

# Flow-Induced Sound and Vibration due to the Separated Shear Layer in Backward-Facing Step and Cavity Configurations

by

Alexey S. Velikorodny

M.Sc., Voronezh State University, 2006

A Dissertation Submitted in Partial Fulfillment of the  
Requirements for the Degree of  
DOCTOR OF PHILOSOPHY  
in the Department of Mechanical Engineering

© Alexey S. Velikorodny, 2009

University of Victoria

All rights reserved. The dissertation may not be reproduced in whole or in part by  
photocopy or other means, without permission of the author.

## **Supervisory Committee**

Flow-Induced Sound and Vibration due to Separated Shear Layer in Backward-Facing  
Step and Cavity Configurations

by

Alexey S. Velikorodny

M.Sc., Voronezh State University, 2006

### **Supervisory Committee**

Dr. Peter Oshkai, (Department of Mechanical Engineering)  
**Supervisor**

Dr. Ned Djilali, (Department of Mechanical Engineering)  
**Departmental Member**

Dr. Brad Buckham, (Department of Mechanical Engineering)  
**Departmental Member**

Dr. Boualem Khouider, (Department of Mathematics and Statistics)  
**Outside Member**

Dr. Graham Duck, (Honeywell Process Solutions, Vancouver)  
**Additional Member**

## ABSTRACT

### **Supervisory Committee**

Dr. Peter Oshkai, (Department of Mechanical Engineering)  
**Supervisor**

Dr. Ned Djilali, (Department of Mechanical Engineering)  
**Departmental Member**

Dr. Brad Buckham, (Department of Mechanical Engineering)  
**Departmental Member**

Dr. Boualem Khouider, (Department of Mathematics and Statistics)  
**Outside Member**

Dr. Graham Duck, (Honeywell Process Solutions, Vancouver)  
**Additional Member**

Fully turbulent inflow past symmetrically located side branches mounted in a duct can give rise to pronounced flow oscillations due to coupling between separated shear layers and standing acoustic waves. Experimental investigation of acoustically-coupled flows was conducted using digital particle image velocimetry (DPIV) in conjunction with unsteady pressure measurements. Global instantaneous, phase- and time-averaged flow images, as well as turbulence statistics, were evaluated to provide insight into the flow physics during flow tone generation. Onset of the locked-on resonant states was characterized in terms of the acoustic pressure amplitude, frequency and the quality factor of the resonant pressure peak. Structure of the acoustic noise source is characterized in terms of patterns of generated acoustic power. In contrast to earlier work, the present study represents the first application of vortex sound theory in conjunction with global quantitative flow imaging and numerical simulation of the 2D acoustic field.

In addition to the basic side branch configuration, the effects of bluff rectangular splitter plates located along the centerline of the main duct was investigated. The first mode of the shear layer oscillation was inhibited by the presence of plates, which resulted in substantial reduction of the amplitude of acoustic

pulsations and the strength of the acoustic source. These results can lead to the development of improved control strategies for coaxial side branch resonators.

Motivation for the second part of this study stems from the paper manufacturing industry, where air clamp devices utilize high-speed jets to position paper sheets with respect to other equipment. Thus, vibration of the paper sheet and turbulent flow that emerged from a planar curved nozzle between a flexible wall and a solid surface containing a backward-facing step (BFS) were investigated using high-speed photography and DPIV, respectively. The emphasis was on the characterization of the flow physics in the air clamp device, as well as of the shape of the paper sheet. For the control case, that involved a solid wall with a geometry that represented the time-averaged paper profile, hydrodynamic oscillation frequencies were characterized using unsteady pressure measurements. Experimentally obtained frequencies of the paper sheet vibration were compared to the hydrodynamic frequencies corresponding to the oscillations of the shear layer downstream of the BFS.



<b>2. EXPERIMENTAL SYSTEM AND TECHNIQUES.....</b>	<b>29</b>
<b>2.1 Side branch resonator.....</b>	<b>29</b>
2.1.1 Overview of the experimental system.....	29
2.1.2 Bluff rectangular splitter plates.....	30
2.1.3 Acoustic pressure measurements.....	31
2.1.4 Quantitative flow imaging of acoustically-coupled flows.....	33
<b>2.2 Air clamp.....</b>	<b>36</b>
2.2.1 Air clamp apparatus in proximity to elastic wall.....	37
2.2.2 Air clamp apparatus in proximity to solid wall.....	40
2.2.3 High-speed photography of the paper sheet.....	42
2.2.4 Quantitative flow imaging in the air clamp apparatus.....	43
<b>2.3 Particle Image Velocimetry and data handling.....</b>	<b>44</b>
2.3.1 PIV fundamentals.....	44
2.3.2 Image processing.....	47
2.3.3 Time-averaging procedures.....	51
2.3.4 Phase-averaging procedures.....	53
<b>3. EXPERIMENTAL RESULTS AND ANALYSIS.....</b>	<b>55</b>
<b>3.1 Acoustically Coupled Flows over Symmetrically Located Side     Branches.....</b>	<b>55</b>
3.1.1 Numerical simulation of acoustic field.....	55
3.1.2 Inflow conditions.....	62
3.1.3 Characterization of the effect of resonator geometry via experimental measurements.....	64
3.1.3.1 Overview of acoustic response.....	64
3.1.3.2 Q-factor of the resonator.....	70
3.1.3.3 Overview of flow patterns.....	74
3.1.3.3.1 Instantaneous flow patterns.....	74
3.1.3.3.2 Phase-averaged flow patterns.....	77
3.1.3.3.3 Time-averaged flow patterns.....	82
3.1.3.4 Acoustic power.....	92

3.1.3.4.1	Acoustic power calculation.....	92
3.1.3.4.2	Acoustic power at one period of acoustic oscillation.....	93
3.1.3.4.3	Time-averaged distribution of the acoustic source.....	94
3.1.3.5	Visco-thermal damping and net acoustic power.....	97
<b>3.2</b>	<b>Turbulent flow over the air clamp in proximity to a flexible and solid     walls.....</b>	<b>101</b>
3.2.1	Paper profile.....	101
3.2.2	Time-averaged flow patterns.....	106
3.2.3	Evolution of vorticity.....	113
3.2.4	Turbulence statistics.....	115
3.2.5	Velocity and turbulence profiles.....	120
3.2.6	Pressure distribution along the upper wall.....	123
3.2.6.1	Distribution of static pressure.....	123
3.2.6.2	Unsteady pressure downstream of the BFS.....	124
<b>4.</b>	<b>CONCLUSIONS AND RECOMMENDATIONS .....</b>	<b>126</b>
<b>4.1</b>	<b>Side branch resonator.....</b>	<b>126</b>
<b>4.2</b>	<b>Air clamp.....</b>	<b>128</b>
	<b>REFERENCES.....</b>	<b>131</b>
	<b>APPENDIX A: SOUND.....</b>	<b>138</b>
	<b>APPENDIX B: VORTEX SOUND THEORY.....</b>	<b>142</b>
	<b>APPENDIX C: DERIVATION OF THE ACOUSTIC POWER     INTEGRAL.. .....</b>	<b>144</b>
	<b>APPENDIX D: AIR CLAMP STAGE AND PAPER SHEET     ASSEMBLY..... .....</b>	<b>146</b>
	<b>APPENDIX E: AIR CLAMP EXPERIMENTAL ISSUES AND     CONSTRAINTS..... .....</b>	<b>147</b>

<b>APPENDIX F: RECOMMEDATIONS FOR AIR CLAMP</b>	
<b>APPLICATION.....</b>	<b>149</b>
<b>APPENDIX G: SOME MATLAB CODES.....</b>	<b>152</b>
<b>PERMISSION LETTERS FOR COPYRIGHTED MATERIAL.....</b>	<b>161</b>

## LIST OF TABLES

<b>2.1</b>	Dimensions of the experimental system .....	30
<b>2.2</b>	Characteristic lengths of side branch resonator with splitter.....	31
<b>3.1</b>	Simulated, theoretical, and measured resonant frequencies for the case of $c/t=2.7$ ( $c/t$ 5.4).....	59
<b>3.2</b>	Simulated, theoretical, and measured resonant frequencies for the case without plate ( $c/t=0$ ).....	59
<b>3.3</b>	Mean values of net acoustic power and visco-thermal losses.....	99
<b>3.4</b>	Summary of inclination angles of the paper sheet and shear layer reattachment lengths for case 2.....	102
<b>3.5</b>	Frequencies of the membrane oscillation modes (Hz).....	105

## LIST OF FIGURES

<b>1.1</b>	Schematic of a mixing layer.....	4
<b>1.2</b>	Schematic of a free plane jet.....	5
<b>1.3</b>	Principal elements of self-sustaining oscillation of turbulent flow past cavity associated with purely hydrodynamic effects (Lin and Rockwell (2001)).....	7
<b>1.4</b>	Schematic of the air clamp flow configuration.....	10
<b>1.5</b>	Schematic of a turbulent plane free jet with induced outer flow.....	12
<b>1.6</b>	Schematic of the side branch resonator.....	18
<b>1.7</b>	Acoustic pressure distribution of resonant acoustic modes in the side branches.....	20
<b>1.8</b>	Schematic of the jet oscillation patterns. $f$ is the oscillation frequency; $f_a$ is the acoustic resonance frequency; $f_{js}$ is the frequency of the natural jet-slot oscillation, and $S$ is the Strouhal number (Ziada 2000).....	23
<b>2.1</b>	Schematic of the side branch resonator experimental system.....	30
<b>2.2</b>	Close-up of the cross-junction.....	31
<b>2.3</b>	Schematic of the side branch resonator experimental system with PIV instrumentation.....	33
<b>2.4</b>	Raw image of the cross-junction region of the side branch resonator.....	35
<b>2.5</b>	Error in paper thickness measurements.....	37
<b>2.6</b>	Schematic of flow configuration in air clamp experimental apparatus.....	37
<b>2.7</b>	Schematic of the air clamp experimental system.....	38
<b>2.8</b>	Side and plan view of the air clamp configuration with solid upper wall..	41
<b>2.9</b>	Characteristic dimensions of a tap for static pressure measurements.....	42
<b>2.10</b>	Raw image of the flow field in the air clamp experimental apparatus. FOV1.....	43
<b>2.11</b>	Flow-chart of DPIV process (Willert and Gharib 1991).....	48

<b>3.1</b>	Computational domain and boundary conditions.....	57
<b>3.2</b>	Close-up of the computational mesh in the cross-junction region.....	58
<b>3.3</b>	Resonant acoustic mode shapes corresponding to acoustic pressure for the case of $c/t=0$ : (a) first mode ( $f = 175$ Hz); (b) third mode ( $f = 526$ Hz); (c) fifth mode ( $f = 879$ Hz).....	60
<b>3.4</b>	Amplitude of the horizontal and the vertical components of acoustic velocity ( $c/t=0$ ) : (a) $(U_{ac})_x$ ; (b) $(U_{ac})_y$ .....	60
<b>3.5</b>	Variation of flow velocity (a) and root-mean-square velocity (b) normalized by wall friction velocity $u_*$ at the exit of the upstream section of the main duct for the cases of the first hydrodynamic mode $(H_1)_L$ and second hydrodynamic mode $(H_2)_L$ ( $c/t=0$ ).....	63
<b>3.6</b>	Pressure amplitude and frequency as functions of incoming velocity ( $c/t=0$ ).....	65
<b>3.7</b>	Pressure amplitude and frequency as functions of incoming velocity ( $c/t=2.7$ ).....	67
<b>3.8</b>	Pressure amplitude and frequency as functions of incoming velocity ( $c/t=5.4$ ).....	69
<b>3.9</b>	Definition of $Q$ -factor.....	70
<b>3.10</b>	Typical pressure spectrum with comb-like structure. Dashed lines correspond to parameters used for calculation of the $Q$ -factor.....	72
<b>3.11</b>	Variation of quality (Q) factor of predominant pressure peak as a function of flow velocity: $c/t=0$ .....	73
<b>3.12</b>	Pattern of instantaneous out-of-plane vorticity corresponding to the first (a), ( $Sr = 0.26$ , $U = 50$ m/s) and second (b), ( $Sr = 0.72$ , $U = 31$ m/s) hydrodynamic modes for the case of $c/t=0$ .....	75
<b>3.13</b>	Pattern of instantaneous out-of-plane vorticity corresponding to the second hydrodynamic mode for the cases of $c/t=2.7$ , $Re_t = 3500$ , $Sr = 0.78$ (a) and $c/t=5.4$ , $Re_t = 3500$ , $Sr = 0.78$ (b) .....	76
<b>3.14</b>	Pattern of phase-averaged vorticity corresponding to the $c/t=0$ , 2.7 and 5.4 cases at $\varphi=36^\circ$ and $144^\circ$ .....	79
<b>3.15</b>	Pattern of phase-averaged vorticity corresponding to the $c/t=0$ , 2.7 and 5.4 cases at $\varphi=250^\circ$ and $324^\circ$ .....	81

<b>3.16</b>	Time-averaged velocity profiles corresponding to the first and second hydrodynamic oscillation modes without splitter plate (a, b) and to the second mode with splitter plates (c, d) .....	82
<b>3.17</b>	Distribution of vorticity thickness across the side branch opening for the case of (a) short and long splitter plate and (b) first and second hydrodynamic oscillation modes without plate.....	84
<b>3.18</b>	Patterns of time-averaged vorticity $\langle \omega_z \rangle$ distribution corresponding to the first and second hydrodynamic oscillation modes without splitter plate (a, b) and to the second mode with splitter plates (c, d) .....	87
<b>3.19</b>	Patterns of time-averaged $\langle u_{rms} \rangle / U_0$ distribution corresponding to the first and second hydrodynamic oscillation modes without splitter plate (a, b) and to the second mode with splitter plates (c, d) .....	88
<b>3.20</b>	Patterns of time-averaged $\langle v_{rms} \rangle / U_0$ distribution corresponding to the first and second hydrodynamic oscillation modes without splitter plate (a, b) and to the second mode with splitter plates (c, d) .....	89
<b>3.21</b>	Patterns of time-averaged $\langle u'v' \rangle / U_0^2$ distribution corresponding to the first and second hydrodynamic oscillation modes without splitter plate (a, b) and to the second mode with splitter plates (c, d) .....	91
<b>3.22</b>	Acoustic power generated by the top (filled) and bottom (open symbols) shear layers during one period of acoustic oscillation: $c/t = 0$ (●), $c/t = 2.7$ (■), $c/t = 5.4$ (▲).....	93
<b>3.23</b>	Patterns of time-averaged distribution of the acoustic source corresponding to the first (a) and second (b) hydrodynamic oscillation modes: $c/t = 0$ .....	95
<b>3.24</b>	Patterns of time-averaged distribution of the acoustic source: $c/t = 2.7$ (a) and $c/t = 5.4$ (b).....	96
<b>3.25</b>	Time-averaged profile of the paper sheet (FOV1, $\Delta p = 25.5$ kPa, $U_0 = 120$ m/s, $W = 88.9$ mm) .....	101
<b>3.26</b>	Spectrum of the paper sheet vibration ( $\Delta p = 25.5$ kPa, $U_0 = 120$ m/s, $W = 158.8$ mm) .....	104
<b>3.27</b>	Time-averaged flow patterns corresponding to FOV1 for Case 1, $U_0 = 95$ m/s.....	108

<b>3.28</b>	Time-averaged flow patterns corresponding to FOV1 for Case 2, $U_0 = 100$ m/s.....	109
<b>3.29</b>	Time-averaged flow patterns corresponding to FOV1 for Case 2, $U_0 = 120$ m/s.....	112
<b>3.30</b>	Time-averaged flow patterns corresponding to FOV1 for Case 3, $U_0 = 100$ m/s.....	113
<b>3.31</b>	Distribution of vorticity thickness in the separated shear layer.....	114
<b>3.32</b>	Time-averaged turbulence statistics corresponding to FOV1 for Case 1, $U_0 = 95$ m/s.....	117
<b>3.33</b>	Time-averaged turbulence statistics corresponding to FOV1 for Case 2, $U_0 = 100$ m/s.....	118
<b>3.34</b>	Time-averaged turbulence statistics corresponding to FOV1 for Case 3, $U_0 = 100$ m/s.....	119
<b>3.35</b>	Distributions of time-averaged horizontal velocity as a function of vertical coordinate corresponding to FOV3 for Case 1, $U_0 = 95$ m/s.....	120
<b>3.36</b>	Distributions of time-averaged horizontal velocity as a function of vertical coordinate corresponding to FOV3 for Case 2, (a): $U_0 = 100$ m/s, (b): $U_0 = 120$ m/s.....	121
<b>3.37</b>	Distributions of time-averaged horizontal velocity as a function of vertical coordinate corresponding to FOV3 for Case 3, $U_0 = 100$ m/s.....	121
<b>3.38</b>	Time-averaged turbulence statistics corresponding to FOV3 for Case 2, $U_0 = 100$ m/s.....	122
<b>3.39</b>	Distribution of static pressure corresponding to FOV3 for Case 3, $U_0 = 100$ m/s.....	123
<b>3.40</b>	Spectrum of the unsteady pressure downstream of the BFS ( $x/h = 6$ ). Case 3, $U_0 = 100$ m/s.....	125
<b>A.1</b>	Time-averaged paper sheet profiles from Honeywell and high-speed photography (present)experiments.....	149
<b>A.2</b>	Schematic of the air clamp with suction ports.....	150

## ACKNOWLEDGEMENTS

I would like to thank to my supervisor Dr. Peter Oshkai for introducing me to the experimental fluid mechanics and PIV flow measurements in particular, as well as for his emotional, technical and financial support throughout the course of this work. I'm also indebted to Dr. Ned Djilali, who shared his experience in a number of discussions on various topics, including my projects, turbulence and validation. I wish to acknowledge Dr. Graham Duck from Honeywell Process Solution for providing our group with significant financial support and experimental materials, as well as for a great opportunity to study a complex industry relevant problem. I would like also to thank Dr's Boualem Khouider and Brad Buckham for providing me with important notes relevant to my analytical and numerical work.

I have had pleasure to know and work with the following Postdoctoral Fellows. First, I had an infinite number of interesting discussions on CFD and other topics with Dr's Latif Bouhadji and Boris Chernyavsky. Second, I owe a debt of gratitude to Dr. TC Wu who helped me at the initial stages of my work in the Experimental Fluids Lab. Finally, I was always encouraged by the sense of humour and optimism of Dr. Slava Berejnov who knows practically everything.

I wish to acknowledge the staff of the Mechanical Engineering Department. In particular, I would like to thank senior scientific assistant Rodney Katz for a number of manufacturing ideas and excellent skills. I wish to thank Peggy White and Sue Walton from the IESVic office for their great administrative support and, of course, Dorothy Burrows for all her help and cheerfulness.

Finally, I would like to express my sincere gratitude to my family in Russia. Thank you for *never* pushing me hard towards research that is why I always did want to learn more. Above all, I would like to thank my wife Anna for always being near me. Without your endless support I wouldn't be able to complete this work.

*To my family*

# CHAPTER 1

## INTRODUCTION

### 1.1 STRUCTURE OF THE DISSERTATION

The dissertation is structured to consist of four chapters. The first introductory chapter presents the motivation for this work and a literature survey of the past and present research in the area of flow-induced sound and vibration due to separated-reattaching flows in various geometries. Section 1.3.2 contains detailed description of the hydrodynamic features encountered in these geometries. Sections 1.3.3 and 1.3.4 provide a review of the experimental and theoretical progress related to flow-acoustic coupling phenomena. All mathematical background and derivations necessary in these sections are provided in Appendices A through C. One of the major scientific values of this dissertation (they are listed in Section 1.4) is the ability to use reported results and observations in application to passive or active control of the separated-reattaching shear layers. Therefore, possible control strategies are included in Section 1.3.5

Experimental systems and techniques used to obtain appropriate experimental results are considered in Chapter 2. Chapter 3 presents experimental results and analysis for both acoustically-coupled flows over deep cavities and air clamp projects. Conclusions and possible directions for future research are outlined in Chapter 4. Due to the industrial nature of the air clamp project necessary experimental issues and

constraints are added in Appendix E, as well as possible methods to control flow separation from the paper sheet are described in Appendix F.

## **1.2 MOTIVATION AND BACKGROUND**

Flow-induced noise and vibrations can arise in a variety of industrial applications and various aspects of this phenomenon received considerable attention from the research community to date. A flow past a mouth of a deep cavity (side-branch) can result in an excitation of high –amplitude acoustic pulsations. Such pulsations are often encountered in gas-transport systems, heat exchangers, electrical and nuclear power stations, and other industrial processes involving transport of a fluid through a pipeline. Relevant practical situations have been reported by several authors including Chen and Sturchler (1977) and Baldwin and Simmons (1986). Flow pulsations may reduce accuracy of flow measurements, alter performance of relief valves and cause undesirable vibration of piping elements. The latter may result in structural damage and industrial accidents. Therefore, high-amplitude pressure pulsations and flow oscillations must be characterized in order to optimize geometry for noise control.

Motivation for the second study reported in the dissertation stems from the paper manufacturing industry, where at various stages of the manufacturing process, sheets of moving paper need to be precisely positioned with respect to sensors and other equipment. The air clamp device utilizes a high-speed jet of air to apply force to the paper sheet without mechanical contact (Moeller et al. (2005)). Interactions, between unsteady separated air flow downstream a backward-facing step and the flexible paper sheet, that occur during operation of the air clamp result in a complex

shape of the paper sheet. Consequently, accuracy of the measurements of the properties of the paper is reduced. The present experimental study aims to characterize the flow-structure interactions (FSI) by providing detailed quantitative visualization of the flow patterns and the shape of the paper sheet. In addition, flow-induced vibrations of the paper sheet are characterized in terms of frequencies and amplitudes of the dominant oscillation modes.

It should be noted that the common feature of these two areas of investigation is the presence of an unstable separated and reattaching shear flow. In the first case, this hydrodynamic instability excites the resonator and leads to a pronounced acoustic response. In the air clamp, the shear layer instability leads to an undesirable vibration of the elastic boundary (paper sheet). The amplitude of these oscillations is, however, limited due to absence of resonance between flow structures and modes of the paper sheet vibration. Nevertheless, such coupling would exist if the paper was clamped only at one edge corresponding to the cantilever beam configuration. Large amplitude oscillations can be achieved in this scenario, leading to the rupture of the paper sheet in some instances. Although, this work doesn't attempt to describe similarities between flow-induced acoustic pulsation and flow-induced structural vibrations at resonance conditions, the experiments that were performed can serve as a basis for such an endeavour in future studies.

## **1.3 LITERATURE SURVEY**

### ***1.3.1 Free shear flows***

This Section provides basic background on the free shear flows, which are relevant to the separated shear layers described in this work. The mixing layer is a

type of a free shear flow. It is defined for an idealized case of two parallel laminar flows with different velocities ( $U_1; U_2 = \lambda U_1; \{0 \leq \lambda < 1\}$ ). The schematic of Fig. 1.1 shows two initially unperturbed flows of different velocities frictionally interacting with each other. This interaction takes place in the thin mixing zone, in which the transverse component of velocity is small compared to the longitudinal one, therefore the classical boundary layer equations for a flat plate at zero incidence can be used to describe this flow.

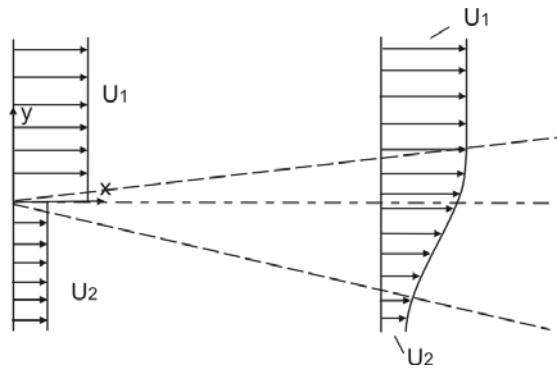


**Fig 1.1** Schematic of a mixing layer

From the numerical solution of the boundary layer equations with appropriate boundary conditions it follows that the transverse velocity at the edge of the upper layer is less or equal to zero ( $v_{+\infty} \leq 0$ ), while at the edge of the bottom one it is larger than zero ( $v_{-\infty} > 0$ ). This implies that the mixing layer sucks the fluid from both the upper and the lower side. Because of a global balance of momentum ( $v_{+\infty} = -\lambda v_{-\infty}$ ) this suction is always greater from the small longitudinal velocity region (bottom side in Fig. 1.1). The process of *entrainment* described above is typical to free shear flows, such like free jets, wakes, and their boundaries (Schlichting and Gersten (2000)).

In any practical flow scenario the mixing layer is a turbulent flow. It forms, for example, at the edge of a plane jet ( $U_1 = U_j$ ) flowing into stagnant surroundings

( $U_2 = 0$ ). The fluid from this region is entrained into the core of the jet, leading to the velocity profile shown in Fig. 1.2.

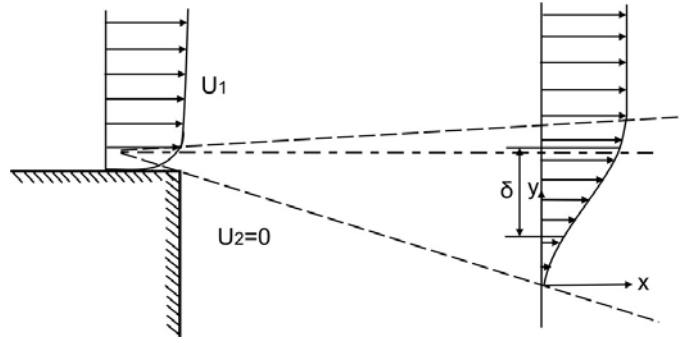


**Fig 1.2** Schematic of a free plane jet

There are many experimental studies that confirm that the mixing layer for this case is self-similar (Wynanski and Fiedler (1970), Champagne et al. (1976)). This means that after the developing region, the mean velocity profile  $\overline{U(x, y)}$  scaled with  $U_1$  does not depend on the distance from the origin ( $x$ ), but only on a cross stream coordinate, which is non-dimensionalized by  $\delta(x)$  – the characteristic width of the jet. As a consequence, spreading of the mixing layers is essentially linear, which was also shown experimentally by Champagne et al. (1976). Similarly, a plane jet with the upper wall, as well as other free shear flow scenarios can be considered (e.g. Pope (2000)). All of these flow scenarios exhibit constant growth rate behaviour in time-averaged sense.

The growth rate of the shear layer can be deduced from the vorticity thickness, which is defined as follows:

$$\delta_\omega = \frac{U_1 - U_2}{\left(\frac{\partial \langle u \rangle}{\partial y}\right)_{\max}}, \quad (1.1)$$

where  $U_1$  and  $U_2$  are free-stream velocities on the upper and lower sides of the shear layer. Moreover, transformation from the small-scale vortices to large-scale clusters of vorticity can be quantified in terms of variation of the vorticity thickness as a function of the downstream distance, since the wavelength and the scale of the vortices in the shear layer are expected to increase as the vorticity thickness increases (Monkewitz and Huerre (1982)). The growth rates for plane mixing layers based on vorticity thickness reported by Brown and Roshko (1974) are in the range from 0.145 to 0.22.

### ***1.3.2 Hydrodynamic features of shear flows with separation and reattachment***

#### ***1.3.2.1 Non-resonant cavity flows***

The basic classification of cavity flows has been the focus of a number of investigations. First, a cavity can be considered as either a deep or shallow cavity. The cavity is defined to be deep, according to Sarohia (1977), if its length-to-depth ratio is less than unity ( $L/D < 1$ ), while the opposite is true for the shallow one (i.e.,  $L/D > 1$ ). Although shallow cavities can be differentiated further to be of open or closed type, only deep cavities will be considered in this thesis. Second, Rockwell and Naudascher (1979) classified the flow excitation mechanisms in cavities into fluid-resonant and fluid-dynamic categories. The fluid-dynamic (acoustic-free) mechanism corresponds to generation of self-sustained flow oscillations in the absence of resonance effects. In contrast, in the fluid-resonant regime, the oscillations are sustained by the coupling between the resonant sound field and the separated unstable flow. In that case, deep cavity flows in particular ( $L/D \sim 0.05$ ), were experimentally investigated by Elder et

al. (1982) when upstream boundary layer was laminar or turbulent. The most noticeable effect due to turbulence was the general increase in background noise at all speeds. The hydrodynamic oscillations in an acoustic-free system are illustrated in Fig. 1.3.

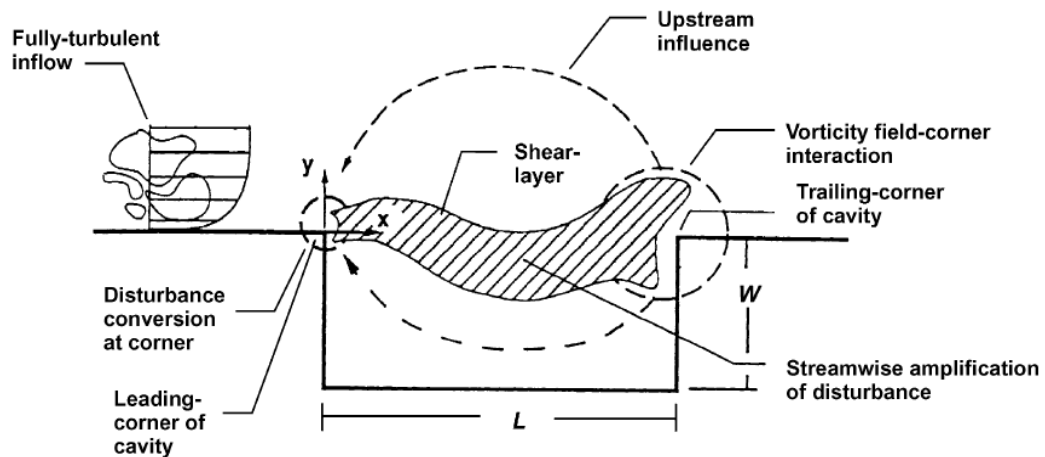


**Fig 1.3** Principal elements of self-sustaining oscillation of turbulent flow past cavity associated with purely hydrodynamic effects (Oshkai 2002)

From the standpoint described in Section 1.3.1, passage of fluid beyond the upstream edge and across the opening resembles the development of a classical free shear layer. This layer is unstable and will roll up to form a train of vortices.

The chain of events that leads to the establishment of the self-sustained oscillations can also be described as follows (Blake (1986)). First, a disturbance is initiated in the shear layer. The magnitude of this disturbance increases as the corresponding vorticity is convected downstream. This behaviour is described by Eqn. (1.2). Subsequently, a disturbance is generated at a downstream location. A typical example of such secondary disturbance is the pressure fluctuation due to interaction of the vortices in the shear layer with the downstream edge of the cavity. Finally, the downstream-initiated disturbance propagates upstream by either acoustic, elastic, or

hydrodynamic means to perturb the inflow and to amplify the initial upstream disturbance.

Based on the linear stability analysis, the transverse velocity associated with the shear layer undulation can be interpreted as a linear approximation of the initial disturbances that are present in the shear layer. The amplification of the transverse oscillations of the shear layer can be expressed according to Eqn. (1.2) (Blake (1986)).

$$u(x, y, t) = |u(y)| e^{\alpha_r x} e^{i(\alpha_i x - \omega t)}, \quad 0 \leq x \leq L \quad (1.2)$$

where  $u(x, y, t)$  is the fluctuating transverse velocity,  $\omega$  is the angular frequency,  $\alpha_r$  is the real part of the complex wave number  $\alpha = \alpha_r + i\alpha_i$ ,  $L$  is the width of the cavity. The parameter  $\alpha_r x$  represents the growth of the disturbance along the opening. The disturbance at the downstream edge of the cavity can be written as

$$u(L, y, t) = |u(y)| e^{\alpha_r L} e^{i(\alpha_i L - \omega t)}. \quad (1.3)$$

The optimal coupling between the initial disturbance at the shear layer separation and the disturbance at the downstream edge occurs when the fluctuating velocity at the downstream edge is  $\pi/2$  radians out-of-phase with respect to the fluctuations at the upstream corner (flow separation point). This condition is expressed in Eqn (1.4).

$$\alpha_r L = 2n_s \pi - \pi/2, \quad n_s = 1, 2, 3, \dots \quad (1.4)$$

where  $n_s$  is the shear layer (hydrodynamic) oscillation mode number.

Since  $\alpha_r = \omega/U_c$ , where  $U_c$  is the convective speed of the corresponding vorticity, the preferred frequencies,  $f_s = \omega/2\pi$ , are given by

$$f_s L / U_c = (n_s - \frac{1}{4}), \quad n_s = 1, 2, 3, \dots \quad (1.5)$$

This equation describes the possible frequencies of fluid disturbance under a standing wave condition across the cavity opening. The phase and strength of the feedback disturbance will depend on the geometry of the cavity and fluid mechanics of the shear layer. A more general expression for the self-sustained oscillation condition is

$$f_s L / U = \frac{U_c}{U} (n_s - \frac{1}{4} - \varphi / 2\pi), \quad n_s = 1, 2, 3, \dots \quad (1.5')$$

where  $U$  is the free-stream velocity, and  $\varphi$  is a phase angle that accounts for the possibility of a phase lag between the generation of disturbance at the downstream edge of the cavity and the response of the separating shear layer. This equation can be further extended by introducing the local Mach number in the case of compressible flows (Rossiter (1964)).

The majority of the previous studies considered shear layer to be quasi-two-dimensional, while three-dimensionality of the flow may play a dominant role in certain cases (Maull and East (1963), Faure et al. (2007), Ahuja and Mendoza (1995), Rockwell and Knisely (1980), Bres and Colonius (2007)). Ahuja and Mendoza (1995) conducted a thorough investigation of the effect of cavity dimensions, boundary layer parameters, and temperature on cavity noise. They provided a threshold for transition from 2D to 3D flow. When the cavity length-to-width ratio is less than unity, the cavity is termed two-dimensional, meaning that the flow is uniform over much of the span. If this ratio exceeds unity, 3D effects are significant. Rockwell and Knisely (1980) used a hydrogen bubble technique to visualize three-dimensional flow patterns in a water channel experiment for a wide rectangular cavity with laminar boundary

layer upstream. Recent experimental investigation by Faure et al. (2007) that involved smoke-based flow visualization has demonstrated occurrence of 3D structures in separated cavity flows. Direct numerical simulations (DNS) of open cavity compressible low Reynolds number flows have been recently performed by Bres and Colonius (2007), revealing 3D structures for a range of cavity configurations.

### 1.3.2.2 Backward-facing step flows

The essential feature of the air clamp shown in Fig. 1.4, which is a subject of the present study, is a backward-facing step (BFS), which was located downstream of the *Coanda* nozzle. The downward inertia of the jet induced by the *Coanda* effect (see details in Section 1.3.2.3) is manifested in a reduced spatial extent of the flow recirculation zone, downstream of the BFS. Similar to cavity flows, as the wall-bounded jet flow leaves the sharp edge of the BFS, it separates and forms a thin shear layer, which is unstable and rolls up into a train of vortices. The shear layer subsequently reattaches to the bottom wall. As a result, a recirculation zone is formed immediately downstream of the BFS.

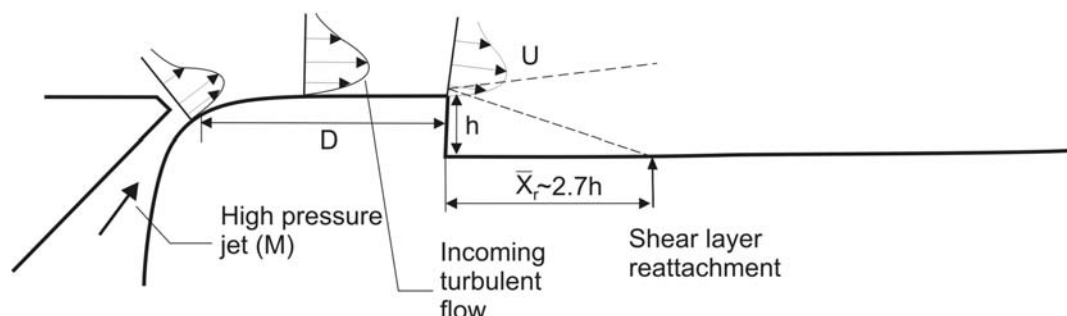


**Fig. 1.4** Schematic of the air clamp flow configuration

Features of flows over BFS have been extensively studied over the years. The majority of the previous investigations employed experimental and theoretical

approaches (Eaton and Johnston (1980), Armaly et al. (1983), Hasan (1992)). In addition, Le et al. (1997) and Dandois et al. (2007) performed direct numerical simulations of BFS flows.

For classical BFS flows (without Coanda effect – see section 1.3.2.3), the reattachment length ( $\overline{X}_r$ ) varies in the range of  $6h$  to  $9h$ , where  $h$  is the height of the BFS (Dandois et al. (2007)). As the Reynolds number based on  $h$  and the free stream velocity  $U$  is increased, the reattachment length  $\overline{X}_r$  is decreased for the range of the Reynolds numbers  $1200 < Re < 6600$ , and remains constant for the fully turbulent flow regime with  $Re > 6600$  Armaly et al. (1983).

The separated shear layer that forms downstream of the BFS is characterized by two types of hydrodynamic instabilities: the convective instability and the absolute instability. The convective (Kelvin-Helmholtz type) instability is related to periodic formation of vortices in the shear layer. The frequency of the convective instability  $f_c$  is related to the momentum thickness of the shear layer Hasan (1992), which in turn serves as a characteristic length scale for determining the growth rate of the shear layer. Another important characteristic length of the BFS flows is the reattachment length  $\overline{X}_r$ . The corresponding Strouhal number ( $Sr_c = f_c \overline{X}_r / U$ , where  $f_c$  is the characteristic frequency of the instability) varies from 0.6 to 0.8 (Dandois et al. (2007)). In addition, Sigurdson (1995) proposed a different scaling based on the separation bubble height and the velocity at the separation point, which correlates the shedding frequencies of a wide variety of separated flows. The absolute instability is related to flapping of the shear layer, which is caused by the imbalance between the viscous entrainment of the fluid into the mixing layer and periodic injection of the

fluid from the recirculation region as described by Eaton and Johnston (1980). The Strouhal number corresponding to the absolute instability ( $Str_a = f_a \overline{X_r} / U$ ) is approximately one order of magnitude lower than that of the convective instability ( $0.08 < Str_a < 0.18$ ) (Dandois et al. (2007)).

### 1.3.2.3 Wall effects and curved boundary flows (*Coanda effect*)

The purpose of this section is to provide an overview on the curved wall bounded flows, and associated *Coanda* effect, which is one of the main principles of the air clamp operation. It was indicated in Section 1.3.1 that while the transverse velocity ( $v$ ) in free shear flows is rather small, it does not vanish at the edge of the jet, but is directed towards the core of the jet, thus causing entrainment of the surrounding fluid. The considered scenario can become more complex when there are walls in the outer region or at the jet outlet as it is shown in Fig.1.5 (Schlichting and Gersten (2000)).

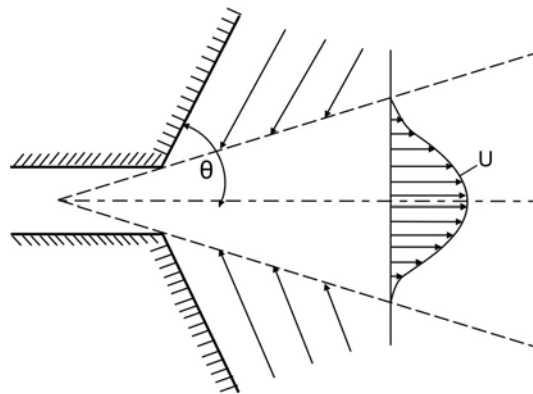


**Fig 1.5** Schematic of a turbulent plane free jet with induced outer flow

If, for example, the angle  $\theta$  of the upper wall is greater than the angle of the lower wall (or there is no upper wall), the jet can be deflected towards the lower wall, leading to the curvature of the free jet. In general, the physical mechanism of the jet

reattachment to the wall is as follows: the surrounding fluid (air) is entrained into the core of the jet both from the wall side and from the ambient fluid side. In the confined region between the jet and the wall, the amount of fluid available for entrainment is limited, and the pressure is reduced compared to the opposite side of the jet. This pressure drop induces the jet deflection towards the wall and its reattachment if the wall is sufficiently long.

This phenomenon is termed a *Coanda* effect by the name of a Romanian engineer, Henri Coanda (Coanda (1932)), and has been studied by several researchers in the configuration similar to Fig. 1.5. Newman (1961) studied experimentally the variation of the reattachment length against the inclination angles  $\theta$  at a constant velocity. He showed that this length increases with  $\theta$ . At constant velocity and wall length, Newman (1961) found that the jet is always attached to the wall at small angles ( $\theta < 50^\circ$ ) and never attached at large angles ( $\theta \geq 64^\circ$ ). For intermediate  $\theta$  values, flow is either detached from the wall or reattached to it, depending if the angle is increased or decreased, showing the hysteresis cycle. Recently, Allery et al. (2004) have been carried out experiments and LES study when the Reynolds number varies. The hysteresis cycle has been confirmed by this study. Interestingly, authors have found out that there is one and only one couple of the parameters ( $\theta, Re$ ) both for the attachment and detachment of the flow.

Similar flow physics govern the case when the sharp corner in Fig. 1.5 is replaced by a curved wall ( $\theta \rightarrow R_c$ ). Recently, Coanda jet flow over the surface of a circular cylinder was investigated experimentally by Wygnanski and co-authors (Neuendorf and Wygnanski (1999), Neuendorf et al. (2004), Han et al. (2006)). Particle image velocimetry (PIV) measurements reported by in these works revealed

the existence of large-scale streamwise flow structures. These vortices appear to be responsible for the overall increase in the turbulent momentum exchange compared to a plane wall jet. It should be noted that the presence of the curved surface adds to the complexity the flow structures, creating an instability mechanism, associated with centrifugal forces. It is commonly referred to as the Görtler instability (e.g. Saric (1994)). It is interesting to note, that similar flow structures were reported to be present in a range of cavity configurations by several recent experimental and numerical investigations (Faure et al. (2007), Bres and Colonius (2007)).

#### *1.3.2.4 Diverging channel flows*

As it is shown in Section 3.2.1, during the operation of the air clamp, interaction between the separated flow downstream of the BFS and the flexible upper wall (paper sheet) resulted in deformation of the paper sheet establishing a diverging channel geometry between the paper sheet and the surface of the air clamp. This geometry shares common characteristics with an asymmetric diffuser, which is a diverging flow area between two surfaces positioned at an angle with respect to each other.

Flows through planar and conical diffusers have been subjects of detailed experimental and numerical investigations (Azad (1996), Okwuobi and Azad (1973; Wu et al. (2006)). Both of these geometries are characterized by a mildly favorable pressure gradient that exists upstream of the diverging area and which becomes strongly adverse at the throat of the diffuser. The magnitude of the adverse pressure gradient is decreasing with the downstream distance until the flow separation/recovery region.

The adverse pressure gradient in an asymmetric diffuser eventually leads to flow separation due to loss of momentum in the boundary layer that exists along the inclined wall. The location of the separation point is dependent on the inflow velocity, in contrast to the BFS flows, where separation always occurs at the fixed point (edge of the BFS). Similar to the BFS flows, separated shear layer in a diffuser eventually reattaches to the wall (Buice and Eaton (1997)). Gullman-Strand et al. (2004) studied the influence of the angle of the asymmetric diffuser on the extent of the recirculating flow region using experimental and numerical approaches.

Specifically related to the present study are the experimental investigations of Driver and Seegmiller (1985). The authors reported experimental measurements of turbulent flow over a BFS in a diverging channel. In contrast to that study, the present configuration involves a highly-confined inflow upstream of the BFS, which is also influenced by the Coanda effect.

#### *1.3.2.5 Bluff rectangular splitter plate flows*

Another type of separating-reattaching flows considered in this dissertation with application to control of acoustic resonances is a flow around a bluff rectangular splitter plate (e.g. Fig 2.2) This configuration was subject of a number of experimental studies at high Reynolds numbers ( $>20 \cdot 10^3$ ) (Cherry et al. (1983), Kiya and Sasaki (1983), Djilali and Gartshore (1991), Saathoff and Melbourne (1997)). In these works, the authors accessed the mean and fluctuating characteristics as well as large-scale unsteadiness of turbulent flow around bluff rectangular plates. These studies report a characteristic low frequency flapping of the separated shear layer that forms at the leading edge of the plate, which is similar to the absolute instability found in the BFS

flows (Section 1.3.2.2). The strong dependence of this type of flow on turbulence is also well documented. Hillier and Cherry (1981) report shortening of the recirculation zone from  $4.88 \cdot t$  to  $2.72 \cdot t$  ( $t$  – is the thickness of the plate) when the free stream turbulence intensity was only increased from 1% to 6.5%. A reduction of over 50% in the mean reattachment length ( $\overline{X_r}$ ) and significant changes in the dynamics of the flow have been demonstrated when turbulence levels reached up to 12% (Saathoff and Melbourne (1997)). These findings are of particular interest to the dissertation since main results shown in the foregoing sections were obtained with the fully-turbulent inflow at moderate Reynolds numbers.

Direct numerical simulation of the flow over a bluff plate at  $Re=1000$  were performed by Tafti and Vanka (1991). Although transitional regime was considered, the study reproduced many of the large-scale characteristics observed at higher Reynolds numbers with  $\overline{X_r}=6.5 \cdot t$ . In particular, time-dependent features such vortex shedding and vortex convection velocities are predicted to be in agreement with the aforementioned experiments at high Reynolds numbers. Large-eddy simulation for flows around bluff plate reported by Suksangpanomrung et al. (2000) were performed at  $Re=50 \cdot 10^3$ . The blockage ratio ( $D/t$ ) both for experimental and numerical works cited herein was less than 6%, where  $D$  is the height of the duct.

Separation-reattachment processes are also strongly related to the geometry of the bluff rectangular plate. In particular, an important parameter for the dynamics of the flow structures and vortex street formation is the chord-to-thickness ratio ( $c/t$ ). For  $Re=8 \cdot 10^3 - 44 \cdot 10^3$  and with the low turbulence inflow Parker and Welsh (1983) were able to identify four following regimes, which were dependant on the  $c/t$ :

- 1) On short plates ( $c/t < 3.2$ ), flow separation occurs at the leading edge corners and the shear layers interact directly, without reattaching to the plate's surface.
- 2) On longer plates ( $3.2 \leq c/t \leq 7.6$ ), the shear layers reattach to the trailing edge periodically in time. The separation bubble growth enveloping the trailing edge and permitting fluid from the recirculation zone to pass into the vortex formation region, initiating a new vortex at separation.
- 3) For still longer plates ( $7.6 < c/t \leq 16$ ), the shear layers always reattach upstream of the trailing edge and form a separation bubble which grows and divides in a random manner. This process generates a boundary with discrete concentrations of vorticity, which move along the plate surface towards the trailing edge. No clear vortex street was observed in this case.
- 4) For plates with  $c/t > 16$ , the boundary layers approach fully turbulent state well downstream of the leading edge separation. Thus, trailing edge separation is not related to the formation of the recirculation zone in the vicinity of the leading edge.

### **1.3.3 Acoustically-coupled flows**

High-amplitude flow oscillations, which are characteristics of the flow-acoustic coupling in the side branch systems shown in Fig. 1.6, have been a subject of many investigations, as summarized by Ziada and Buhlmann (1992).

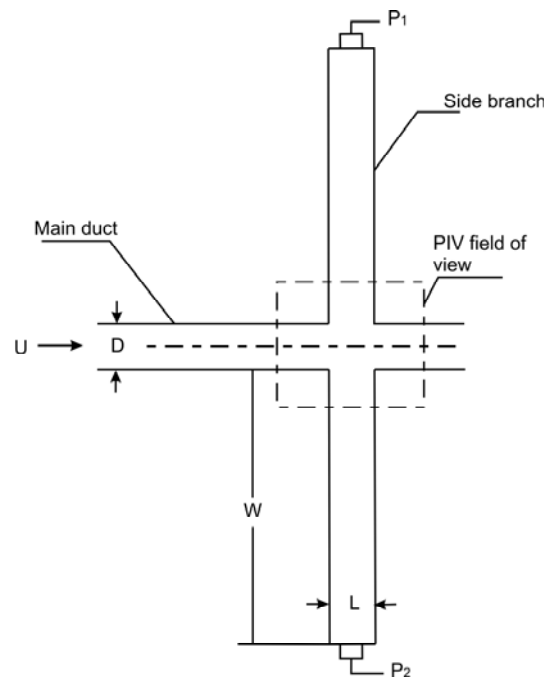


**Fig. 1.6** Schematic of the side branch resonator

Flow-acoustic resonance occurs when the frequency of the self-sustained shear layer oscillations (Section 1.3.2.1) matches the resonant acoustic mode of the side branch. Interaction between the vorticity-bearing velocity field and the acoustic field, which is defined as the unsteady irrotational component of the velocity field  $\underline{V}$ , results in formation of large-scale vortical structures that are convected across the mouth of the cavity. The energy transfer is described by the vortex sound theory that was developed by Powel (1964) and generalized by Howe (1975) (see Appendix B for more details). Under the assumption of negligible frictional losses, the interaction is described by Crocco's form of Euler's equation

$$\frac{\partial \underline{V}}{\partial t} + \nabla B = -\underline{\omega} \times \underline{V}, \quad (1.7)$$

where  $B = \int \frac{dp}{\rho} + v^2 / 2$  is the total enthalpy (with  $v$  being a potential velocity), and  $\underline{\omega}$  is the vorticity. If the Mach number is small, convective effects on the propagation of

acoustic waves can be neglected, and equation (1.7) upon application of divergence operator becomes:

$$\frac{1}{c^2} \frac{\partial^2 B}{\partial t^2} - \Delta B = \underline{\nabla} \cdot (\underline{\omega} \times \underline{V}), \quad (1.8)$$

where  $c$  is the speed of sound. Thus, the source of sound corresponds to the Coriolis force density  $f_c = -\rho_0 (\underline{\omega} \times \underline{V})$ , where  $\rho_0$  is the fluid density.

It has been demonstrated (e.g. by Ziada and Buehlmann 1992) that for long side branches ( $W/D \gg 1$ ), the resonant frequencies of a coaxial side branch resonator can be predicted using the following theoretical expression:

$$f = \frac{(2n-1)c_0}{2(2W+D)}, \quad n=1,2,3,\dots, \quad (1.9)$$

where  $m = 2n - 1$  ( $n = 1, 2, 3, \dots$ ) indicates the mode number,  $c_0 = 343$  m/s is the speed of sound and  $D$  is the width of the main duct.

In the present investigation, a simple quarter wave resonator model was used to describe the response of each branch of the coaxial resonator. According to this model, only acoustic waves that are odd multiples of a quarter wavelengths can be excited inside the side branches. The pressure perturbations in the coaxial side branches at several resonant acoustic modes are illustrated schematically in Fig. 1.7.

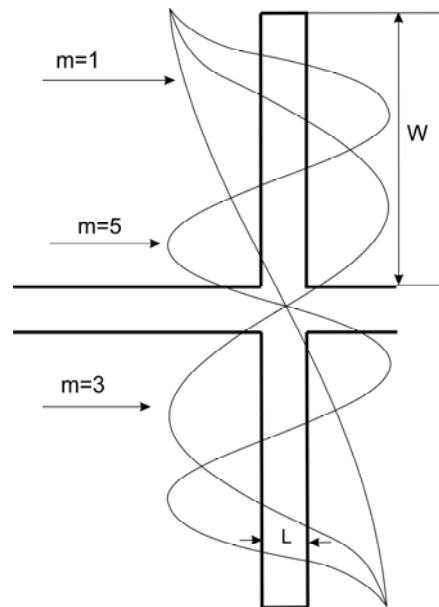


**Fig. 1.7** Acoustic pressure distribution of resonant acoustic modes in the side branches

Fig. 1.7 shows three examples of possible resonance modes, corresponding to  $m = 1, 3,$  and  $5$ . For  $m = 1$ , one quarter of the characteristic wavelength of the resonator spans the depth of each side branch, and thus one half of a wavelength is completed across both side branches. Similarly, for  $m = 3$  and  $m = 5$ , three quarters of a wavelength and five quarters of a wavelength span each side branch respectively.

Measurements of the frequencies of cavity tones have been performed for a variety of external boundary layer flows by DeMetz and Farabee (1977) and Elder et al. (1982). For small values of  $\delta/L$ , where  $\delta$  is the boundary layer thickness, the reported Strouhal numbers suggest relatively high values of average vorticity convection velocity. More specifically,  $U_c/U$  usually varies from 0.33 to 0.45, but may go up to 0.9 if the jet-mode is considered (Blake 1986). The frequencies of the shear layer oscillations will be approximated according to Eqn. (1.5).

The more complex mechanisms of resonant interaction between the acoustic field and the oscillating shear layer in deep cavities and symmetrically located side-

branches has been a subject of several experimental investigations (e.g. Nelson et al. (1981), Jungowski et al. (1989), Bruggeman et al (1989), Ziada and Buehlmann (1992), Ziada (1994), Kriesels et al. (1995), Oshkai et al. (2008), Velikorodny et al. (2009)). At the point of separation, the incident acoustic waves amplify the shear layer fluctuations. The small-scale vortices extract energy from the mean flow to form large-scale vortex structures. Further downstream, the energy is transferred into the resonant acoustic field through the interaction of the formed vortices with the downstream corner of the cavity. This mechanism is described in detail by Ziada (1994).

Kriesels et al. (1995) employed laser-Doppler velocimetry to obtain measurements of flow in cross-junction of coaxial side branch system. It was shown that the acoustic velocity amplitude at the resonance conditions is comparable to the flow velocity at the center line of the main duct. Experiments of Ziada (1994) provide detailed smoke visualizations of formation and propagation of vortices during a single period of acoustic oscillation cycle. The objective of the study was to try to understand non-linear mechanisms of the shear layer response to the large-amplitude acoustic pulsations, as well as the adjustment of the feedback of the system in such manner that a favourable phasing of events occurs over a wide range of lock-in (range of velocities). “Better understanding of these aspects is a prerequisite for the development of nonlinear models which are capable of predicting not only the onset of oscillations but also its amplitude as a function of flow velocity”, Ziada (1994).

Simple linear models of the acoustically-coupled flows have recently been considered by Dequand et al. (2003). These models are based on Nelson’s representation of the shear layer as a row of discrete vortices convected at constant

velocity towards downstream edge of the cavity (Nelson et al. (1983)). Once concentrated vorticity values are known vortex sound theory suggested by Powell (1964) and extended by Howe (1975) is employed (e.g. Appendix B). Numerical simulations, based on the Euler equations for two-dimensional inviscid and compressible flows were also performed in these studies. All simulations overpredicted experimentally obtained acoustic pulsation amplitudes by 30-40%.

Jungowski et al. (1989) reported that the ratio between the cavity width and the main duct width has a pronounced effect on the acoustic pressure amplitude. When this ratio was increased a substantial reduction in the pulsation amplitude was observed. The mechanism which is responsible for such behavior of the coaxial side branch resonator was recently investigated by Oshkai et al. (2008). The accompanied quantitative description of the hydrodynamic field and visco-thermal losses calculated on that basis can be found in Velikorodny et al. (2009a).

While preceding discussion is related to flows over deep cavities, other types of resonators can be described using a conceptually similar approach. Specifically related to coaxial side branch resonators is a jet-slot oscillator model (Blake 1986), which is also based on Eqn. (1.9). Ziada (2000) emphasized that the hydrodynamic behaviour of the jet-slot oscillator changes substantially when the resonance is excited. It was observed that the shear layer oscillation was symmetrical when the resonance was not established (Fig 1.8, Case B), which is in contrast to an anti-symmetric oscillation during resonance (Fig 1.8, Cases A, C).

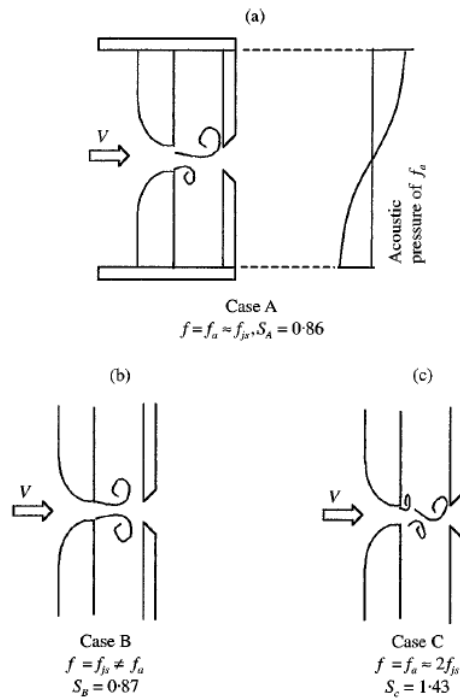


**Fig.1.8** Schematic of the jet oscillation patterns.  $f$  is the oscillation frequency;  $f_a$  is the acoustic resonance frequency;  $f_{js}$  is the frequency of the natural jet-slot oscillation, and  $S$  is the Strouhal number (Ziada 2000).

At the onset of resonance, the pressure amplitude increases sharply, while the flow velocity and the pressure oscillations in the cavities (side branches) become out-of-phase with each other. Therefore, the jet oscillation pattern switches to an antisymmetric mode when the resonance is excited, as illustrated schematically in Fig. 1.8 (Cases A and C).

It should be noted that the splitter plates are extensively used in industry to alleviate strong flow-acoustic resonances. Howe (1986) theoretically studied the effect of the perforated screens on dissipation of sound in large industrial heat exchangers. Recently, Arthurs et al. (2006) investigated the effect of a splitter plate that spans across the entire side branch in order to limit propagation of the acoustic waves. In contrast to the experiments of Arthurs et al. (2006), the plates in the present

study did not span across the entire side branch, which limited their interference with the acoustic wave propagation.

### **1.3.4 Vortex sound theory**

It has been clearly established by the works of Howe (1975) and Howe (1984), Nelson et al. (1983), Stokes and Welsh (1986) and Bruggemann (1989) among others, that Powel's vortex sound theory as generalized by Howe (1975) provides a reasonable procedure for calculating the interaction between the acoustic and the vortical fields (Appendix B). In the framework of this theory an influential for engineering community corollary was provided by Howe (1984).

Howe (1984) summarized, that with the low Mach number, inviscid, constant entropy approximation, the total flow velocity can be represented by a linear combination of an incompressible vorticity-bearing velocity and an irrotational acoustic velocity. The acoustic velocity is defined as the unsteady component of the irrotational part of the total flow velocity. As a consequence, instantaneous acoustic power  $P$  generated by vorticity  $\underline{\omega}$ , within a volume  $V$  can be obtained from

$$P_w(t) = -\iiint_V \rho_0 (\underline{\omega} \times \underline{v}) \cdot \underline{u}_{ac} dV, \quad (1.10)$$

where  $\rho_0$  is the fluid density,  $\underline{v}$  is the fluid velocity and  $\underline{u}_{ac}$  is the acoustic particle velocity. The sign of the triple product  $(\underline{\omega} \times \underline{v}) \cdot \underline{u}_{ac}$  determines whether vorticity acts as an acoustic source or sink. For high Reynolds number, low Mach number flows, Eqn. (1.10) provides efficient method for calculating sound power. In order to show that  $P(t)$  is indeed the rate of acoustic energy production and to examine its range of

applicability, Howe's acoustic power integral was derived from the equation similar to (1.8) as it is shown in Appendix C.

### **1.3.5 Control strategies**

In this section both passive and active control strategies for separated shear flows and acoustic response of the resonator will be reviewed.

Chun and Sung (1996), Leontev et al. (1994), Ziada (2003) and Dandois et al. (2007) among others have investigated effects of local acoustical forcing near the separation edge of the BFS. Achieved resonance resulted in the formation of the large scale vortices, which enhanced entrainment rate, and reduced the reattachment length as compared to the unforced flow. Thus, the most effective frequency was found to be the shedding frequency of the shear layer.

The effective feedback control in suppressing flow-excited oscillations by means of synthetic jets was investigated by Ziada (2003). The control actuator consisted of a synthetic jet generated by loudspeakers and located in the proximity of flow separation. The proposed active control technique reduced oscillation amplitudes up to 35 dB, and proved to be very effective in the considered cases: impinging flow oscillations, flow-acoustic coupling (less effective), vortex-induced lock-in vibration and turbulent buffeting.

There are two major ways to passively control flow-induced tones in the side branches. First, and most effective approach, is to eliminate the resonator by de-tuning or misaligning the side-branches (e.g Ziada and Buhlmann 1992). Second way is concerned with the shear layer and is aimed to minimize or avoid the development of the disturbances by breaking two-dimensionality of the flow (e.g Karadogan and

Rockwell (1983)). The latter can be achieved by implementing various types of vortex generators, spoilers, and splitter plates. Previous researchers have shown that these approaches can decrease sound pressure in a resonant system by a factor of two (Arthurs et al. 2006). In the present study, in order to limit the hydrodynamic interaction of the shear layers and potentially alleviate the intensity of acoustic resonances various splitter plates were placed in the middle of the cross-junction.

#### **1.4 CONTRIBUTIONS**

Previous investigations, summarized in the literature survey, provided substantial insight into separated-reattaching shear flows in the geometries of interest, as well as their potential coupling with acoustic field. Despite these advances, a number of issues remain unresolved. The main contribution of the present dissertation is in the area of flow-acoustic coupling in side-branch resonators. Phase-averaged flow patterns and structures of the acoustic source presented in this work provided detailed quantitative insight into the physics of the flow-acoustic coupling phenomenon. This contributes to better understanding of the acoustic source and can lead to formulation of non-linear models capable of predicting the amplitude of pulsations as a function of the flow velocity.

Specific contributions related to the flow-acoustic coupling phenomenon are listed below:

- 1) This work represents the first quantitative description of the effects of resonator geometry on the associated flow patterns. Bluff rectangular plates placed along the centerline of the main duct in the cross-junction region had significant influence on the degree of hydrodynamic interaction between the

shear layers that formed across the openings of the side branches. At the same time, acoustic modes of the resonator remained unchanged. The first hydrodynamic oscillation mode has been inhibited by the presence of plates, which resulted in substantial reduction of the acoustic pulsation amplitude and the strength of the acoustic source (Velikorodny et al. (2008)).

- 2) Imaging of the flow structures in conjunction with unsteady pressure measurements yielded detailed quantitative flow patterns at various phases of the acoustic oscillation cycle. In contrast to the earlier works, the present study represents the first application of vortex sound theory in conjunction with global quantitative flow imaging and numerical simulation of the two-dimensional acoustic wave field to calculate the acoustic energy generated or absorbed by vortices during a typical oscillation cycle (Oshkai et al. (2008)).
- 3) Several issues related to understanding of flow-acoustic coupling mechanisms has been resolved in this work and reported by Velikorodny et al. (2009a):
  - a) Presence of a wide range of scales of vortical structures in acoustically-coupled side branch flows has not been previously addressed. In the present study, transformation of the small-scale vortices into large-scale structures that are associated with flow-acoustic resonance has been quantified using global quantitative imaging and vorticity thickness in particular.
  - b) Flow-acoustic resonance in side-branch systems is characterized by a sharp peak in the corresponding pressure spectrum. Consequence of variation of inflow velocity on the quality factor of the resonant spectral peak has been addressed.

- c) For the first time , visco-thermal damping and net generated acoustic power of the coaxial side-branch system has been evaluated based on global, quantitative flow imaging data.

The following fundamental and industrial contributions related to the air clamp experiments in proximity to the elastic/solid walls can be summarized as follows:

- 1) In contrast to the classical BFS case, proximity of the curved nozzle and the adverse pressure gradient imposed by the diverging channel geometry resulted in a substantial decrease of the flow reattachment length. In addition, it was demonstrated that transverse profiles of the time-averaged flow velocity and turbulence statistics of the flow in the air clamp share qualitative similarity with the corresponding parameters of diverging channel flows (Velikorodny et al. (2009b)).
- 2) Quantitative flow visualization of Coanda jet flows over a backward-facing step configuration in the presence of an elastic and solid boundary was performed in order to provide the first global, quantitative insight into the underlying physical principles behind the operation of an air clamp device. This investigation provided detailed data sets for validation of numerical models that can be used to improve the air clamp design and to provide guidelines for its operation. Moreover, high-speed photography of the paper motion was implemented in order to characterize its modes of vibration. Consequently, a number of recommendations for the large-scale industrial system were formulated and listed in Appendix F.

## CHAPTER 2

### EXPERIMENTAL SYSTEMS AND TECHNIQUES

In this Chapter experimental systems both for the flow-acoustic coupling and the air clamp projects are described. Quantitative flow imaging (PIV) is first presented separately for each project highlighting their particular aspects and consequently in Section 2.3 to consider its fundamentals.

#### 2.1 SIDE BRANCH RESONATOR

##### 2.1.1 *Overview of the experimental system*

The initial objective of the experimental apparatus shown in Fig. 2.1 was to investigate phenomenon of flow-induced sound in a system with symmetrically located side branches (deep cavities) and to study the influence of the width of the main duct (Yan (2006)). Design of the system was provided by Howard (2004). The flow facility consists of an inlet plenum chamber, a main duct, and an arrangement of the side branches. It allows variations of the channel geometry, optical access to the separated flow area, as well as ability to perform acoustic pressure measurements (as described in the following section). In addition, the flow conditioning and the main duct length provide a fully-turbulent inflow in the vicinity of the cross-junction, which was verified in Section 3.1.2.



splitter plate was placed in the middle of the cross-junction (Fig. 2.2). The narrow main duct with  $D = 6.35\text{mm}$  was utilized in the present experiments.

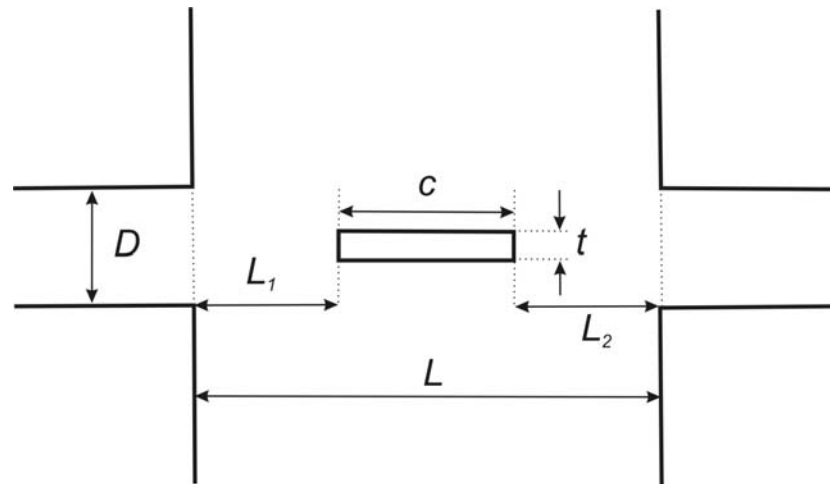


**Fig. 2.2** Close-up of the cross-junction

In the present investigation, the flow features are compared for three cases corresponding to different chord lengths ( $c$ ) of the splitter plates with thickness  $t = 1.85\text{ mm}$  and the out-of plane height of  $25.4\text{ mm}$ . These cases have the following parameters:  $c = 0$  (no splitter plate),  $5$ , and  $10\text{ mm}$  (with chord-to-thickness ratios:  $c/t = 0, 2.7$  and  $5.4$  respectively). Therefore, according to section 1.3.2.5 the last two cases correspond to the 1) and 2) regime of the flows around bluff rectangular splitter plates with low turbulence inflow. In contrast to the earlier studies, a fully-turbulent inflow condition was considered in this work. Besides global cavity length ( $L$ ), other plausible characteristic lengths for the impingement of the shear layers were identified and summarized in Table 2.2.

$c$ (mm)	$L_1$ (mm)	$L_2$ (mm)
0	NA	NA
5	8.3	12
10	5.3	10

**Table 2.2** Characteristic lengths of side branch resonator with splitter plate

### **2.1.3 Acoustic pressure measurements**

Piezoelectric pressure transducers (PCB Model no. 103A02) with a nominal sensitivity 0.21 mV/Pa were used in the experiments. These are high-sensitivity pressure sensors featuring miniature size, built-in electronics and acceleration compensation. These transducers were mounted at the dead ends of the side branch resonator as it is shown in Fig. 2.1.

Acquired pressure signals were transmitted to a National Instruments PXI-4472 data acquisition board with 24-bit resolution and 102.4 kS/s capability, where  $k=10^3$  and S is a number of samples. The maximum frequency of interest was more than 6.5 times less compared to the sampling rate of 8192 Hz, which is in order 12.5 times less than the maximum sample rate of the board (allows to use all 8 channels). It should be noted that frequency of interest for phase-averaged PIV experiments was approximately 877 Hz, which is about 10 times less than the sampling rate. Therefore, at least 10 samples were acquired per cycle at this frequency, which is sufficient for representation of the signal in the time domain and corresponding phase-averaging procedures.

A custom LabView and Matlab codes were employed to process pressure signals and characterize them in the frequency domain. There are a number of parameters involved in the spectral analysis: a) the number of samples per data set; b) the sampling rate; c) the number of data sets to calculate average. The number of samples per data set was calculated according to  $n = f_s / \Delta f$  (where  $f_s$  – sampling rate,  $\Delta f$  – frequency resolution). The  $\Delta f = 0.5\text{Hz}$  was found to adequately characterize the system response. In addition, the time trace of the pressure signal was employed as a phase reference for the image acquisition.

The acoustic pressure signal was not filtered since the NI PXI-4472 board contains a built-in antialiasing capability for each channel that can remove most noise from signals. The analog inputs have both analog and real-time digital filters implemented in hardware to prevent aliasing. Input signals are first passed through fixed analog filters to remove any signals with frequency components beyond the range of the analog-to-digital converters (<45 kHz). Secondly, digital antialiasing filters automatically adjust their cut-off frequency to remove any frequency components above half the programmed sampling rate (National Instruments 2008).

Moreover, in the present set of experiments, the ambiguity of sinusoidal pressure signal was minimised due to the low damping in the system and consequent high amplitudes at the resonant frequencies compared to the higher-order harmonics.

#### **2.1.4 Quantitative Imaging of acoustically-coupled flow**

Flow velocity in the cross-junction region was measured using two-component digital PIV, as it is shown in Fig. 2.3.

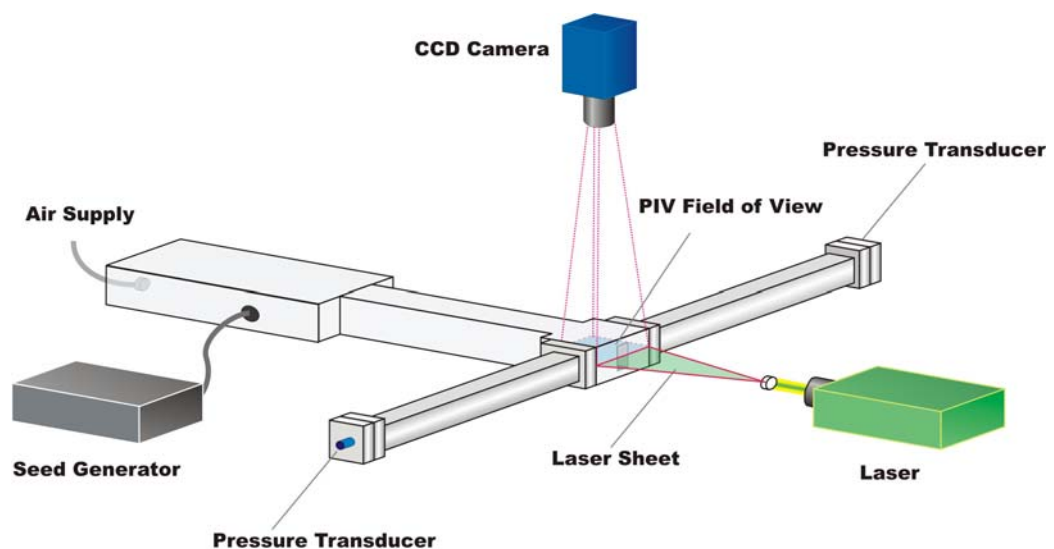


**Fig. 2.3** Schematic of the side branch resonator experimental system with PIV instrumentation

Oil droplets with the typical diameter of approximately 1  $\mu\text{m}$  were used as tracer particles. The Stokes number was calculated according to Eqn. (2.1) from Section 2.3.1. It was found to be  $3 \times 10^{-3}$ , which indicates that the oil particles follow the airflow very well and are a good choice of tracers for this application. The particles were generated using a LaVision atomizer, which employed Laskin nozzles (e.g Raffel et al. (2007)) to generate small air bubbles inside a container with oil. Small oil droplets were generated inside the bubbles and were carried by the bubbles towards the oil surface and subsequently entrained into the air stream leaving the atomizer. The particle concentration was controlled by employing a secondary air inlet to the atomizer, which contained a flow rate regulator. The particles were injected into the inlet chamber that was located upstream of the entrance of the main duct. The inlet chamber contained a honeycomb-type flow straightener, which provided uniform inflow into the main duct and also resulted in homogeneous distribution of the seeding particles in the incoming air stream.

An Nd:YAG dual cavity pulsed laser with a maximum energy output of 2 x 100 mJ/pulse was used to generate a planar light sheet that illuminated the flow tracers. The light scattered by the tracers was captured by a digital camera with a progressive scan charge coupled device (CCD), which had a resolution of 1376 x 1040 pixels. The displacement of the particles was recorded as a pair of single-exposed images. The time delay between the two laser pulses depended on the flow velocity and the magnification factor of the camera lens. The pulse delay was optimized interactively by systematically increasing the pulse separation to minimize the number of outliers within the calculated vector field. The temporal resolution of

the data sets corresponded to 4.9 cross-correlated images per second. The typical raw PIV image obtained during this process is shown in Fig. 2.4.

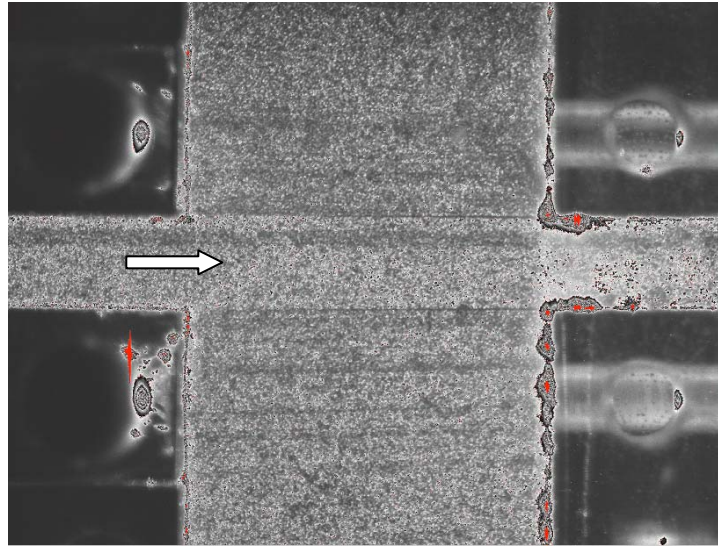


**Fig. 2.4** Raw image of the cross-junction region of the side branch resonator

The recorded sequence of raw images was evaluated using LaVision DaVis 7 software by cross-correlating pairs of frames, each containing single exposures of the group of tracers. A multi-pass adaptive image interrogation algorithm was employed in order to improve the accuracy of the calculated velocity vectors by minimizing the loss of particle image pairs. The algorithm evaluated the particle images in several iterations. Initially, larger interrogation windows (IW) with the size of 128 x 128 pixels were used to determine the local mean particle displacements. Subsequently, smaller interrogation windows were used to improve spatial resolution. The smallest interrogation window had the size of 32 x 32 pixels. Spatial resolution of the velocity vector field of 4.5 vectors/mm was obtained by employing 50% overlap of the interrogation windows and a lens with a focal length of 60 mm.

In the present study, a high-speed PIV system was utilised to provide quantitative measurements of the flow in the cross-junction with bluff splitter plates.

An Nd:YLF dual cavity pulsed, diode-pumped laser with a maximum energy output of 2 x 25 mJ/pulse and up to 10 kHz repetition rate was applied. The high-speed camera features a lens with a focal length of 60 mm in conjunction with a 1024 x 1024 pixel CMOS sensor, providing a physical resolution of 30 pixels/mm. Interrogation window size was initially set to 64 x 64 and subsequently reduced to 16 x 16 pixels. This corresponds to the velocity vector field resolution of 0.35 x 0.35 mm or spatial resolution of 5.7 vectors/mm, which was obtained by employing 50% overlap of the interrogation windows. The system could provide up to 3000 cross-correlated images per second without affecting the field of view of the camera. The phase of acquisition of each velocity field with respect to a typical acoustic oscillation cycle was obtained by recording the trigger signal to the laser together with the acoustic pressure signals. More details on this procedure are provided in Section 2.3.

The erroneous vectors that were replaced by interpolation during the postprocessing stage resulted in bias error of approximately 2%. In addition, precision errors, which are associated with location of the particle displacement correlation peak, accounted for uncertainty of approximately 2%.

## **2.2 AIR CLAMP**

Honeywell Process Solutions proposed to measure thickness of the paper sheet that moves between two domes each containing a laser using a conventional time-of-flight technique. The air clamp described in detail in Fig. 2.6 is embedded into the bottom dome to position the paper sheet with respect to the lasers and to eliminate large-scale vibrations in the system. In reality, paper sheet is not flat, but possesses a certain slope ( $\alpha$ ) due to reasons described in Chapter 3. Moreover, the positions of the

lasers experience misalignment ( $\Delta x$ ) of up to 300  $\mu\text{m}$ , because of the mechanical vibrations in the system. Therefore, an error ( $\Delta h$ ) is introduced as it is illustrated in Fig. 2.5.

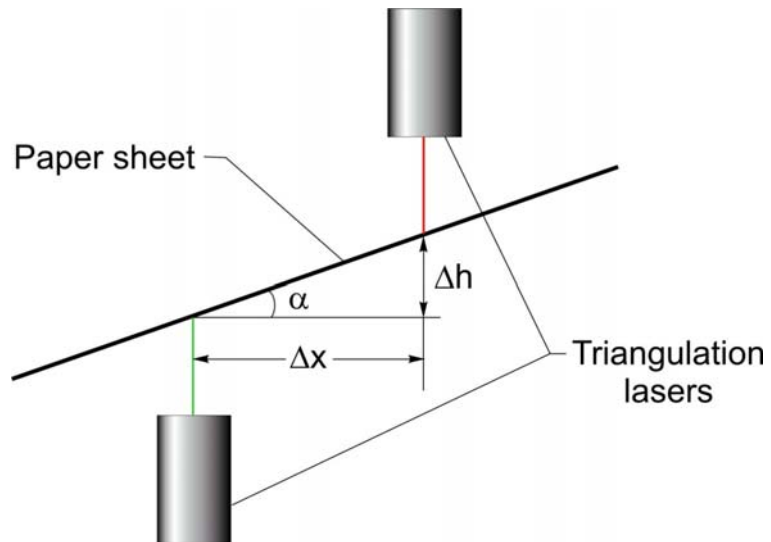


**Fig. 2.5** Error in paper thickness measurements

### 2.2.1 Air clamp apparatus in proximity to the elastic wall

The air clamp apparatus involved a contoured nozzle with the exit width of 0.1 mm that produced a planar wall-bounded jet of air over the air clamp surface. A BFS of height  $h = 0.457$  mm was located at the distance  $D = 2$  mm downstream of the jet exit (Fig. 2.6).

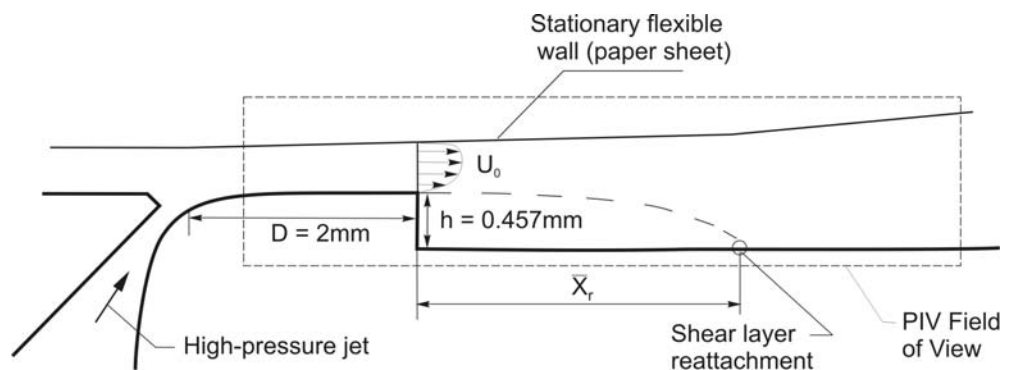


**Fig. 2.6** Schematic of flow configuration in air clamp experimental apparatus

The air clamp had the span-wise (out-of-page) dimension of 76 mm. The flow area between the air clamp surface and the paper sheet had no side walls. The dimensions of the experimental system corresponded to the dimensions of the air clamp in the industrial setting. In contrast to this experimental configuration, approximately an order of magnitude wider paper sheet, which is moving in the streamwise direction at the speed of 28 m/s, was utilized in the industrial manufacturing process.

An experimental apparatus was designed and constructed by Honeywell Process Solutions to investigate air flow through the air clamp in conjunction with a stationary paper sheet. A schematic of the experimental arrangement is shown in Fig. 2.7, while major details can be found in Appendix D. The experimental apparatus provided an opportunity to perform experiments both in the presence of the dome and without it.

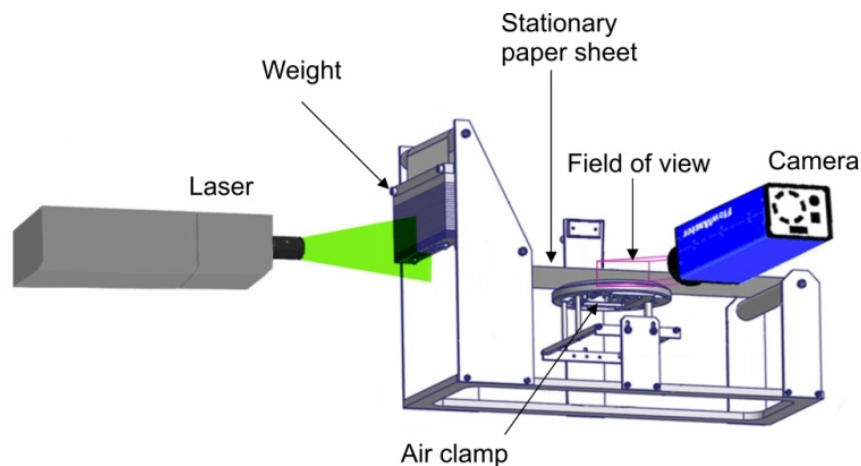


**Fig. 2.7** Schematic of the air clamp experimental system

The schematic shows a sheet retaining device with the air clamp, the tensioned stationary paper sheet with the density  $\rho_p = 55 \text{ g/m}^2$  and the thickness  $h_p = 60 \text{ }\mu\text{m}$ , as well as positions of the laser and the digital camera that were employed for velocity

measurements and visualization of the shape of the paper sheet. The paper sheet, which had the length  $L_p = 508$  mm, was located (in the absence of flow) at the height  $H = 6$  mm above the air clamp surface. PIV and high-speed photography experiments were conducted for a range of inflow velocities (up to 150 m/s, controlled via inlet plenum pressure) and several values of the paper sheet width  $W$ .

The mean air flow in the system was directed towards the laser (from right to left in Fig. 2.7). The experimental system provided optical access for flow visualization as well as a possibility to vary the inflow velocity. Variation of the speed of the incoming jet was performed by changing pressure ( $\Delta p$ ) in the plenum chamber of the air clamp. Moreover, the distance between the air clamp and the paper sheet (in the absence of flow) was adjustable in the range of 1-10 mm. In addition, the system allowed variation of tension per unit width of the sheet by changing its width and/or the amount of the applied weight.

The following configurations were studied experimentally in order to provide insight into the underlying flow physics:

**Case 1:** Coanda jet flow over the BFS without upper boundary (i.e. in the absence of the paper sheet). This configuration served as one of the control cases for experiments that involved flow interaction with the paper sheet. Moreover, this case was used for characterization of the inflow conditions.

**Case 2:** Coanda jet flow over the BFS in the presence of a stationary elastic wall (paper sheet) under variable tension conditions. This configuration is shown in Fig. 2.6. Two characteristic jet velocities were considered for the configuration of Case 2. These flow conditions corresponded to  $\Delta p = 18.6$  kPa ( $U_0 = 100$  m/s) and  $\Delta p = 25.5$  kPa ( $U_0 = 120$  m/s), where  $\Delta p$  is a reference plenum pressure and  $U_0$  is a maximum

time-averaged velocity at the downstream location corresponding to  $x = 0$  (edge of the step). Unless specified otherwise, the data presented in the results sections corresponds to the paper sheet that had a width of 88.9 mm and was subjected to tension per unit of sheet width of 150 N/m. The tension was determined by the hanging weight (indicated in Fig. 2.6) applied to the nominally horizontal paper sheet and corrected to account for the load carried by the rollers (Lakshmana (2004)).

**Case 3:** Coanda jet flow over the BFS in the presence of a solid upper wall. This configuration, which is illustrated schematically in Fig. 2.8, served as a control case and provided an opportunity to characterize the pressure distribution in the diverging channel geometry. In addition, hydrodynamic frequencies associated with the flapping motion of the separated shear layer were measured by piezoelectric transducer mounted in the upper wall. These measurements were subsequently used to quantify hydrodynamic forcing of the paper sheet oscillations corresponding to Case 2.

In all considered cases the nominal quasi-two-dimensional flow assumption was verified by measuring the mean reattachment length at several spanwise locations (planes). The difference in  $\overline{X_r}$  at various stations didn't exceed  $0.3h$ .

### ***2.2.2 Air clamp apparatus in proximity to solid wall***

This section describes important particulars of the control configuration that involved a solid wall in place of the paper sheet. The geometry of the wall corresponded to the time-averaged profile of the paper sheet for the case of  $Re_h = 3000$ . The shape of the paper sheet, which was determined using high-speed photography, is described in detail in Section 3.2.1. The schematic of the experimental configuration involving the solid upper wall is shown in Fig. 2.8.

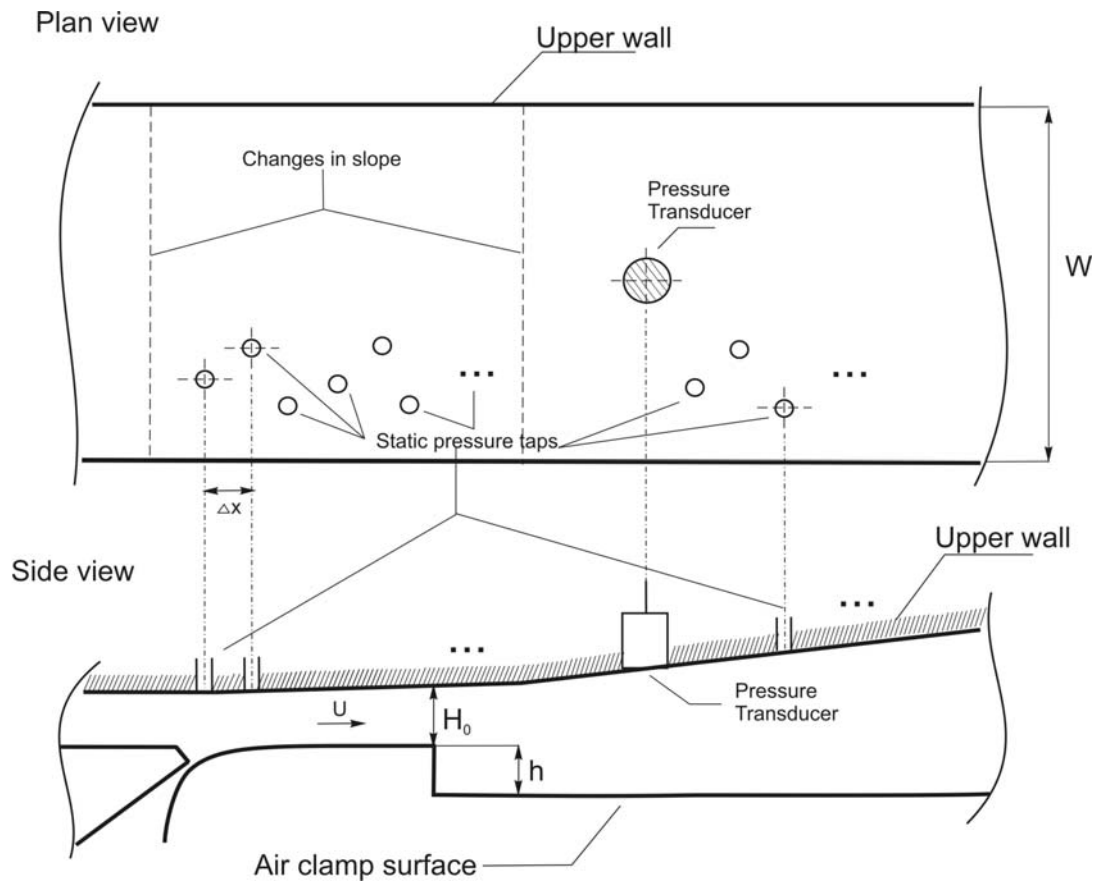


**Fig. 2.8** Side and plan view of the air clamp configuration with solid upper wall

The upper wall contained a piezoelectric pressure transducer and an array of 33 static pressure taps with a typical diameter of 0.125 mm that were distributed downstream of the BFS at the distances  $\Delta x$  from each other ranging between  $\Delta x = 0.27$  mm and  $\Delta x = 0.67$  mm. The distribution of the static pressure along the upper wall was measured by an oil manometer with the accuracy of  $\pm 8$  Pa. The depth-to-diameter ratio of the taps was selected according to theoretical guidelines outlined by Liversey et al. (1962). In order to minimize the static-hole error it is suggested to use the following parameters shown schematically in Fig. 2.9:  $d_s/d_c = 1/14$ ;  $l_s \ll l_c$ ;  $l_s/d_s = 2$ ;

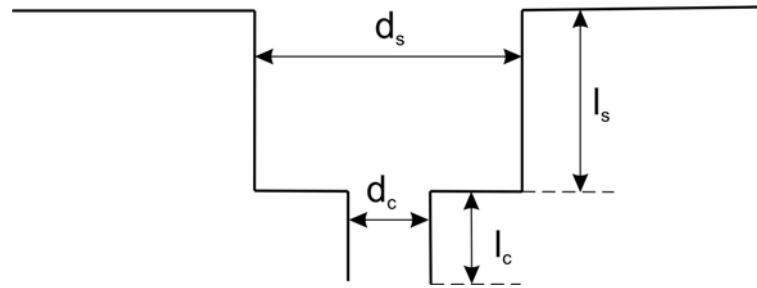


**Fig. 2.9** Characteristic dimensions of a tap for static pressure measurements

The piezoelectric transducer, which was located in the vicinity of the downstream location where the separated shear layer reattached to the bottom wall, had a nominal sensitivity of 0.21 mV/Pa and employed on-board electronics and acceleration compensation. The pressure signals were acquired at the frequency of 32768 Hz using a data acquisition board with a 24-bit resolution. The maximum frequency of interest in the current study (6000 Hz) was 5.46 times lower than the employed data acquisition rate. The pressure signal was acquired for 20 seconds, which provided sufficient number of samples for application of Welch's averaged modified periodogram method (Welsh (1967)).

### **2.2.3 High-speed photography of the paper sheet**

Instantaneous position and shape of the paper sheet during the operation of the air clamp were measured by employing high-speed photography. Images of the oscillating paper sheet, which was illuminated by a pulsed laser, were acquired using a high-resolution complementary metal oxide semiconductor (CMOS) camera at a rate  $F_s = 6$  kHz. The positions of the laser and the camera relative to the air clamp and the paper sheet are shown in Fig. 2.7. The profile of the paper was obtained from the images captured by the camera using a custom Matlab code (Appendix G).

### 2.2.4 Quantitative flow imaging in the air clamp apparatus

Particle image velocimetry was implemented in order to acquire global, quantitative measurements of airflow velocity in the air clamp. The technique involved seeding the flow with tracer particles (oil droplets), which had the nominal diameter of 1  $\mu\text{m}$ . The Stokes number (Eqn. 2.1) for that application was less than 0.3. The particles were generated using a LaVision atomizer and injected into the inlet chamber that was located upstream of the Coanda nozzle. PIV system described in the first part of Section 2.1.4 was employed in the present study. A typical instantaneous image of the flow field is shown in Fig. 2.10.

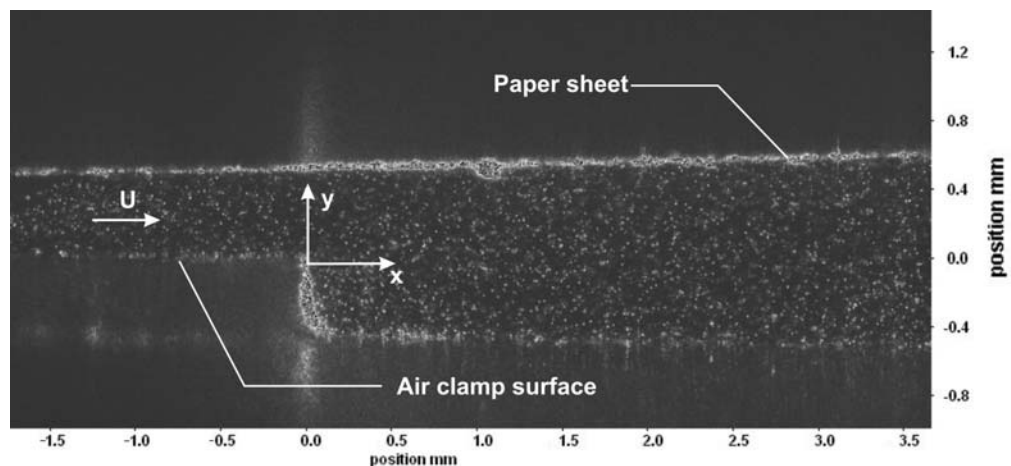


**Fig. 2.10** Raw image of the flow field in the air clamp experimental apparatus. FOV1

Three fields of view (FOVs) were considered in this study. The FOVs corresponded to different magnification factors of the PIV camera and were selected to characterize the distinguishing flow features. The FOV 1 (shown in Fig. 2.8), FOV 2, and FOV 3 had dimensions of 5 x 3.7 mm, 10 x 7.6 mm, and 25 x 18.9 mm respectively. The recorded sequence of images was evaluated using LaVision DaVis 7 software by cross-correlating pairs of frames as described in Sections 2.1.3 and 2.3. In this study larger interrogation windows with the size of 64 x 64 pixels were utilized,

while smaller windows were adjusted for each FOV. The smallest interrogation window size of 16 x 16 pixels for FOVs 1 and 2 and 6 x 6 pixels for FOV 3 was employed in conjunction with a 50% overlap of the interrogation windows to provide physical resolution of 3.6  $\mu\text{m}/\text{pixel}$ , 7.3  $\mu\text{m}/\text{pixel}$ , and 18.2  $\mu\text{m}/\text{pixel}$  for FOVs 1, 2, and 3 respectively, which corresponded to the velocity vector field resolution of 29 x 29  $\mu\text{m}^2$ , 58 x 58  $\mu\text{m}^2$ , and 55 x 55  $\mu\text{m}^2$ . To achieve such resolutions the magnification of the camera (1:2.8) was doubled by deploying the TAMRON SP AF Tele-Converter (300F – FNs 2x). Some experimental issues and constraints associated with this project are summarized in Appendix E.

Location of the particle displacement correlation peak was estimated with approximately 2% precision. The bias error due to interpolation procedures during the postprocessing stage was approximately 7%. Therefore, the total uncertainty did not exceed 10%.

## **2.3 PARTICLE IMAGE VELOCIMETERY AND DATA HANDLING**

### **2.3.1 PIV Fundamentals**

Particle Image Velocimetry (PIV) is a flow visualization technique that can provide a quantitative measurement of the instantaneous flow velocity over a region illuminated by a two-dimensional light sheet. The experimental set-up of a PIV system typically consists of several interacting subsystems. The fluid flow is seeded with tracer particles and illuminated in one plane at least twice within a short time-interval. The images captured by the camera have to be evaluated to determine displacement of particles between the light pulses. In order to handle a data collected employing PIV technique a computer with sophisticated image evaluation and post-

processing algorithms is required. Since the first fundamental reviews on the PIV techniques (e.g. by Adrian (1991), Willert and Gharib (1991)), significant progress in the development of hardware and software enable application of PIV not only in research laboratories, but also in industrial research. One of the most recent comprehensive guide on the digital version of PIV can be found in Raffel et al. (2007).

The PIV technique has several advantages over other flow measurement methods including the following:

1. PIV provides essentially non-intrusive velocity measurements. This allows the application of PIV even in high-speed flows in the vicinity of the wall or/and with shocks, where the flow would be disturbed by the presence of the probe. Careful selection of particle sizes and seeding density ensures negligible interference with the fluid flow. The quantitative measure of the ability of a tracer particle to follow the streamlines of the fluid is the dimensionless Stokes numbers (Hinds (1999)). Particles having  $St \ll 1$  will follow the flow very well, whereas particles with  $St \gg 1$  will not follow the flow at all. The Stokes number is given by

$$St = \frac{\tau U}{L} = \frac{\rho d^2 C_c}{18\mu} \frac{U}{L} \quad (2.1)$$

where  $U$  and  $L$  are characteristic length and velocity of the flow respectively,  $\tau$  – is a relaxation time, which can be expressed as follows:  $\frac{\rho d^2 C_c}{18\mu}$ . In this equation  $\rho$  and  $d$  are the density and typical diameter of the particle,  $\mu$  – is a dynamic viscosity of the fluid and  $C_c$  – is a slip correction factor, which has a value close to unity for considered particle diameters.

2. PIV is a whole field technique. It allows the measurement of velocity in the large parts of the flow field. Resulting global quantitative images have relatively high spatial resolution. The number of independent velocity vectors is commonly determined by the spatial resolution of the sensor and interrogation window size (see Section 2.3.2).

3. PIV can produce real-time velocity maps through use of state-of-the-art digital high-speed cameras and computer hardware. Nowadays, high-speed recording on complementary metal-oxide semiconductor (CMOS) sensors allows acquisition in the kHz-range.

Although rapid development of the PIV is still underway, several limitations should be listed. First, only two-dimensional PIV is considered established technique, meaning that only two (in plane) components of the velocity vector can be determined. Specific methods (stereo techniques, dual-plane PIV) exist to capture third component of the two-dimensional velocity field. Research on the time-resolved tomographic PIV, which is essentially three-dimensional, is currently being pursued (Scarano and Poelma (2009)). Second, PIV technique is limited by a minimum achievable time between image pairs, which results in the limitation on the maximum resolvable speed. Moreover, temporal resolution of a PIV image sequence is limited by the laser repetition rate and the acquisition rate of the camera. Both at this point can't compete with other established techniques. While Raffel et al. (2007) provides thorough review of the state-of-the-art hardware implemented in PIV, the following sections will concentrate on the most important processing techniques embedded into the LaVision DaVis software.

As it will follow from Section 2.3.2 the two major classes of errors types are associated with PIV. These are mean bias (systematic error) and root-mean-square (uncertainty) errors (Huang et al. (1997)). The systematic errors arise due to implementation of cross-correlation algorithm and peak-finding scheme. Uncertainty is generally attributed to the noise in the correlation domain. In practice, however, it is not always possible to distinguish between the two, therefore both systematic and uncertainty errors are combined in the total error.

Often to access the measurement precision of PIV a numerical simulation is utilized (e.g. Willert (1996), Huang et al. (1997)). By varying only a single parameter at a time, artificial particle images of known content are generated, evaluated and compared with known theoretical or experimental result. The particles in the images are positioned randomly, and the evaluation procedure is based on a large number of Monte Carlo simulations. This way effect of particles diameter, particle image density, image quantization levels, background noise and displacement gradient can be accessed (Raffel et al. 2007).

### **2.3.2 Image processing**

The direct cross-correlation function  $\phi'(m, n)$  for two sample regions  $f(m, n)$  and  $g(m, n)$  is given in Eqn. (2.2) (Raffel et al. 2007):

$$\phi'(m, n) = \frac{\sum_{m=-\infty}^{\infty} \sum_{n=-\infty}^{\infty} f(m, n)g(m + x, n + y)}{\sum_{m=-\infty}^{\infty} \sum_{n=-\infty}^{\infty} f(m, n) \sum_{m=-\infty}^{\infty} \sum_{n=-\infty}^{\infty} g(m, n)}, \quad (2.2)$$

where  $f(m,n)$  and  $g(m,n)$  denote image intensity distribution of the first and second image in the pair,  $m$  and  $n$  are coordinates of the interrogation window,  $x$  and  $y$  are pixel offsets between the two images.

The two frame cross-correlation method shown in Fig 2.11 was used in the present study to obtain velocity field. Two sequential images were divided into small interrogation windows (IW) of size  $N$ . Statistical cross-correlation technique was utilized to determine one local velocity vector for each interrogation window. The cross-correlation algorithm based on the Fourier Transform was introduced by Willert and Gharib (1991). This approach takes advantage of the correlation theorem, which states that the cross-correlation of two functions is equivalent to a complex conjugate multiplication of their Fourier Transforms. In practice, the Fast Fourier Transform (FFT) is utilized, which reduces the computations from  $O(N^2)$  for direct cross-correlation procedure to  $O(N \log_2 N)$  operations. When two-dimensional correlations from Fig. 2.11 are considered the efficiency is further increased.

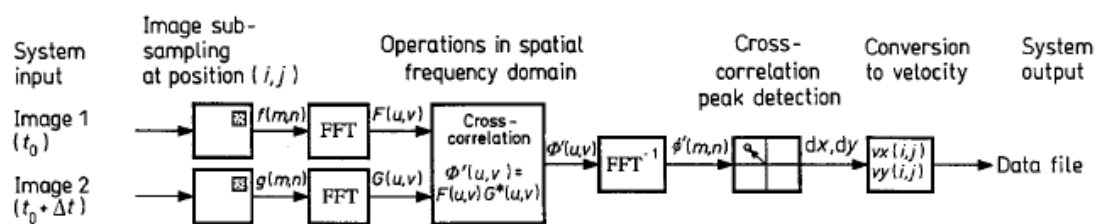


**Fig. 2.11** Flow-chart of DPIV process (Willert and Gharib 1991)

When many particle images match up with their corresponding shifted partners the cross-correlation value ( $\phi'(m,n)$ ) is high (close to unity). The highest peak in the cross-correlation image represents the most probable displacement for the particles within the interrogation window. A variety of methods for detecting location of the correlation peak have been utilized in the past: peak centroid, parabolic peak fit,

Gaussian peak fit. These functions are based on a three point fit, which includes the maximum correlation value and two adjoining values in both directions of the correlation plane. The Gaussian peak estimator proved to be the most efficient, due to Airy type intensity distribution in the particle images. Algorithm can reach accuracies of the order of 0.1 of a pixel. When a local particle displacement vector is found, the local velocity vector can be calculated as the ratio of the displacement vector to the time interval between the two exposures ( $ds/dt$ ).

Although the FFT approach outlined above provides superior computation speed compared to direct methods, some drawbacks should be outlined. First, according to the Nyquist criterion associated with the Fourier transform, the maximum displacement magnitude that can be computed accurately is  $N/2$ . In practice, however, the strength of the correlation peak will decrease with increasing displacement, due to decrease in particle matches. Willert and Gharib (1991) suggest a value of  $N/3$  to be the limit for achieving sufficient accuracy of the displacement vector. A more conservative, but widely adopted value is  $N/4$  (Keane and Adrian 1990). Second, the FFT correlation estimates are biased due to periodicity of the data and appropriate weighting functions have to be used as discussed in the preceding paragraph. In addition, the FFT will be efficient only when it is implemented with a base-2 dimension (i.e.  $32 \times 32$ ).

Two techniques were used in the present study to improve signal-to-noise ratio of the correlation peak, as well as increase spatial resolution of the resulting vector field: adaptive multi-pass processing and interrogation window overlap. In many cases, these procedures allow neglecting the “ $N/4$  rule” and adopting  $N/3$  as an appropriate limit of displacement magnitude (Raffel et al. 2007).

First, the adaptive multi-pass technique was introduced by Westerweel (1997) to correct for the velocity bias. In the flows with high velocity gradients particles from a particular IW in the first image of an image pair will likely exit it by the time the second image is acquired. Thus, there is a bias towards lower magnitude displacement measurements for the two-frame cross-correlation. The adaptive multipass method corrects for this velocity bias by off-setting the IW according to the mean displacement vector. This process is fulfilled in several iterations of the cross correlation algorithm by decreasing the IW size (i.e. from  $64 \times 64$  pixels<sup>2</sup> to  $16 \times 16$  pixels<sup>2</sup>). After each pass of the adaptive multipass process, a regional median filter was applied to eliminate groups of spurious vectors. The median filter computes a median vector from the 8 neighbours and compares the middle vector with this median vector  $\pm$  deviation of the neighbouring vectors. Consequently, it removes vectors that were greater than a certain threshold times the root-mean-square (rms) value of all of their immediate neighbours. All vector groups with less than  $x$  vectors are then entirely removed and empty spaces are filled by bilinear interpolation. Finally, a  $3 \times 3$  pixels<sup>2</sup> window smoothing is automatically performed during the adaptive multipass process.

Second, Hart (2000) introduced a correlation based technique to reduce the impact of false correlation peaks in noisy data by overlapping two neighbouring interrogation windows by 50%. The two overlapping regions are multiplied, which causes amplification of any correlation peaks that are common to both windows and damps any peaks that are not. The method delivers a single averaged displacement vector between the two correlations and reduces the likelihood of acquiring a false vector. Moreover, it increases spatial resolution of the velocity field. It has been shown, however, that in order to use this algorithm with 75% (or more) overlap some

advanced processing methods for oversampled data must be utilized, due to high degree of self-correlation. Thus, interrogation windows with 50% overlap were employed during all experiments reported in this dissertation.

The post-processing scheme was almost identical for all velocity fields calculated during the experiments. Once these vector fields were obtained, a median filter and a bilinear interpolation were applied again. In addition, the images were smoothed using a Gaussian filter with a standard deviation of the kernel of 1.3.

A number of methods exist for interpretation and analysis of the velocity vector fields (Adrian et al. (2000)). Reynolds decomposition method and phase-averaged flow patterns were used in the present investigation and are described in following sections.

### ***2.3.3 Time-averaging procedures***

Pairs of images that were used for calculation of the instantaneous flow patterns were acquired at a frequency of 4.9 Hz for the side branch resonator without splitter plates and air clamp. This rate of data acquisition provided a suitable spacing in time for calculation of the turbulence statistics provided by Reynolds decomposition. In the case of a side branch resonator a set of 200 images was used to calculate the time-averaged streamwise and transverse velocity vector ( $\langle u \rangle$  and  $\langle v \rangle$  respectively), out-of-plane vorticity  $\langle \omega_z \rangle$ , root-mean-square (rms) of the  $u$  and  $v$  component fluctuations ( $\langle u_{rms} \rangle$  and  $\langle v_{rms} \rangle$ ), as well as the Reynolds stress correlation  $\langle u'v' \rangle$ . In the case of the air clamp, sets of 100, 150 or 200 images, depending on the reliable acquisition time (limited by oil accumulation at the surface

of the air clamp), were used to calculate the time-averaged velocity vector of  $\langle \omega_z \rangle$ ,  $\langle u_{rms} \rangle$  and  $\langle v_{rms} \rangle$ , and  $\langle u'v' \rangle$ .

In contrast to the previously discussed cases, a high-speed system was used to acquire both time- and phase-averaged characteristics in the side branch resonator with splitter plates. The acquisition frequency was thus increased to 87 Hz. Nevertheless, since the nominal frequency of oscillation of the cavity shear layer was approximately 877 Hz, this framing rate corresponds to an interval of more than 10 cycles of oscillation. Therefore it also provides a suitable spacing in time for obtaining random samples and calculation of averaged turbulence statistics. In this case, a total of 870 images were acquired. The definition for each of the time averages with  $N$  being the total number of images is as follows:

Time-averaged vector of horizontal and transverse components of velocity:

$$\langle u, v \rangle = \frac{1}{N} \sum_{n=1}^N (u_n(x, y), v_n(x, y)) \quad (2.3)$$

Time-averaged vorticity:

$$\langle \omega \rangle = \frac{1}{N} \sum_{n=1}^N \omega_n(x, y) \quad (2.4)$$

Root-mean-square of u component fluctuation:

$$u_{rms} = \left\{ \frac{1}{N} \sum_{n=1}^N [u_n(x, y) - \langle u(x, y) \rangle]^2 \right\}^{1/2} \quad (2.5)$$

Root-mean-square of v component fluctuation:

$$v_{rms} = \left\{ \frac{1}{N} \sum_{n=1}^N [v_n(x, y) - \langle v(x, y) \rangle]^2 \right\}^{1/2} \quad (2.6)$$

Averaged value of Reynolds stress correlation:

$$\langle u'v' \rangle = \frac{1}{N} \sum_{n=1}^N [u_n(x, y) - \langle u(x, y) \rangle][v_n(x, y) - \langle v(x, y) \rangle] \quad (2.7)$$

Eqns. (2.5)-(2.7) were non-dimensionalized by the maximum time-averaged velocity at the edge of the cavity or step ( $U_0$ ). The statistical error for the second order moments with 95% confidence was calculated to be less than 5%, 2% and 4% for side branch resonator without, with splitter plates and air clamp cases respectively.

#### **2.3.4 Phase-averaging procedures**

The phase of acquisition of each velocity field with respect to a typical acoustic cycle was determined using the trigger signal to the laser, which was recorded together with the acoustic pressure signal. This trigger signal (Q-switch) was provided by a synchronizer unit developed by LaVision Inc.

When the framing rate of the camera is low, Geveci et al. (2003) outlined an approach for obtaining the phase-averaged PIV images. This procedure was implemented in two steps. First, the time trace of the pressure signal was used as a phase reference of image acquisition. The phase difference was defined to be a difference between the occurrence of zero crossing of pressure signal from negative to positive and acquisition of the pair of images. A typical acoustic cycle was divided into five phase intervals (i.e.  $72^\circ$  increment). The images that correspond to the same phase interval were classified as having the same phase. Second, the quantitative position of large-scale vortical structures along the cavity opening (obtained using centroid method) was used to improve the accuracy of phase determination. These steps allowed resolution of the effective phase angle to within  $1.5^\circ$ . The accuracy of

the phase determination using the phase-locking technique (Yan (2006)) was within  $\pm 4^\circ$ .

In contrast to Geveci et al (2003), high framing rate (1 kHz) was utilized in the present experiments. At this acquisition frequency, approximately one image pair was acquired during a period of the acoustic oscillation cycle ( $T=0.0011$ ). The acquisition phase of the image pairs was smoothly varying with time through the acoustic cycle. The custom Matlab code (Appendix G) allowed efficient identification of ten phases and captured corresponding numbers of image frames. Thus, at least one hundred pairs of images at each phase of the acoustic oscillation cycle were stored. The accuracy of the phase was found to be within  $\pm 2.5^\circ$ . The equations employed for phase-averaging are directly analogous to those employed for time-averaging, except that the average is performed for the total number of  $M$  images at a given phase.

## CHAPTER 3

### EXPERIMENTAL RESULTS AND ANALYSIS

#### 3.1 ACOUSTICALLY COUPLED FLOWS OVER SYMMETRICALLY LOCATED SIDE BRANCHES

##### *3.1.1 Numerical simulation of acoustic field*

The 2D-dimensional acoustic field was obtained numerically from a modified two-dimensional Helmholtz equation using Comsol 3.2 software. Under assumption of monochromatic or time-harmonic wave propagation, the wave equation (A7) reduces to Helmholtz equation for acoustic pressure  $p$ , which can be treated as an eigenvalue problem:

$$\Delta p + \frac{\lambda}{c^2} p = 0 \quad (3.1)$$

where  $\Delta$  is a Laplace operator,  $c$  - speed of sound, and eigenvalue  $\lambda = \omega^2 = (2\pi f)^2$ , therefore:

$$f = \frac{\sqrt{\lambda}}{2\pi} \quad (3.2)$$

Solution of the equations (3.1 and 3.2) for the case of the coaxial side branch resonator, results in the eigenfunctions, which correspond to the acoustic mode shapes and eigenvalues, which represent resonant frequencies respectively.

It should be pointed out that an alternative approach to simulating the acoustic field could involve using a low-frequency Green's function as proposed by Howe

(1975). The correct singular behavior of the Green's function at the sharp corners can be obtained by matching the acoustic velocity in the region represented by plane wave propagation to an incompressible potential flow representation.

The amplitudes of the horizontal and vertical components of the acoustic particle velocity  $\underline{u}_{ac}$  were determined from the values of the local acceleration due to fluctuations of acoustic pressure  $p$ , obtained from the numerical model:

$$(u_{ac})_i = -\frac{1}{2\pi f \rho_0} \frac{\partial p}{\partial x_i}, \quad (3.3)$$

where  $f$  is the resonant frequency.

Equation (3.3) is determined from the second Newton's law, where convective acceleration terms are dropped out, due to considerations given in the Appendix A on linearization of Euler's equations.

The boundary conditions at the open ends of the duct were set to zero acoustic pressure. All other surfaces were modeled as solid boundaries. Fig. 3.1 shows the computational domain and boundary conditions for the case of the main duct without splitter plates.

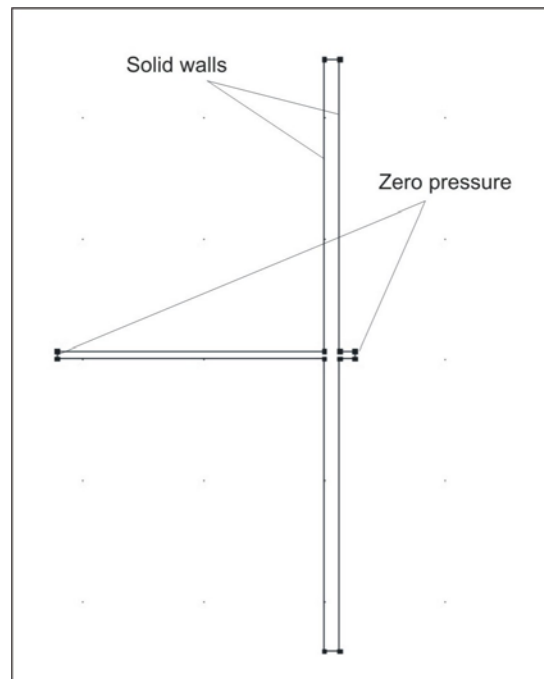


**Fig. 3.1** Computational domain and boundary conditions

A non-uniform computational mesh with a total of 33920 triangular elements was employed to provide adequate resolution. A close-up of the refined mesh in the cross-junction region is shown in Fig. 3.2. The acoustic field defined as the unsteady potential flow component of the velocity field has singularities at the sharp corners of the cross-junction. In order to resolve these singularities numerically, the cross-junction corners were represented by curved elements with a radius of 0.1 mm. The radius of curvature was chosen to be substantially smaller than the resolution of the experimentally-obtained velocity field while ensuring numerical convergence upon grid refinement.

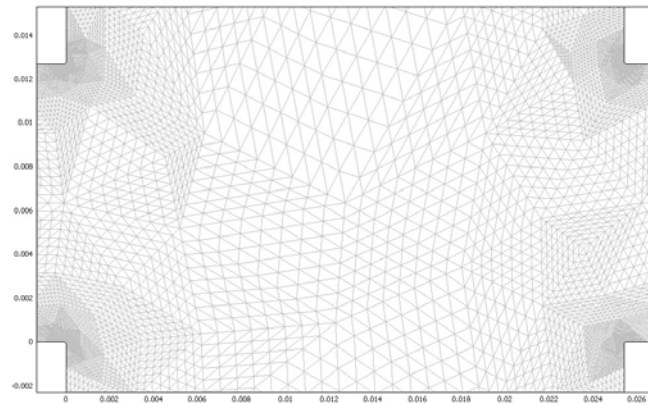


**Fig. 3.2** Close-up of the computational mesh in the cross-junction region

While the numerical simulation yields all mathematically possible eigenvalues, only the modes that correspond to low radiation losses into the main duct can be excited in the physical system. The acoustic modes corresponding to the in-phase oscillation of the pressure in the side branches are strongly damped by radiation along the main pipe and, consequently, are not excited in the experimental apparatus.

Tables 3.1 and 3.2 compare simulated frequencies to those observed in the experiments as well as to the values predicted by Eqn. (1.9) for the cases with- and without a splitter plate respectively. Here  $f_m$  refers to the  $m$ -th oscillation mode. It should be noted that both the theoretical and the numerical predictions of the resonant frequencies are within  $\pm 3\%$  of the measured frequencies of the acoustic modes, which are described in detail in the following section. Splitter plates have no substantial influence on the simulated frequencies and corresponding acoustic modes of the resonator.

$f_{\text{simulated}}$ , Hz	$f_{\text{theoretical}}$ , Hz	$f_{\text{measured}}$ , Hz
$f_1=124$ (124)		
$f_2=175$ (175)	$f_1=177$	$f_1=NA$
$f_3=358$ (358)		
$f_4=432$ (432)		
$f_5=526$ (524)	$f_3=531$	$f_3=528$
$f_6=711$ (711)		
$f_7=793$ (793)		
$f_8=877$ (874)	$f_5=884$	$f_5=877$ (876)
$f_9=1062$ (1062)		
$f_{10}=1169$ (1168)		
$f_{11}=1227$ (1223)	$f_7=1238$	1231(1228)

**Table 3.1** Simulated, theoretical, and measured resonant frequencies for the case of  $c/t=2.7$  ( $c/t=5.4$ )

$f_{\text{simulated}}$ , Hz	$f_{\text{theoretical}}$ , Hz	$f_{\text{measured}}$ , Hz
$f_1=143$		
$f_2=175$	$f_1=177$	$f_1=172$
$f_3=358$		
$f_4=432$		
$f_5=526$	$f_3=530$	$f_3=524$
$f_6=710$		
$f_7=793$		
$f_8=877$	$f_5=883$	$f_5=883$
$f_9=1061$		
$f_{10}=1168$		
$f_{11}=1228$	$f_7=1236$	$f_7=1223$

**Table 3.2** Simulated, theoretical, and measured resonant frequencies for the case without plate ( $c/t=0$ )

Mode shapes corresponding to the first three resonant acoustic modes ( $m = 1, 3,$  and  $5$ ) for the case without splitter plates are shown in Fig. 3.3. This result is consistent with Fig.1.5 from introduction, which shows theoretical expectations for quarter-wave resonator.

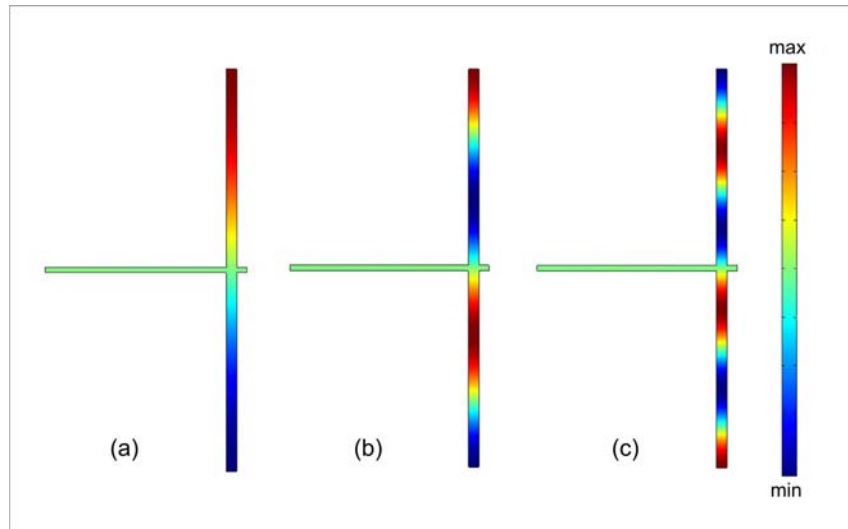


**Fig. 3.3** Resonant acoustic mode shapes corresponding to acoustic pressure for the case of  $c/t=0$ : (a) first mode ( $f = 175$  Hz); (b) third mode ( $f = 526$ Hz); (c) fifth mode ( $f = 879$  Hz)

The numerically simulated pressure mode shapes that are shown in Fig. 3.3 were used to calculate the magnitudes of the acoustic velocity corresponding to three resonant acoustic modes. The acoustic velocity was determined from the values of the local acceleration due to fluctuations of acoustic pressure (Eqn. 3.3). It was found to be  $\pi/2$  radians out-of-phase with the fluctuations of the acoustic pressure.

Distributions of the amplitude of the horizontal and vertical components of the acoustic particle velocity  $\underline{u}_{ac}$  in the cross-junction region without splitter plates are shown in Fig. 3.4.

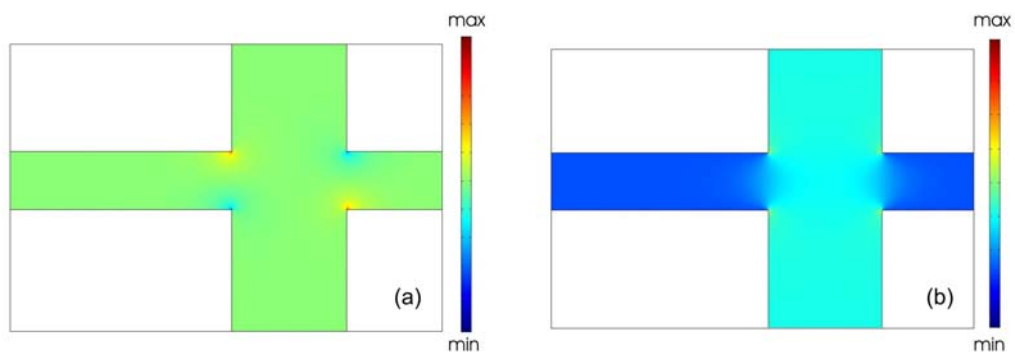


**Fig. 3.4** Amplitude of the horizontal and the vertical components of acoustic velocity ( $c/t=0$ ): (a)  $(U_{ac})_x$ ; (b)  $(U_{ac})_y$

It can be seen that the acoustic wave deviates from the one-dimensional plane wave approximation, due to presence of acoustic fluxes into the main duct (x-direction). Low values of the horizontal component of the acoustic velocity  $(U_{ac})_x$  are observed in the side branches and in the main duct. This effect corresponds to the low values of acoustic losses into the main duct that were reported for similar configurations by Arthurs et al. (2006) and Ziada and S. Shine (1999) among others. However, elevated values of the horizontal acoustic velocity  $(U_{ac})_x$  are observed in the vicinity of the corners of the side branches. Pattern of the vertical component of the acoustic velocity  $(U_{ac})_y$  shown in Fig. 3.4(b) also exhibits deviations from the one-dimensional wave propagation pattern in the vicinity of the leading and trailing corners of the cross-junction. Previously developed semi-empirical approaches for acoustic power calculation (Oshkai and Yan (2008)) employed a one-dimensional acoustic model, which did not account for variations of the acoustic velocity in the vicinity of the corners. While affecting the spatial structure of the acoustic noise source, this non-zero acoustic velocity corresponds to relatively low values of acoustic flux into the main duct and therefore to negligible acoustic radiation. In the real systems some radiation may, however, occur in the downstream direction due to presence of the turbulent flow along the main duct. Thus, downstream of the cross-junction acoustic energy might leak out, especially, because the open pipe termination is very close to the side branch cavity. This hypothesis will be examined in the section 3.1.2.6.

### **3.1.2 Inflow conditions**

One of the objectives of this investigation was to characterize the development of organized shear layer oscillation from the incoming turbulent flow. Existence of the harmonic flow oscillations in systems involving deep cavities has been reported in several earlier studies, including Ziada and Buhlmann (1992) and Kriesels et al. (1995), among others. When the incoming flow is laminar, self-sustained oscillations can develop even in the absence of acoustic resonance. The present investigation demonstrated that coupling of the hydrodynamic instability with a resonant acoustic mode of the side branch resonator can result in large-scale vortex formation even in the case of a turbulent inflow.

PIV data were used to verify the traditional semi-logarithmic distribution of the mean two-dimensional velocity immediately upstream of the leading edge of the bottom side branch. A set of 200 instantaneous velocity fields, which was acquired at a frequency of 4.9 Hz, was ensemble-averaged to produce time-averaged velocity distribution. Plots of the dimensionless velocity distribution as a function of the characteristic wall coordinate  $y^+$  are given in Fig. 3.5 for the case of  $c/t=0$ .

The filled and open symbols correspond to the cases of the first and second hydrodynamic modes of the shear layer oscillations ( $(H_1)_L$  and  $(H_2)_L$ ) respectively. These shear layer oscillation regimes are described in detail in the subsequent sections. The velocity distribution was found to be in agreement with established results Pope (2000). It should be noted that due to optical inaccessibility, PIV data were not available in the immediate proximity to the wall.

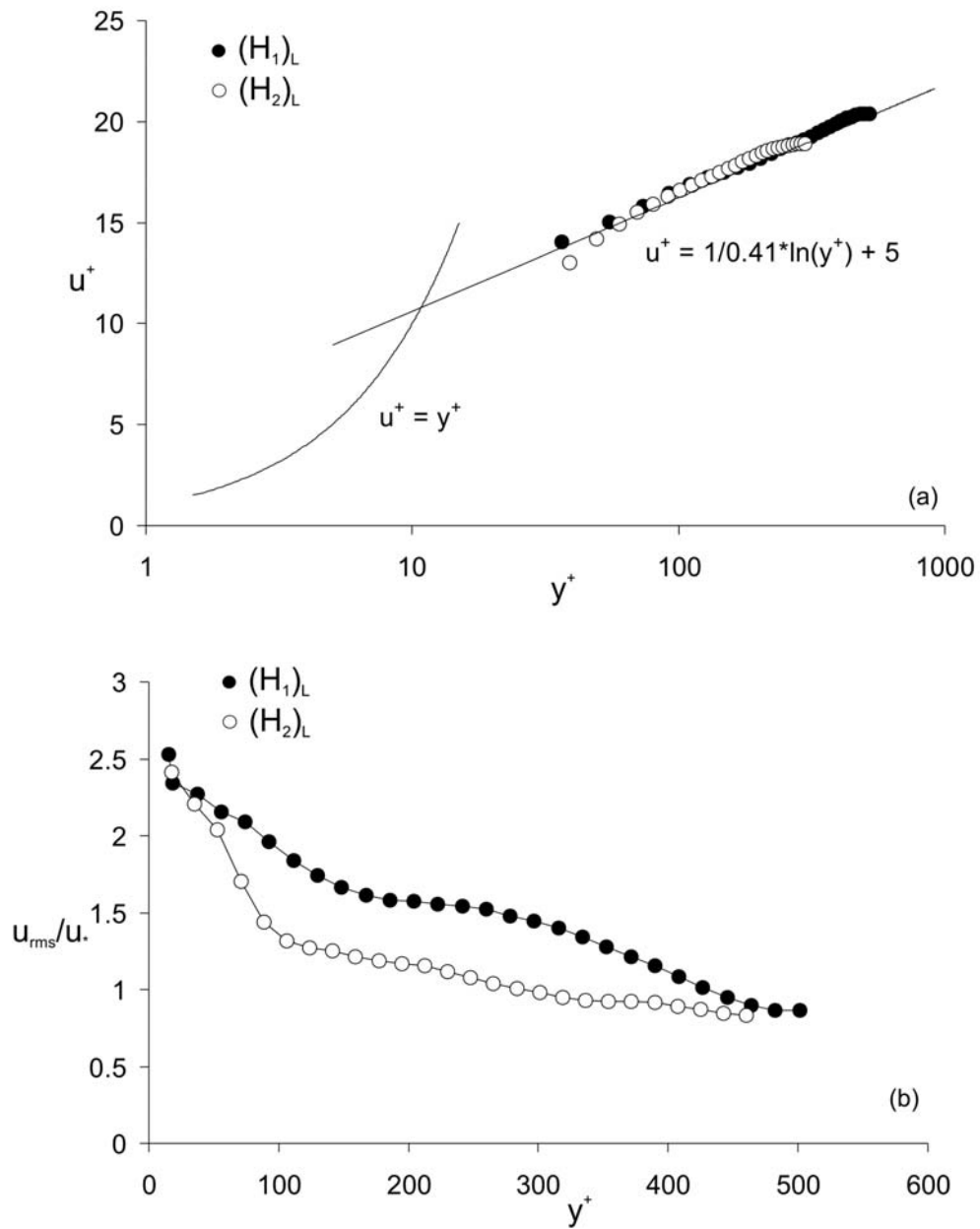


**Fig. 3.5** Variation of flow velocity (a) and root-mean-square velocity (b) normalized by wall friction velocity  $u_*$  at the exit of the upstream section of the main duct for the cases of the first hydrodynamic mode  $(H_1)_L$  and second hydrodynamic mode  $(H_2)_L$  ( $c/t=0$ )

### ***3.1.3 Characterization of the effect of resonator geometry via experimental measurements***

#### ***3.1.3.1 Overview of acoustic response***

The measured frequency and the pressure amplitude for the configuration without the splitter plate are plotted in Fig. 3.6 as functions of the flow velocity in the main duct. The data points shown in the plot correspond to the points of maximum pressure amplitude at each velocity value.

It is observed that when the flow tone is generated, it is not associated with a single value of velocity, but rather with a range of velocities. There exists a minimum threshold velocity, which is required to excite the resonance. The resonance is observed to occur over three ranges of flow velocity. The frequency of the dominant resonant mode switches from the first to the fifth acoustic mode as the flow velocity  $U$  reaches approximately 31 m/s. The corresponding pressure at this point reaches 101 dB. Subsequently, the dominant frequency switches to the third mode at 39 m/s, and then to seventh acoustic and second hydrodynamic mode at 43 m/s. The maximum resonance amplitude is approximately 120 dB.

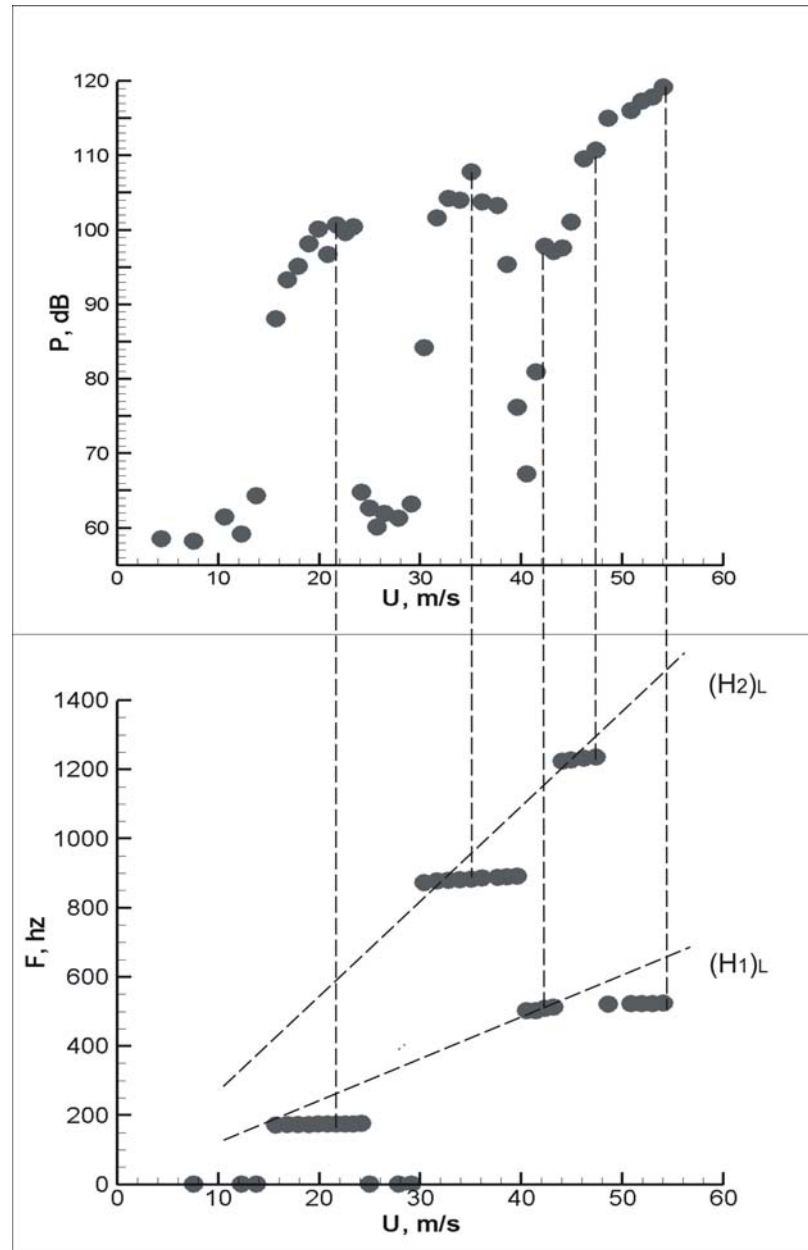


**Fig. 3.6** Pressure amplitude and frequency as functions of incoming velocity ( $c/t=0$ ).

The following formula that is based on linear stability analysis, was used to calculate frequencies of hydrodynamic (Strouhal) modes of the shear layer oscillation.

$$f = \frac{U_c}{U} \left( n_s - \frac{1}{4} \right) \left( \frac{U}{L_{eff}} \right), \quad (3.4)$$

where  $f$  is the shear layer oscillation frequency,  $U$  is the mean flow velocity,  $U_c$  is the convective speed of the vortices,  $n_s$  is the hydrodynamic (Strouhal) mode number that indicates the number of vortices formed in the shear layer during a typical oscillation period, and  $L_{eff}$  is effective length of the cavity. In the present investigation a value of 0.4 was used for  $U_c/U$  in the calculation of the hydrodynamic frequencies in the case without plate.

The diagonal lines labeled as  $(H_1)_L$  and  $(H_2)_L$  in Fig. 3.6 correspond to the calculated first and second hydrodynamic (Strouhal) modes, with  $L$  (cavity length) being the characteristic length. Both calculated hydrodynamic modes ( $(H_1)_L$ ) and  $(H_2)_L$ ) provide a good fit to the measured frequencies.

Considering the response of the resonator in the presence of a short splitter plate ( $c/t = 2.7$ ), it can be observed in Fig.3.7 (and confirmed by flow visualization) that only the second hydrodynamic oscillation mode results in tone generation. When a splitter plate is present in the cross-junction region, the maximum pressure amplitude decreases to 115 dB. Frequencies of the hydrodynamic shear layer oscillation modes (Strouhal modes) as functions of flow velocity were calculated using Eqn. (3.4) and several values of effective cavity length ( $L_{eff} = L, L_1, L_2$ , and  $c$ , as they are defined in Fig. 2.4).

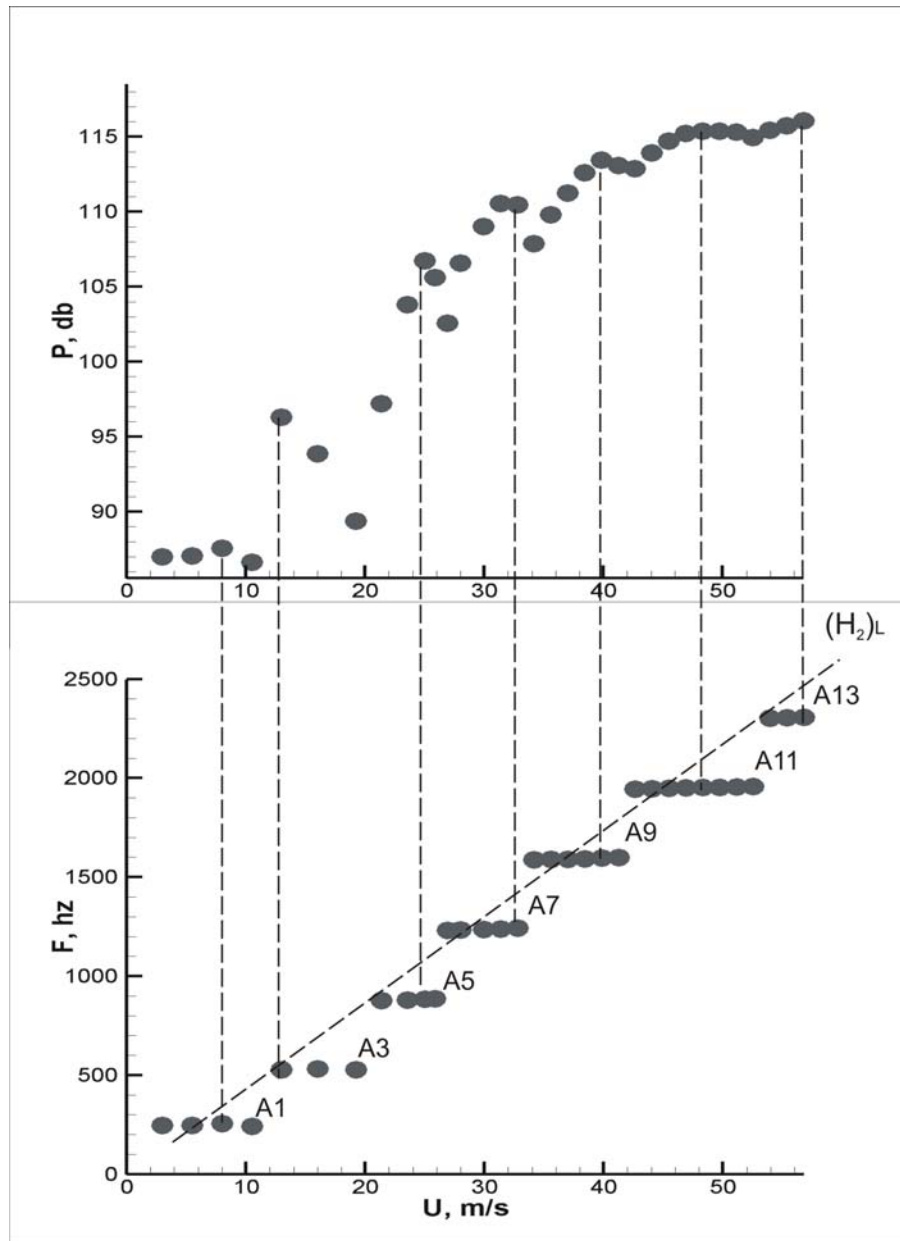


**Fig. 3.7** Pressure amplitude and frequency as functions of incoming velocity ( $c/t = 2.7$ )

It should be noted that the experimental data corresponds to the hydrodynamic mode that is based on  $L_{eff} = L ((H_2)_L)$  and  $U_c / U = 0.61$ , while hydrodynamic modes that were calculated using the values of  $L_{eff} = L_1$ ,  $L_{eff} = L_2$  and  $L_{eff} = c ((H_2)_{L1}, (H_2)_{L2}$  and  $(H_2)_c$ ) over-predict the experimental data for various values of convective speed. Relatively high values of convective speeds ( $0.61U$ ) are attributed to the presence of

splitter plate and the consequent need to satisfy momentum balance. Although, frequencies that were calculated based on  $L_{eff} = L_1$  do match experimental data with a low convective velocity when first hydrodynamic mode is used, there is no evidence of such obtained from flow patterns (Section 3.1.3.3), which further underlines the importance of flow visualization.

In the case of a long ( $c/t = 5.4$ ) splitter plate (Fig. 3.8), the data trend remains qualitatively similar to the case of  $c/t = 2.7$ . The Strouhal (hydrodynamic) mode of the shear layer oscillation also corresponds to a characteristic length  $L_{eff} = L$  (the distance between the upstream edge and downstream edge of the side branch). The maximum pressure amplitude further decreased to 112 dB.

In general, for all three cases, the best correspondence between the calculated Strouhal mode and the experimental data results when the distance between the upstream and downstream edge ( $L_{eff} = L$ ) is utilized for evaluation of the hydrodynamic shear layer frequencies. It should also be noted that the presence of the splitter plate did not significantly affect the theoretically predicted acoustic modes of the system, while hydrodynamic features were significantly affected. As a result first hydrodynamic mode was suppressed and maximum pressure generated e.g. at fifth acoustic mode decreased, which can be explained as follows. Generation of vorticity around the splitter plate affects the amount of energy that is transferred between the vorticity-bearing flow and the resonant acoustic field. Therefore, the maximum values of acoustic pressure decrease as the splitter plate length is increased. Also it should be noted, that absence of the first energetic hydrodynamic mode in the presence of plates

led to the decrease of 5-9db in maximum pressure even at highest (achievable) velocity values (~56 m/s).

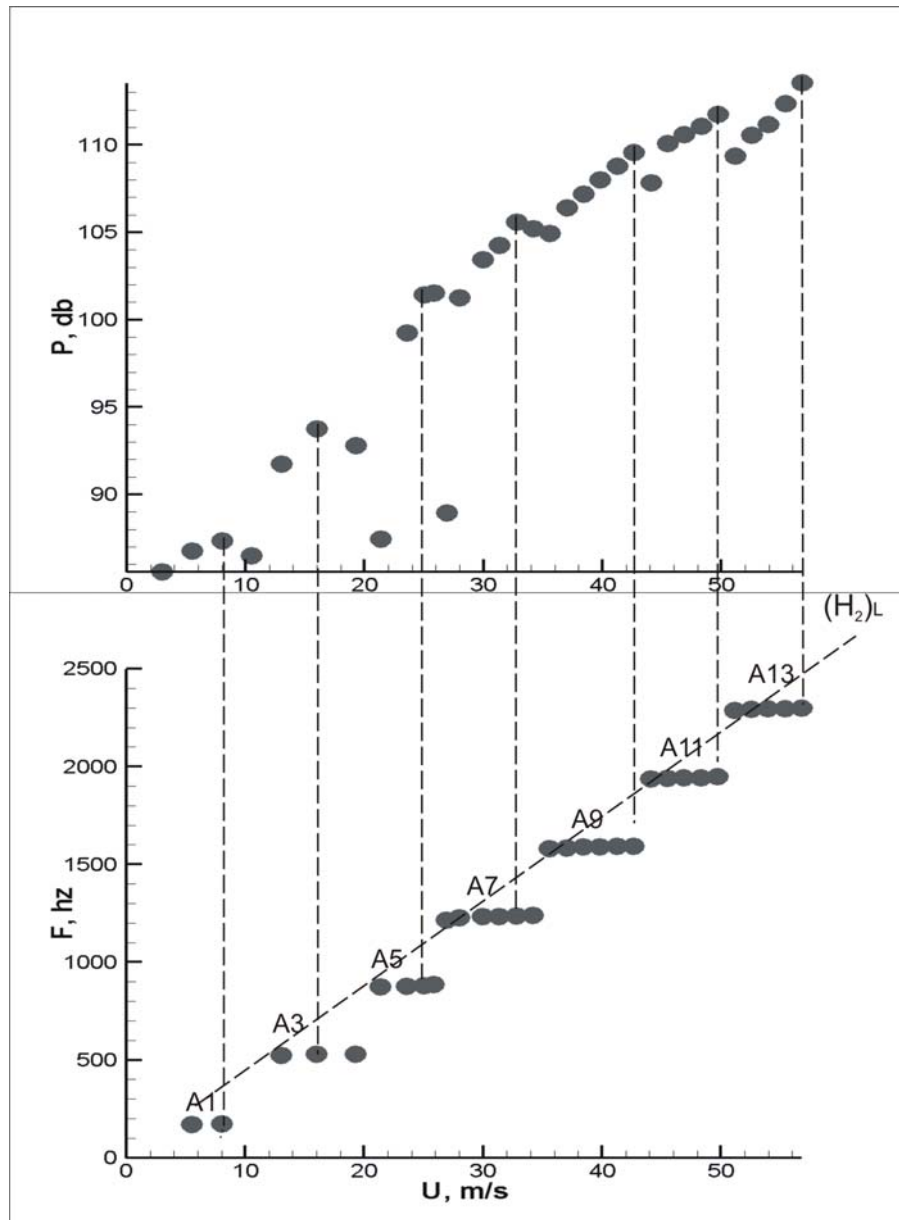


**Fig. 3.8** Pressure amplitude and frequency as functions of incoming velocity ( $c/t=5.4$ )

### 3.1.3.2 Q-factor of the resonator

The onset of resonance can be characterized in terms of the quality factor  $Q$  of the system (defined in Fig. 3.9):  $Q = f_0 / (f_2 - f_1)$ , where  $f_0$  is the frequency corresponding to the dominant pressure peak, and  $f_1$  and  $f_2$  are the values of frequency below and above the resonant frequency  $f_0$  respectively, at which the value of the power spectral density of the pressure signal is equal to one half of the corresponding dominant value.

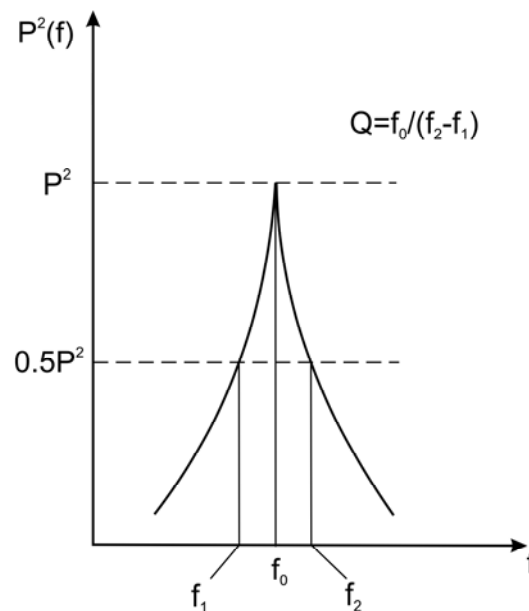


**Fig. 3.9** Definition of  $Q$ -factor

Response of a fluid resonator that is excited by an incoming turbulent flow is analogous to that of an elastically mounted body buffeted by a turbulent flow. Rockwell et al. (2003) employed this mechanical analogy to characterize acoustic response of shallow cavity resonators. In a simple mechanical oscillating system that has a mass  $m$ , a spring with a stiffness  $C$ , and a dashpot with a damping coefficient  $R$ , the  $Q$ -factor is determined by the damping coefficient. If the  $Q$ -factor is large, the oscillation amplitude is large due to the lightly-damped nature of the system and vice

versa. Similar relationship between the  $Q$ -factor and the oscillation amplitude exists in the case of a distributed mass resonator. Generally speaking, fluid resonators of a standing wave type can be viewed as distributed oscillating systems. Therefore, by analogy with a mechanical oscillator, a side branch fluid oscillator will exhibit a certain value of the  $Q$ -factor corresponding to a given frequency  $f_0$ , when it is buffeted by turbulent inflow.

The  $Q$ -factor value corresponding to the no flow condition, which hereafter will be referred to as the  $Q$ -factor of the resonator, provides an upper bound for the  $Q$ -factor values in the absence of the flow-acoustic resonance. For this value to be exceeded, a physical mechanism for inducing the increased pressure amplitude response (i.e. the flow-acoustic coupling) must be present. Thus, the  $Q$ -factor values above the  $Q$ -factor of the resonator can be interpreted as a criterion for the presence of flow-acoustic resonance. The  $Q$ -factor of the resonator can be determined experimentally using loudspeaker excitation in the absence of mean flow Rockwell et al. (2003). In this procedure, the loudspeaker excitation is abruptly terminated, and the decaying pressure amplitude is recorded. The  $Q$ -factor is then calculated according to  $Q = n_0\pi$ , where  $n_0$  is the number of oscillation periods required for the pressure signal to decay to  $1/e$  of the original amplitude. Alternatively, the  $Q$ -factor of the resonator can be calculated from the power spectral density of the resonator response to band-limited white noise excitation. In the present study, the  $Q$ -factor of the resonator ( $Q = 80$ ) was calculated according to Eqn. (3.12). Generally, similar values ( $Q = 70 - 120$ ) were obtained using the experimental approaches for shallow cavity and single side branch resonators (Yang et al. (2009)).

The pressure spectra obtained in the present experiments occasionally exhibited comb-like structures, as shown in Fig. 3.10. The following procedure was implemented to calculate the  $Q$ -factor of the measured pressure peak (see Appendix G for Matlab code). Frequency  $f_0$  corresponded to the global maximum of  $P^2$  within the range of frequencies containing the spectral peak (520 Hz – 535 Hz for the peak shown in Fig. 3.10). Within the same range, frequency  $f_2$  was calculated by averaging the lowest and the highest frequencies corresponding to the pressure level of  $0.5 P^2$  above  $f_0$ . Similar averaging, but involving the frequencies below  $f_0$ , was used to calculate the value of  $f_1$ . It should be noted that in the case shown in Fig. 3.10, a single point at the level  $0.5 P^2$  existed below  $f_0$ . Therefore, no averaging was necessary to evaluate  $f_1$ . Subsequently, the  $Q$ -factor was calculated according to the definition given in Fig. 3.9:  $Q = f_0 / (f_2 - f_1)$ .

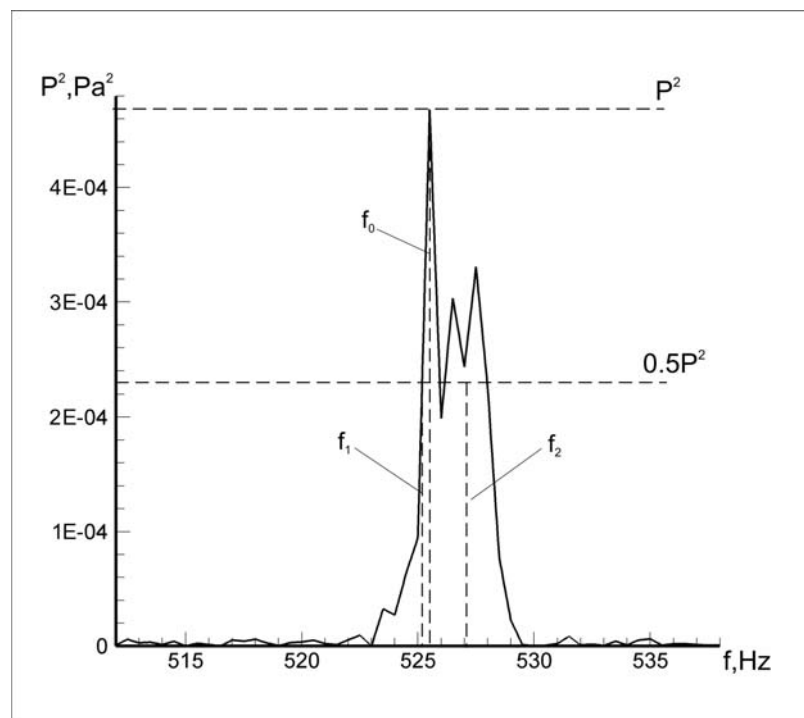


**Fig. 3.10** Typical pressure spectrum with comb-like structure. Dashed lines correspond to parameters used for calculation of the  $Q$ -factor.

The plot of Fig. 3.11 shows variation of the  $Q$ -factor of the pressure peak as a function of the flow velocity. The locked-on flow tones exhibited pressure peaks with high values of  $Q$ -factor ( $Q > 1000$ ). The dominance of the first shear layer oscillation mode is in agreement with the findings of Arthurs et al. (2006). The values of the  $Q$ -factor prior to the onset of the lock-on ( $Q < 80$ ) were in the general range of the  $Q$ -factor values of the shallow cavity-pipeline system in the absence of resonance ( $70 \leq Q \leq 120$ ) reported by Rockwell et al. (2003). Significant pressure amplitudes occurred at the frequency of the seventh acoustic mode ( $f = 1200$  Hz) and were associated with the second hydrodynamic mode ( $(H_2)_L$ ) for the range of flow velocities between  $U = 43$  m/s and  $48$  m/s. The highest values of the  $Q$ -factor ( $Q \approx 2400$ ) were observed in this velocity range.

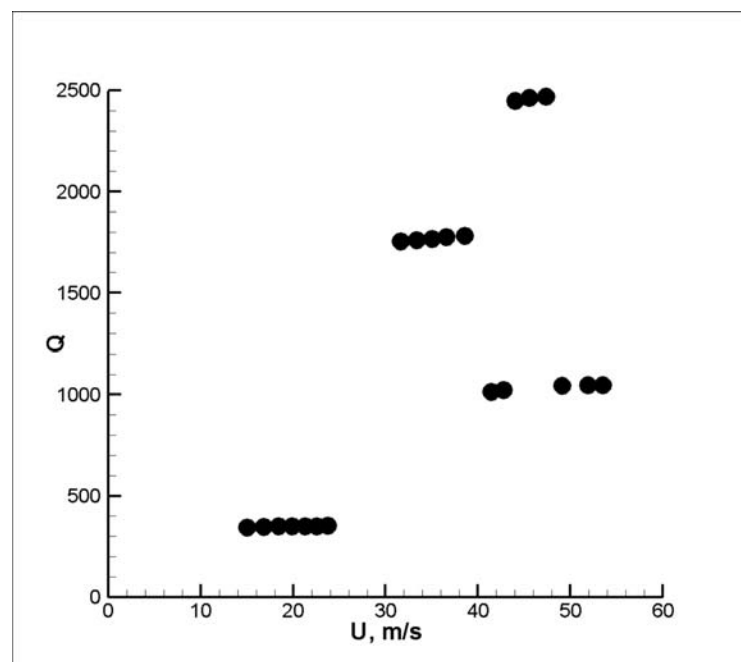


**Fig. 3.11** Variation of quality ( $Q$ ) factor of predominant pressure peak as a function of flow velocity:  
 $c/t=0$

It should be noted that  $Q$ -factors calculated for cases involving splitter plates (not shown) have similarly to the case without plate followed the frequency response trend shown in Figs 3.6-3.8. This fact is attributed to the strong dependence of the  $Q$ -factor and frequency in the considered framework.

The large values of the  $Q$ -factors of the predominant pressure peaks observed in the present experiments at resonance indicate that the side branch oscillator is nearly harmonic. This observation is consistent with the concept that periodic formation of large-scale vortical structures in the oscillating shear layers is the main source of generated sound. It should be noted that this harmonic oscillation of the shear layer occurs on the turbulent background of the fully-developed incoming flow.

### 3.1.3.3 Overview of flow patterns

#### 3.1.3.3.1 Instantaneous flow patterns

An insight into the physics of the acoustically-coupled shear layers and their interaction with the splitter plates is provided by global quantitative flow imaging using PIV. Figs. 3.12 and 3.13 provide an overview of the out-of-plane vorticity distribution for the cases of  $c/t=0$ ,  $c/t=2.7$  and  $c/t=5.4$  respectively.

Images presented in Fig. 3.12 correspond to the first and second hydrodynamic mode of the shear layer oscillation, when respectively one and two large-scale vortices form in the shear layer during a typical oscillation cycle. For the case of the first hydrodynamic oscillation mode, the mean flow velocity is 50m/s and the acoustic frequency  $f = 524$  Hz, which yields a Strouhal number of  $Sr = fL/U = 0.26$ . The observed value of the dimensionless acoustic velocity  $U_{ac}/U$  for this case can be estimated to be 0.001. Assuming planar acoustic wave propagation inside the

side branches, the acoustic velocity amplitude  $U_{ac}$  can be determined from the acoustic pressure amplitude  $P$ :  $U_{ac} = P / \rho_0 c_0$  (Eqn.A10), where  $\rho_0$  is the mean fluid density and  $c_0$  is the speed of sound.

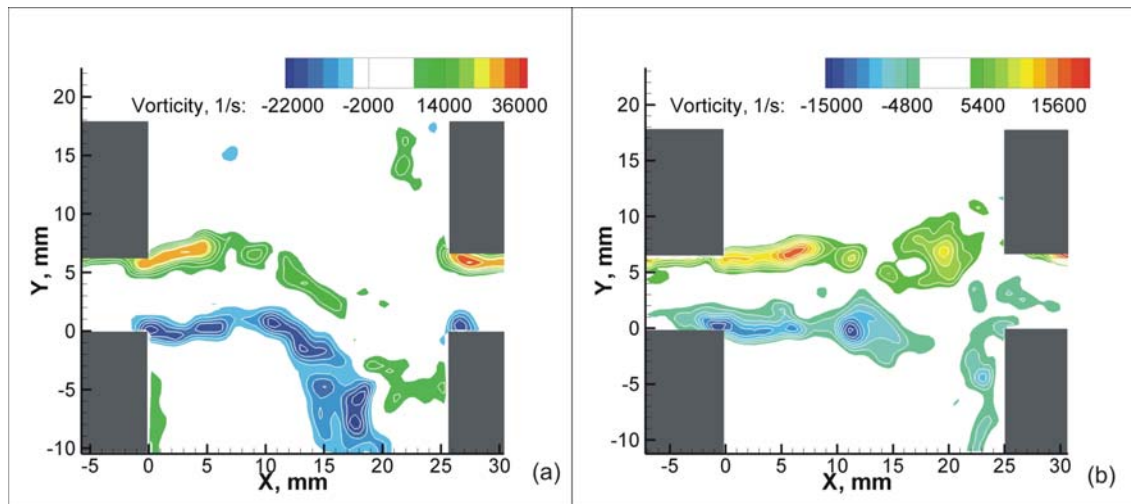


**Fig. 3.12** Pattern of instantaneous out-of-plane vorticity corresponding to the first (a), ( $Sr = 0.26$ ,  $U = 50$  m/s) and second (b), ( $Sr = 0.72$ ,  $U = 31$  m/s) hydrodynamic modes for the  $c/t=0$  case.

In the case of the second hydrodynamic mode shown in Fig. 3.12(b), the mean flow velocity is  $U = 31$  m/s and the acoustic frequency  $f = 877$  Hz, which yields a Strouhal number of  $Sr = fL/U = 0.72$ . The observed value of the dimensionless acoustic velocity  $U_{ac}/U$  for this case can be estimated to be 0.00035, which is substantially lower than in the previous case.

The vorticity plots illustrate formation of large-scale vortical structures in the separated shear layers. As the vortices are convected downstream along the cavity opening, their peak vorticity is decreased, but the overall circulation values increase due to a larger spatial extent and higher convective speed. The vorticity plots show that the shear layer oscillation coupled with an acoustic mode drastically increases the oscillation amplitude for the case of the first hydrodynamic mode, while in the case of the second mode they are less pronounced.

Cases involving the splitter plates presented in Fig. 3.13 for  $c/t = 2.7$  and  $c/t = 5.4$ . These flow patterns correspond to the second hydrodynamic mode of the shear layer oscillation, which is consistent with the acoustic response of the resonator.

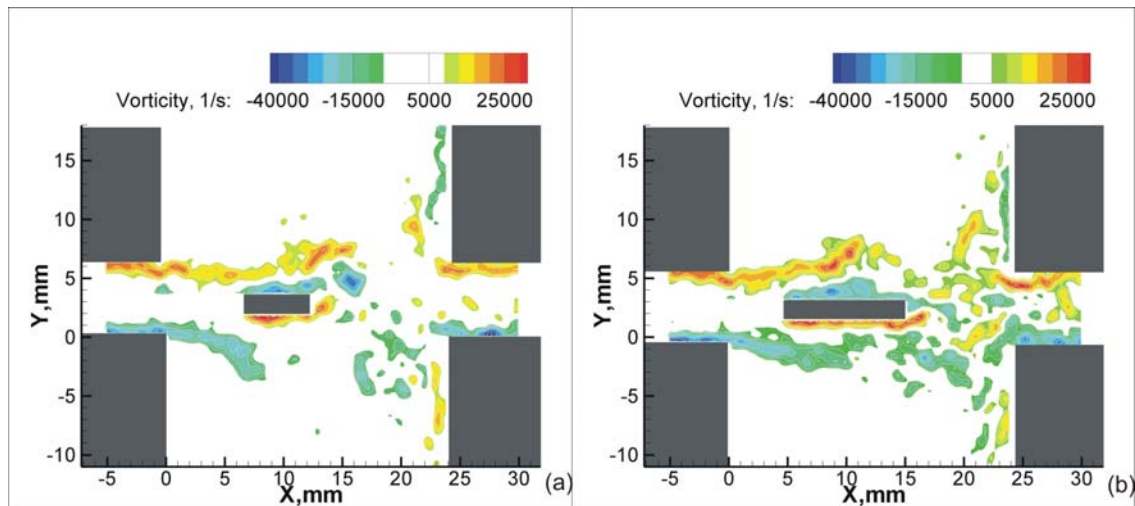


**Fig. 3.13** Pattern of instantaneous out-of-plane vorticity corresponding to the second hydrodynamic mode for the cases of  $c/t = 2.7$ ,  $Re_t = 3500$ ,  $Sr = 0.78$  (a) and  $c/t = 5.4$ ,  $Re_t = 3500$ ,  $Sr = 0.78$  (b).

The mean flow velocity in these cases is  $U = 28$  m/s and the acoustic frequency  $f = 877$  Hz, which yields a Strouhal number of  $Sr = fL/U = 0.78$ . The dimensionless acoustic velocity  $U_{ac}/U$  can be approximated to be 0.0005. The presence of the splitter plates significantly affects the dynamics of the shear layers along the entire span of side branches. Hydrodynamic interaction between the vortices in the upper and lower shear layers is substantially limited, while separation at the leading edge of the splitter plate significantly alters their dynamics by deflecting the path of the shed vortices.

Flow pattern of Fig. 3.13(b) show formation of the separation bubble along the upper and lower surfaces of the splitter plate, which is consistent with regime (3) described in Section 1.3.2.5. For the case of  $c/t = 2.7$ , it can be seen in Fig 3.13(a) that the shear layers form at the leading edge of the plate reattach in the vicinity of the

trailing edge, which corresponds to regime (2). The following section describes these processes in more detail.

### 3.1.3.3.2 Phase-averaged flow patterns

In addition to the instantaneous flow measurements, implementation of analysis of measured acoustic pressure in conjunction with DPIV imaging resulted in a series of global quantitative images of the acoustically coupled flow that show formation and propagation of large-scale vortices during a typical acoustic cycle. Figs. 3.14 and 3.15 show the phase-averaged flow patterns for the three values of the splitter plate chord length at two phase's  $\varphi$  of the acoustic cycle. These flow patterns were obtained by ensemble averaging of up to 100 DPIV images that were acquired at the same phase of the acoustic pressure oscillation cycle. The left and right columns of Fig. 3.14 correspond to the values of phase ( $\varphi$ ) of  $36^\circ$  and  $144^\circ$ , respectively. At these phases, the acoustic velocity is directed into the upper side branch, and a new vortex is formed at the upstream edge of upper side branch indicated in the vorticity plot. The vortex in the lower shear layer has been fully developed and convects downstream. The top, middle and bottom rows of Fig. 3.14 correspond to the cases of  $c/t=0$ ,  $c/t=2.7$  and  $c/t=5.4$ , respectively. It should be noted that all cases presented in Fig. 3.14 correspond to the second hydrodynamic mode.

Considering the case of  $c/t=2.7$ , it can be seen in the left column of Fig. 3.14 that interaction of the shear layers with splitter plate results in the enhanced transverse oscillation of the upper shear layer at this phase. The amplitude of this oscillation is directly related to the generated acoustic power and will be described in Section 3.1.3.4. Further downstream separations at the leading edges of the splitter

plate create two additional shear layers, which interact with the trailing edges and subsequently form a vortex street in the wake of the plate. These vortices are numbered 1 and 2, respectively. It can be seen that vortex 1 is directed downward, while vortex 2 is convected downstream with less pronounced displacement in the vertical direction. This behaviour of vortex 2 is determined by the presence of larger vortex 3, which restricts it to have similar transverse amplitude.

The trajectory of the shed vortices can be indentified in the flow pattern shown in the middle-right image of Fig. 3.14, corresponding to  $\phi = 144^\circ$ . In this plot a prime symbol is added to designate each vortex from the previous phase. Both 1' and 2' vortices are travelling towards the bottom trailing edge of the cavity with relatively higher convective speeds due to acceleration of the flow on the splitter plate. These velocities can be approximated from the known positions of the vortices at the each phase of the typical oscillation cycle. It should be noticed that both shear layers from the upstream edge of the cavity and from the splitter plate correspond to the second hydrodynamic oscillation mode when two vortices are formed during a typical oscillation cycle.

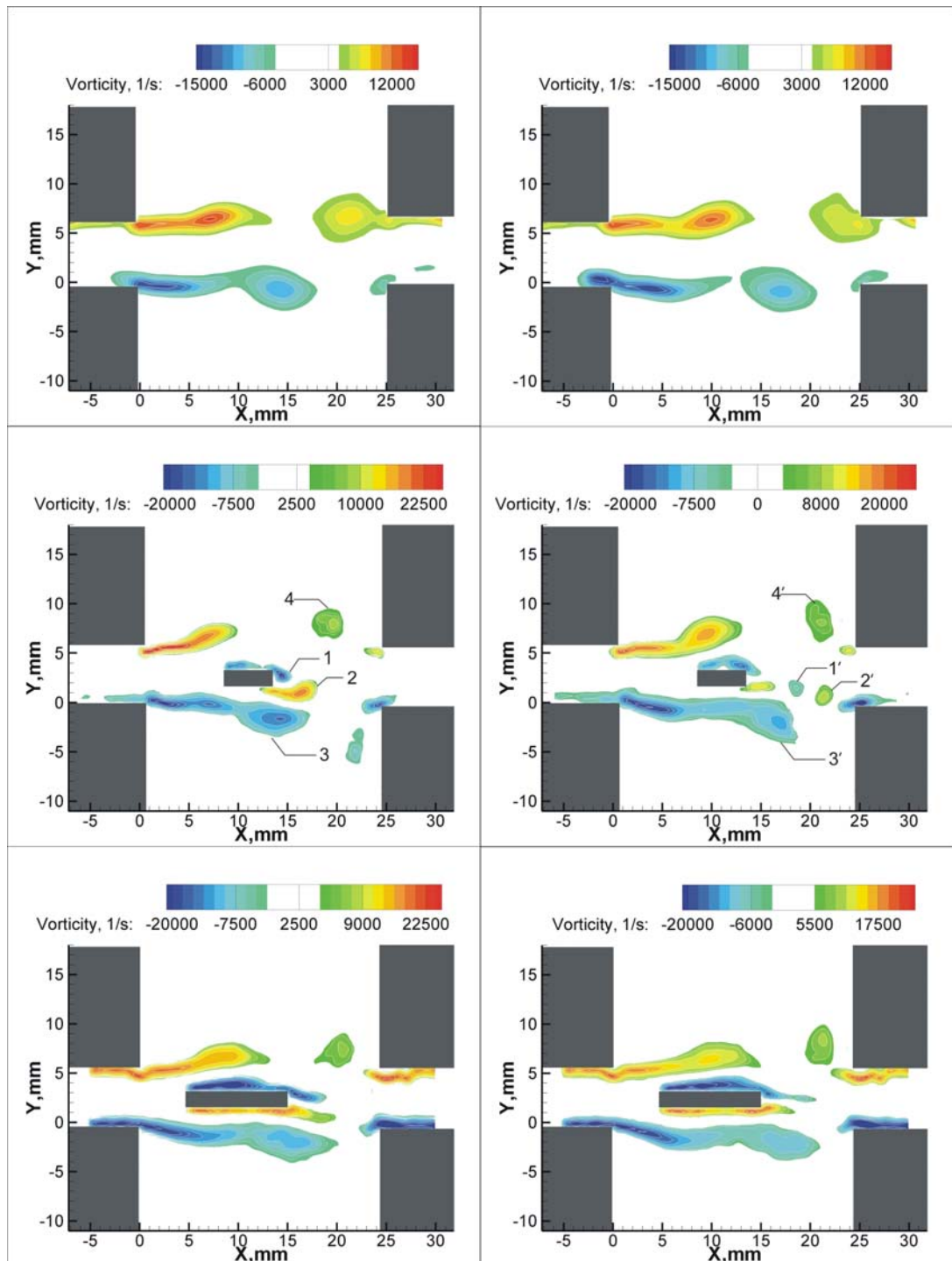


**Fig. 3.14** Pattern of phase-averaged vorticity corresponding to the  $c/t = 0, 2.7$  and  $5.4$  cases at  $\phi = 36^\circ$  and  $144^\circ$ .

The flow patterns corresponding to the case of  $c/t = 5.4$  are considered in the bottom row of Fig. 3.14. The amplitude of oscillations of the shear layers decreased

compared to the case of  $c/t = 2.7$  shown in middle row, and the dynamics of the vortices in this scenario exhibits similar qualitative behavior to the  $c/t = 0$  case. In contrast to the case of  $c/t = 2.7$  separated shear layers reattach to the surface of the long splitter plate and form a separation zone, which is described in more detail in the following Section 3.1.3.3.3. Consequently, this leads to the formation of the boundary layers, and to less pronounced oscillations in the wake of the plate. In addition the vortex street identified in the case of a short plate does not occur for the case of  $c/t = 5.4$ .

Fig. 3.15 corresponds to the values of phase ( $\varphi$ ) of  $250^\circ$  and  $324^\circ$ , respectively, and shows a similar development of all structures. It can be seen that these structures are symmetric with respect to the centerline of the duct when compared to phases shown in Fig. 3.14. This time vortices (5 and 6) shed from the splitter plate were directed towards upper downstream edge of the cavity. Shear layers at the trailing edge of the large  $c/t = 5.4$  splitter plate are now directed towards the upper side branch as well. Overall, the adjustment of the shear layer oscillations to the geometry of the cross-junction is one of the essential features of the flow-acoustic resonance phenomenon. Consequently, this non-linear mechanisms lead to the favourable phasing of flow events to occurs over a wide range of lock-in, as it was shown in Section 3.1.3.1

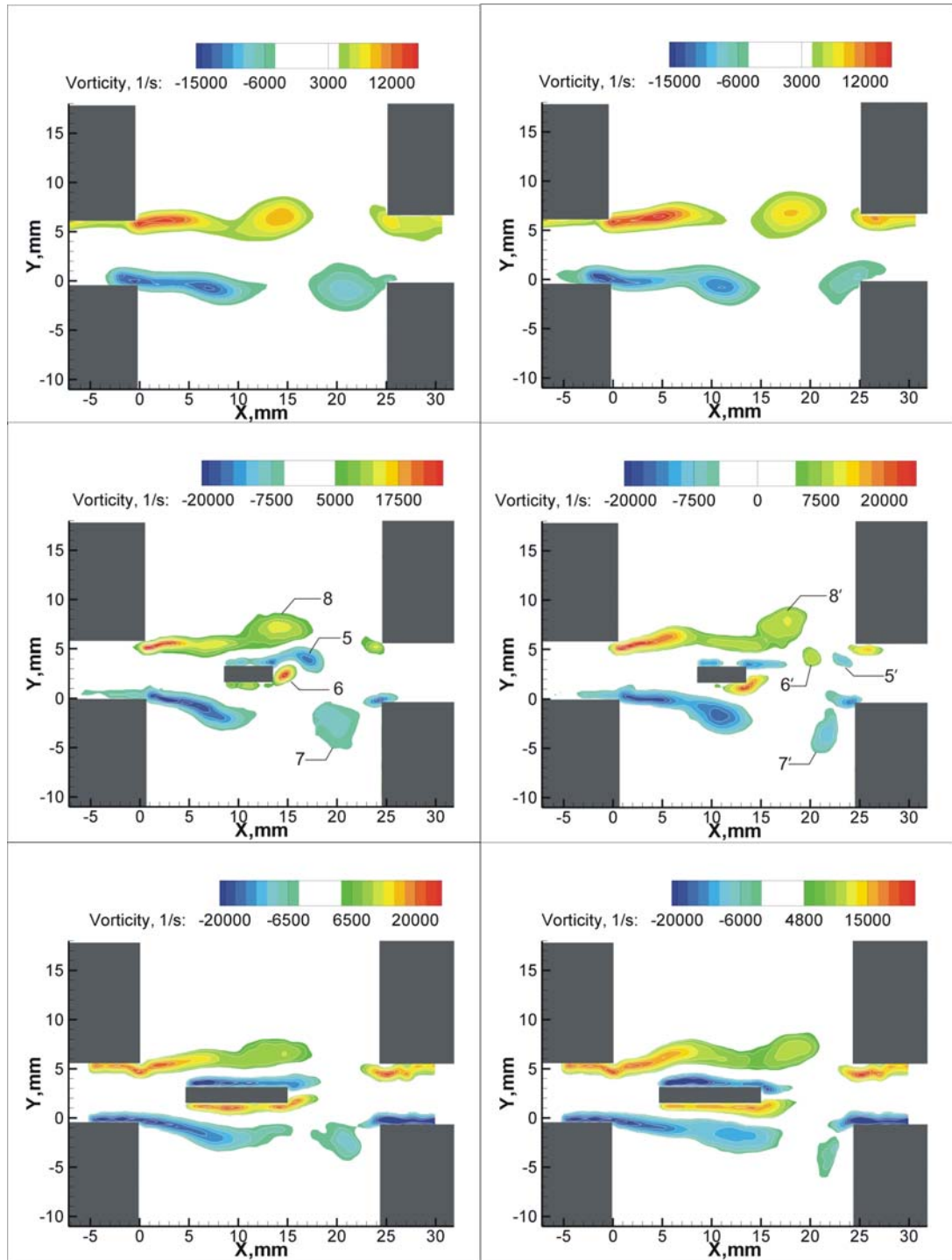


**Fig. 3.15** Pattern of phase-averaged vorticity corresponding to the  $c/t=0, 2.7$  and  $5.4$  cases  $\phi = 250^\circ$  and  $324^\circ$ .

### 3.1.3.3.3 Time-averaged flow patterns

Time-averaged velocity profiles for the cases of first and second hydrodynamic oscillation modes without plates (a, b) and second hydrodynamic mode with bluff splitter plates (c, d) are shown in Fig. 3.16. Inflow speeds, Strouhal numbers and dimensionless acoustic velocities corresponding to these cases were described in Section 3.1.3.3.1.

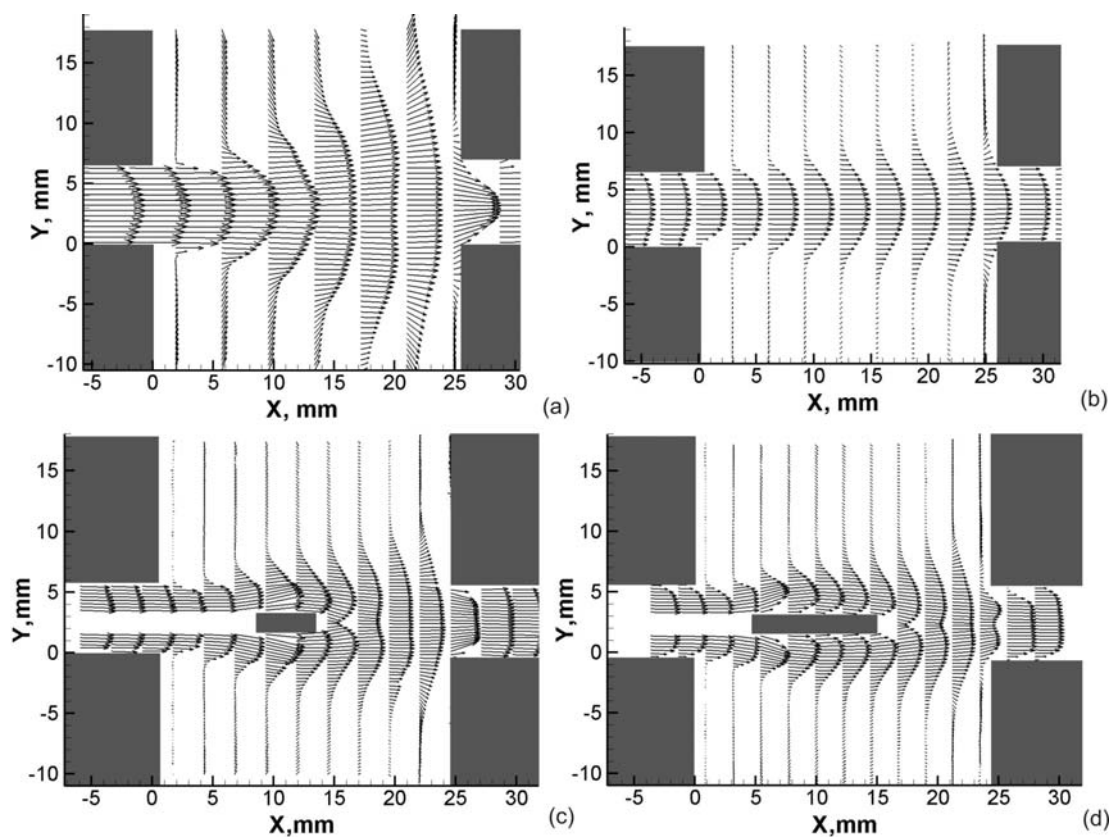


**Fig. 3.16** Time-averaged velocity profiles corresponding to the first and second hydrodynamic oscillation modes without splitter plate (a, b) and to the second mode with splitter plates (c, d)

Mixing layer presented in Fig. 3.16(a) corresponds to the first hydrodynamic oscillation mode and exhibits large entrainment compared to other cases. This entrainment results in a higher growth rate of the jet, which can be quantified from the following Fig.3.17. Less pronounced spread of the mixing layer was observed in Fig. 3.16(b), (c) and (d) due to the nature of the second hydrodynamic oscillation mode.

In the bottom row of Fig. 3.16 the bluff splitter plates are positioned in the middle of the junction. In the present investigation, the value of reattachment length ( $\overline{X}_r$ ) was determined from the time-averaged velocity field by calculating the location of the stagnation point on the surface of the plate. The velocity vector field had a physical resolution of  $175 \times 175 \mu\text{m}^2$ , which corresponded to the uncertainty of approximately  $0.2t$  in the calculated reattachment length. For the case of a short plate ( $c/t = 2.7$ ) the flow structures reattach right at its trailing edge. For long splitter plate ( $c/t = 5.4$ ) this event occurs upstream of the trailing edge at  $\overline{X}_r/t \sim 3.1$ . These experimental conclusions contradict findings of Parker and Welsh (1983) mentioned in Section 1.3.2.5. This fact can be attributed to the following causes. First, reattachment length decreases when turbulence is added to the free stream flow (Hillier and Cherry (1981)). Second,  $\overline{X}_r$  can be further decreased when a substantial amount of solid blockage is introduced (Djilali and Gartshore (1991)).

The distribution of the normalized vorticity thickness (Eqn. 1.1) across the lower side branch opening for all considered cases is shown in Fig. 3.17. The open and filled symbols correspond either to the long/short plate (Fig. 3.17a) or a first/second hydrodynamic mode (Fig. 3.17b).

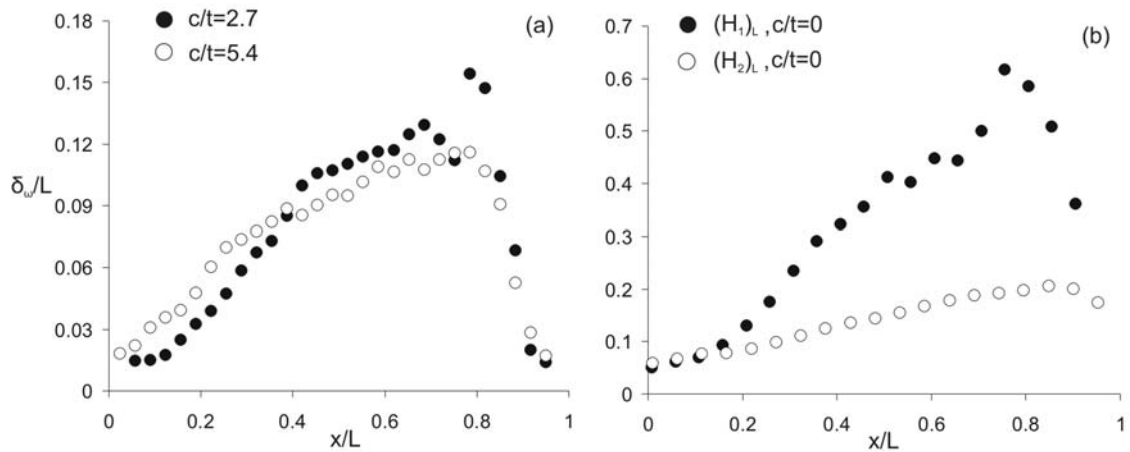


**Fig. 3.17** Distribution of vorticity thickness across the side branch opening for the case of (a) short and long splitter plate and (b) first and second hydrodynamic oscillation modes without plate

The streamwise variation of vorticity thickness shown in Fig. 3.17(a) can be classified into four stages. The first stage corresponds to an approximately linear growth of the shear layers before impingement onto the plates. This stage corresponds to the region that extends from  $x/L=0$  to  $x/L=0.33$  for the short plate ( $c/t=2.7$ ) with growth rate  $\frac{d\delta_\omega}{dx} = 0.22$ . For  $c/t=5.4$  the first stage corresponds to the segment from  $x/L=0$  to  $x/L=0.19$  with growth rate calculated to be 0.14. These results are generally within the growth rate values (0.145 – 0.22) reported by Brown and Roshko (1974) for plane mixing layers in the absence of acoustic coupling. In the second short region, the shear layer also grows in a linear fashion and approximately corresponds to the first half of the separation bubble on the splitter plate. This region covers segment from  $x/L=0.33$  to  $x/L=0.42$  for  $c/t=2.7$  having growth rate  $\frac{d\delta_\omega}{dx}$  of 0.37. For  $c/t=5.4$  this stage corresponds to the distance between  $x/L=0.19$  and  $x/L=0.27$  with growth rate of 0.33. The increased growth rates in these regions are due to interaction of the turbulent shear layers with the bluff body. In the third stage up to  $x=0.6L$  corresponding to the trailing edge of the plates, growth rates of the shear

layers decrease sharply with values of 0.12 and 0.115 respectively. Finally, the region beyond the splitter plates is characterized by the sharp increase of velocity gradients and interaction between shear layers, which results in formation of small vortices and leads to general decrease in the vorticity thickness values.

The growth rate of the vorticity thickness for  $(H_1)_L$  across the first segment of the cavity opening ( $x/L = 0.15$  to  $x/L = 0.5$ ) shown in Fig 3.17 (b) is associated with  $\frac{d\delta_\omega}{dx}$  as large as 0.9. Although, the rate of growth does decrease after  $x/L = 0.5$ , its value always exceeds 0.57. The wavelength and scale of the vortices in the shear layer are expected to increase as the vorticity thickness increases Monkewitz and Huerre (1982). Therefore, the plot of Fig. 11 indicates that small-scale vortices were forming in the vicinity of the upstream corner of the side branch, and that they subsequently transformed into large-scale concentrations at locations well downstream from the flow separation point. It should be noted that the rate of growth of the vorticity thickness substantially increased at the downstream distance of  $x/L \approx 0.15$ . Instantaneous flow patterns shown in Fig. 3.12 as well as phase-averaged flow patterns reported by Oshkai and Yan (2008) indicate that vortex roll-up occurred at this location. High value of the growth rate observed in the present experiments is attributed to the presence of flow-acoustic coupling, which promotes formation of large-scale vortical structures due to large acoustic velocity amplitudes. Fig. 3.17(b) also shows the distribution of the normalized vorticity thickness across the lower side branch opening for the case of the second shear layer oscillation mode. The vorticity thickness distribution was qualitatively similar to that observed in the case of the first hydrodynamic mode, i.e. it increased with the downstream distance. The growth rate

of the shear layers across the entire cavity was approximately equal to 0.16, which is substantially lower compared to the case of the first hydrodynamic mode. It is suggested that this decrease is due to formation of two vortices per acoustic oscillation cycle in each shear layer, as opposed to one vortex per cycle that forms during the first hydrodynamic oscillation mode.

As it was indicated in Section 3.1.3 presence of the plates inhibits the first hydrodynamic oscillation mode and substantially decreases growth rates of the shear layers. Moreover,  $\frac{d\delta_\omega}{dx}$  was found to be substantially less in the case of a long splitter plate ( $c/t=5.4$ ) compared to the case of  $c/t=2.7$ .

Distribution of the time-averaged vorticity is shown in Fig. 3.18. Peak values of  $\langle\omega_z\rangle$  correspond to the locations of flow separation from the upstream edges of the side branches. High values were also exhibited at the downstream corners, where secondary separation takes place. Figs. 3.18(c) and (d) show additional shear layers that were formed at the trailing edge of the bluff splitter plates.

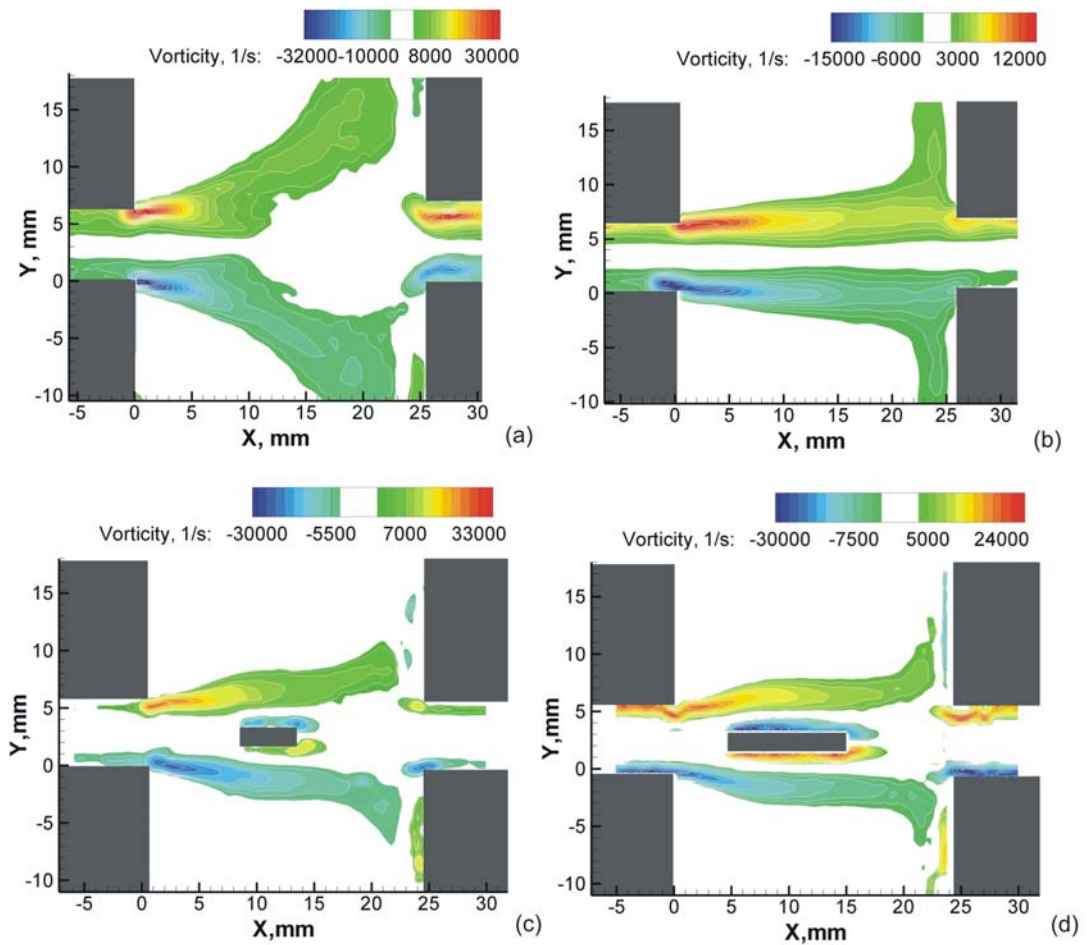


**Fig. 3.18** Patterns of time-averaged vorticity  $\langle \omega_z \rangle$  distribution corresponding to the first and second hydrodynamic oscillation modes without splitter plate (a, b) and to the second mode with splitter plates (c, d)

The values of non-dimensional velocity fluctuations and their correlations for all four cases are presented in terms of patterns of  $\langle u_{\text{rms}} \rangle / U_0$ ,  $\langle v_{\text{rms}} \rangle / U_0$ , and  $\langle u'v' \rangle / U_0^2$ , in Figs. 3.19, 3.20 and 3.21 respectively. Peak values of  $\langle u_{\text{rms}} \rangle / U_0$  occurred immediately downstream of the secondary separation points in the case without splitter plate. In the vicinity of the upstream corners ( $x \sim 7\text{mm}$ ) of the side branches, substantially large  $\langle u_{\text{rms}} \rangle / U_0$  values existed over an extensive domain, which suggests that roll-up and consequent growth of the vortices took place in that region. In contrast, in the case of the splitter plates shown in Figs 3.19(c) and (d) maximum

values of  $\langle u_{\text{rms}} \rangle / U_0$  occurred in the vicinity of the trailing edge. These regions correspond to the interaction of the shear layers downstream of the splitter plates. The minimum values of  $\langle u_{\text{rms}} \rangle / U_0 = 0.12$  were observed for the case of a long splitter plate.

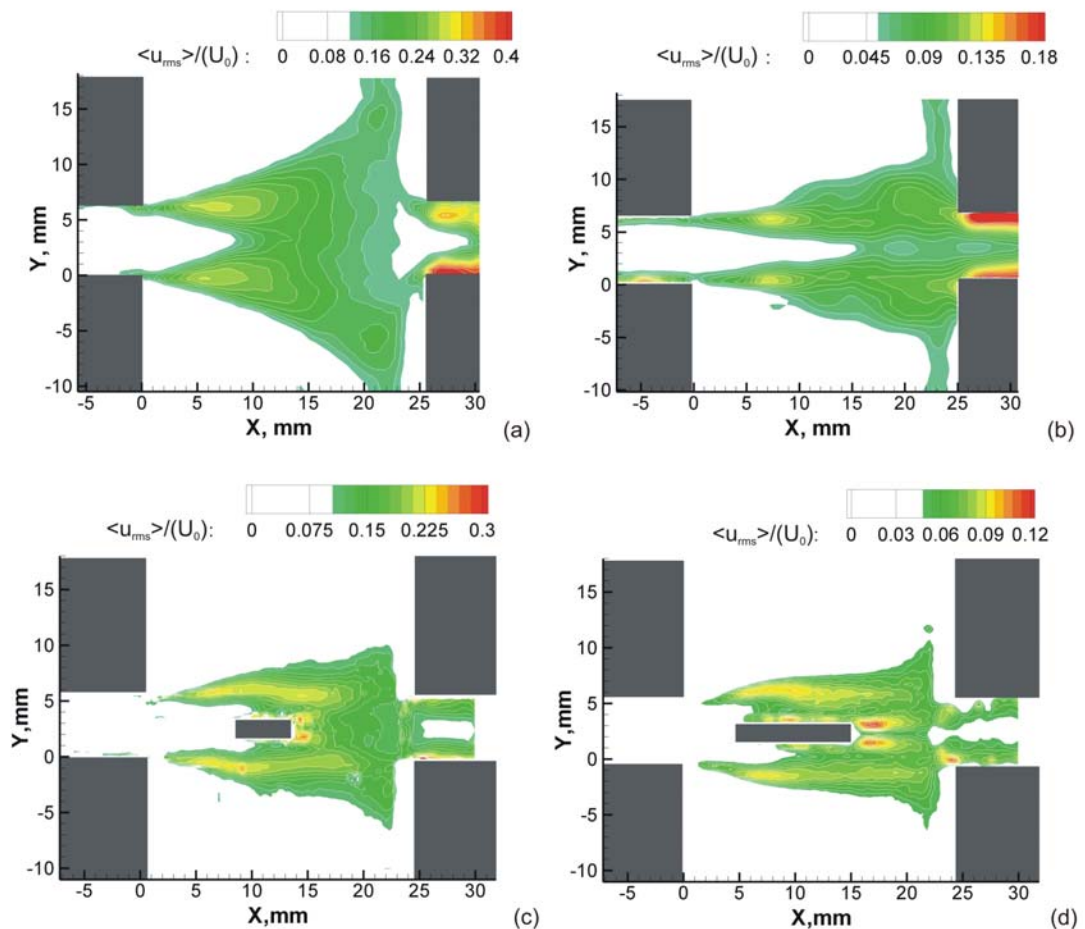


**Fig. 3.19** Patterns of time-averaged  $\langle u_{\text{rms}} \rangle / U_0$  distribution corresponding to the first and second hydrodynamic oscillation modes without splitter plate (a, b) and to the second mode with splitter plates (c, d)

The corresponding  $\langle v_{\text{rms}} \rangle / U_0$  plots that are shown in Fig. 3.20(a) exhibited peak values of 0.3 at  $x = 17$  mm and  $y = 10$  and  $y = -6$  mm for the upper and lower side branches respectively. The large excursions of the shear layers into the side branches are evident. This pattern was characteristic to the first hydrodynamic mode of shear layer oscillations. High values of  $\langle v_{\text{rms}} \rangle / U_0$  (up to 0.16) occurred in Fig.

3.20(b) in the downstream region of the cross-junction, which indicates that this region of flow involved significant movement of large-scale clusters of vorticity. The single region of the  $\langle v_{rms} \rangle / U_0$  in that case suggests the presence of single acoustic noise structure close to the downstream edge of the cavity.

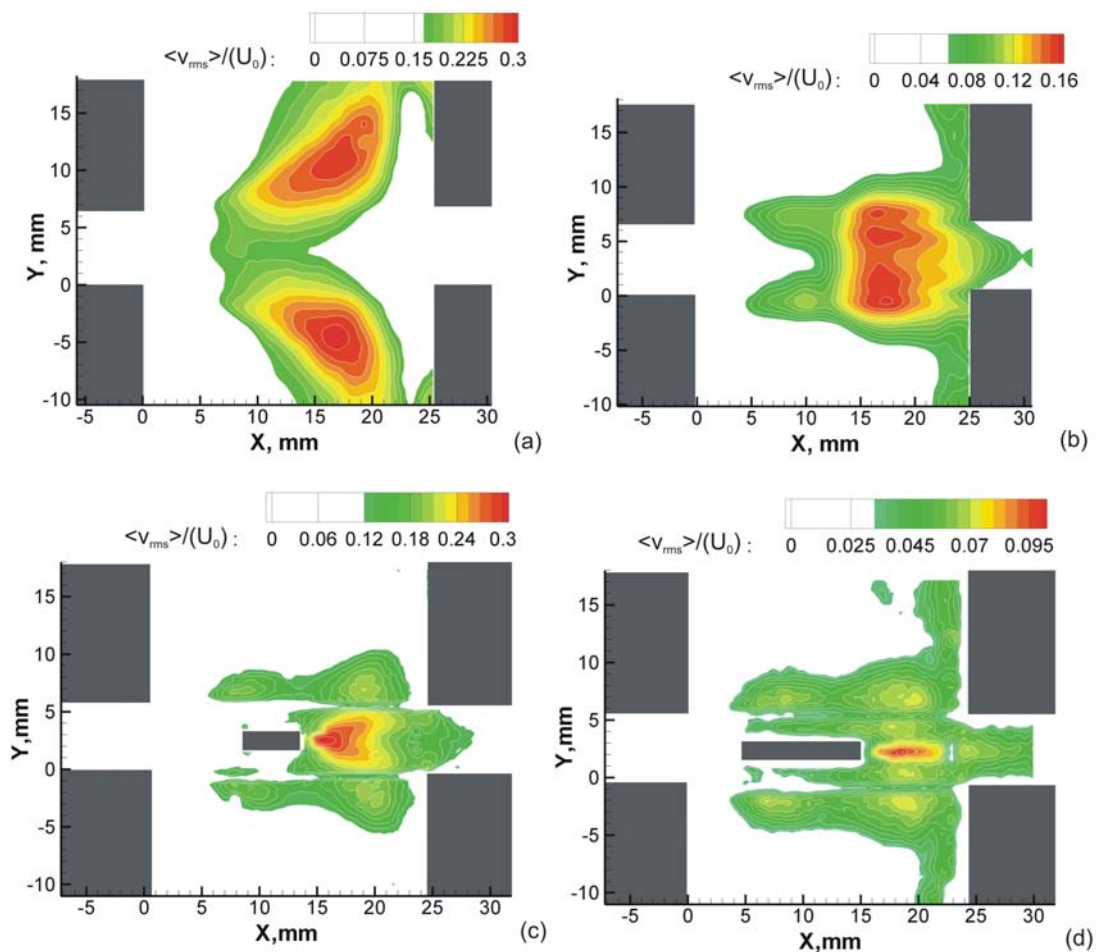


**Fig. 3.20** Patterns of time-averaged  $\langle v_{rms} \rangle / U_0$  distribution corresponding to the first and second hydrodynamic oscillation modes without splitter plate (a, b) and to the second mode with splitter plates (c, d)

Figures 3.20(c) and (d) show the distribution of the  $\langle v_{rms} \rangle / U_0$  component for the case of the short and the long splitter plates ( $c/t = 2.7$  and  $5.4$ ), respectively. The elevated contours in Fig 3.20(c), with peak values of  $\langle v_{rms} \rangle / U_0 = 0.18$  occurred approximately at  $x = 8$  mm and  $x = 20$  mm corresponding to the regions where cavity

shear layers interacted with leading and trailing edge shear layers. Significant values of  $\langle v_{\text{rms}} \rangle / U_0 = 0.3$  concentrated in the area downstream the short splitter plate. For the case of a long plate ( $c/t = 2.7$ ) shown in Fig. 3.20(d) elevated contours existed at similar locations, i.e. at  $x = 8$  and  $20$  mm. In contrast to the case shown in Fig. 3.20(c), the elevated contour downstream the long plate in the middle of the junction was substantially smaller in size and magnitude, exhibited peak values of  $\langle v_{\text{rms}} \rangle / U_0 < 0.1$ .

The patterns of velocity correlation  $\langle u'v' \rangle / U_0^2$  that corresponds to the dominant Reynolds shear stress component are shown in Fig. 3.21. Generally speaking, substantial values of  $\langle u'v' \rangle / U_0^2$  of the opposite sign were present along the upper and the lower shear layers for all cases. Large excursions of the  $\langle u'v' \rangle / U_0^2$  in Fig. 3.21(a) with a peak value of  $0.05$  correspond to the first hydrodynamic oscillation mode. The velocity correlation shown in Fig. 3.21(b) exhibited two peaks in the contour plots corresponding to each shear layer (at  $x = 9$  and  $x = 17$  mm). These values, however, are of low magnitude compared to the first hydrodynamic mode case.

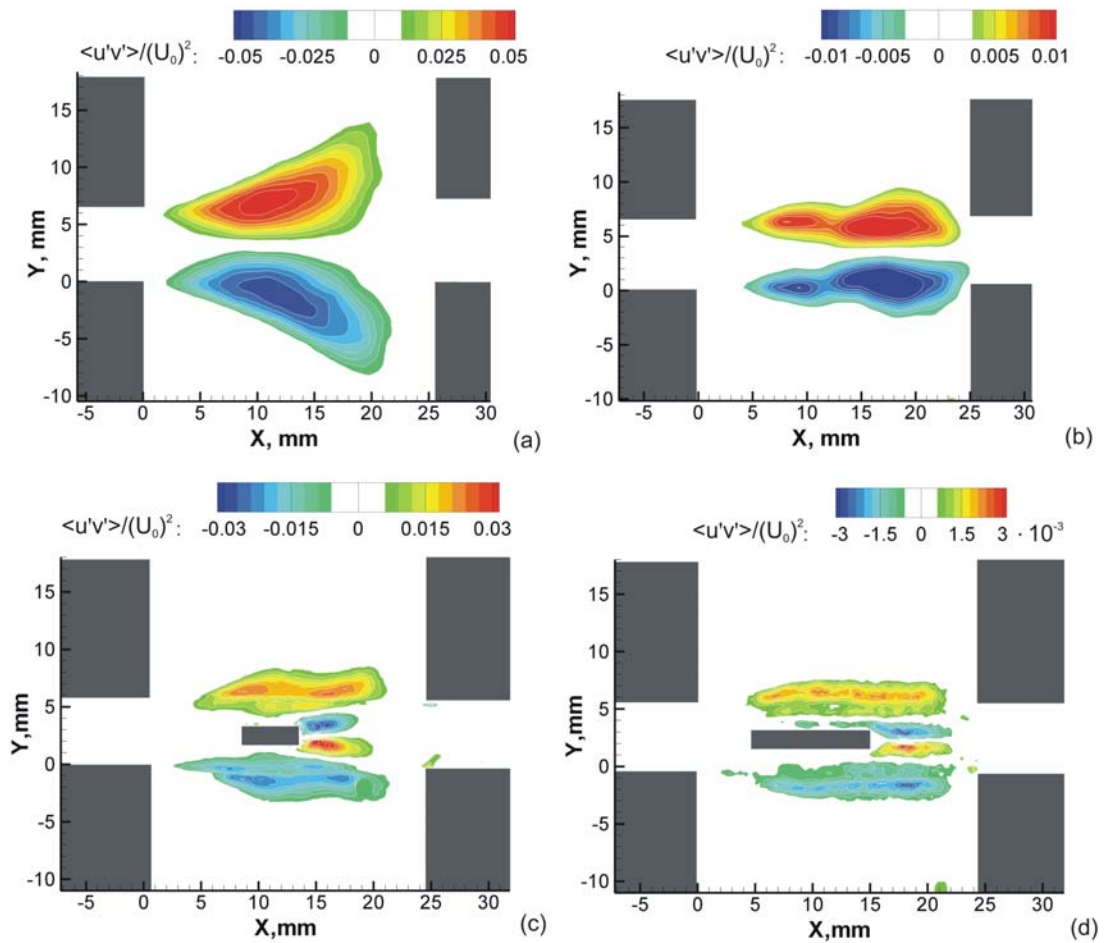


**Fig. 3.21** Patterns of time-averaged  $\langle u'v' \rangle / U_0^2$  distribution corresponding to the first and second hydrodynamic oscillation modes without splitter plate (a, b) and to the second mode with splitter plates (c, d)

Two additional layers of  $\langle u'v' \rangle / U_0^2$  can be seen in Figs. 2.21(a) and (b). These layers have opposite signs and correspond to the formation of the shear layers at the trailing edges of plates. Insignificant peak values of Reynolds shear stress of  $3 \cdot 10^{-3}$  were observed in Fig. 3.21(b) for the long splitter plate ( $c/t=5.4$ ).

### 3.1.3.4 Acoustic power

#### 3.1.3.4.1 Acoustic power calculation

The instantaneous acoustic power  $P_w$  generated by vorticity  $\underline{\omega}$ , within a volume  $V$  can be obtained from:

$$P_w = -\iiint_V \rho_0 (\underline{\omega} \times \underline{V}) \cdot \underline{u}_{ac} dV, \quad (3.5)$$

where  $\rho_0$  is the fluid density,  $\underline{V}$  is the fluid velocity, and  $\underline{u}_{ac}$  is the acoustic particle velocity.

As it was stated the theoretical framework for this approach to acoustic power calculation has been developed by Howe (1975). The hydrodynamic contribution to the acoustic power integral,  $(\underline{\omega} \times \underline{V})$ , was calculated based on the global phase-averaged flow measurements. The amplitudes of the horizontal and vertical components of the acoustic particle velocity  $\underline{u}_{ac}$  were determined using numerical model described in Section 3.1.1.

The incompressible vorticity-bearing (hydrodynamic) velocity field was calculated by subtracting the acoustic velocity from the total phase-averaged flow velocity that was measured experimentally using the DPIV technique, as described in the previous section. More specifically the triple product is evaluated as follows:

$$\underline{\omega} \times \underline{v} = \begin{vmatrix} i & j & k \\ 0 & 0 & \omega_z \\ u - u_{acx} & v - u_{acy} & 0 \end{vmatrix} = (u - u_{ax})\omega_z \underline{j} - (v - u_{ay})\omega_z \underline{i}, \quad (3.6)$$

which leads to

$$\begin{aligned} (\underline{\omega} \times \underline{v}) \cdot \underline{u}_{ac} &= \left\{ (u - u_{ax})\omega_z \underline{j} - (v - u_{ay})\omega_z \underline{i} \right\} \cdot \{u_{ax} \underline{i} + u_{ay} \underline{j}\} = \\ &= \left( (u - u_{ax})u_{ay} - (v - u_{ay})u_{ax} \right) \omega_z \end{aligned} \quad (3.7)$$

substituting expression (3.7) into Eqn. (3.5) yields

$$P_w = -\rho_0 \iiint_V \left( (u - u_{ax})u_{ay} - (v - u_{ay})u_{ax} \right) \omega_z dV \quad (3.8)$$

### 3.1.3.4.2 Acoustic power at one period of acoustic oscillation

Figure 3.22 shows acoustic power generated during one period of acoustic oscillation cycle by both top and bottom shear layers for of  $c/t=0$ ,  $c/t=2.7$  and  $c/t=5.4$  respectively. These results correspond to the second hydrodynamic mode with  $Sr=0.72$  and  $Sr=0.78$  for the cases without and with splitter plates respectively.

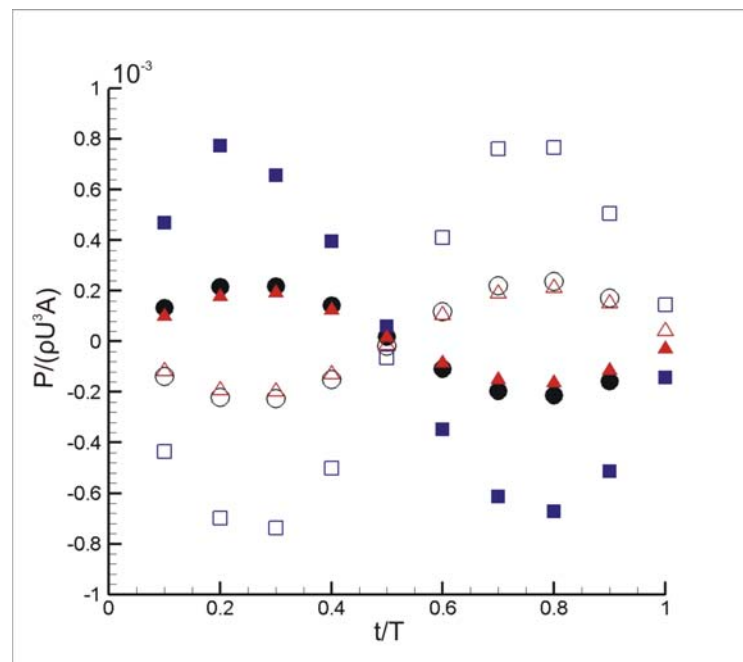


**Fig. 3.22** Acoustic power generated by the top (filled) and bottom (open symbols) shear layers during one period of acoustic oscillation:  $c/t=0$  (●),  $c/t=2.7$  (■),  $c/t=5.4$  (▲).

The source power is initially positive for the top side branch and negative for the bottom one. This is due to the positive acoustic velocity flux in the triple product in the first half period and the opposite signs of the vorticity shed at each corner. A slight difference in amplitude is caused by the fact that both the hydrodynamic and the

acoustic velocity fields in the top side branch contribute to the shedding of positive vorticity. For the bottom side branch these fields are opposite in direction. At the second half period the total circulation of the vortex structures have increased and the magnitude of the source power increases. Therefore, the net power production obtained after time-averaging the acoustic power over an acoustic period is positive (see section 3.1.2.6).

It is also observed in Fig 3.22 that maximum acoustic power is generated in the case of  $c/t = 2.7$ . The case without splitter shows comparable values of generated power with long splitter plate scenario. The acoustic response of the resonator (indirectly) strengthens the conclusion that the system experiences substantially different hydrodynamic behaviour with a short plate, which was discussed in Sections 3.1.3.3.1 and 3.1.3.3.2

#### *3.1.3.4.3 Time-averaged distribution of the acoustic source*

Figure.3.23 shows spatial distribution of the integrand of Eqn. (3.8) corresponding to the first and second hydrodynamic oscillation modes for the case without splitter plates ( $c/t = 0$ ). Substantial interaction between the shear layers results in formation of a single acoustic power source region close to the centerline of the main duct, as shown in Fig. 3.23(a). The source is accompanied by two sinks that correspond to the regions in the shear layers where vortex development takes place. It should be noted that the source region extends across almost the entire opening of the coaxial side branch resonator. The peak values of the generated acoustic power (4000 N/s) correspond to large-scale vortices, which extend far into the side branches during the transverse oscillations of the separated shear layers.

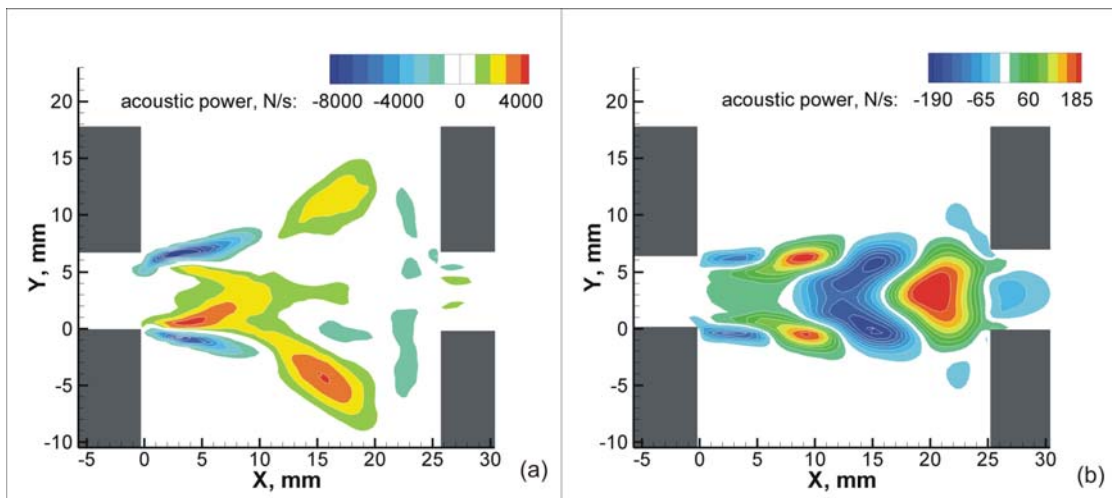


**Fig. 3.23** Patterns of time-averaged distribution of the acoustic source corresponding to the first (a) and second (b) hydrodynamic oscillation modes:  $c/t = 0$ .

Spatial distribution of the acoustic source corresponding to the second hydrodynamic mode is shown in Fig. 3.23(b). Immediately after the separation, the amplitude of the transverse oscillations of the shear layers is limited, and two discrete source-sink pairs exist in the vicinity of the upstream corner of the junction. The two sink regions with peak amplitudes of 190 N/s are located at  $x=4$  mm. Farther downstream, the transverse shear layer undulations increase in amplitude, and a large single sink of acoustic power is present. This sink region exhibits high levels of negative acoustic power due to the increasing circulation of the large-scale vortices. Prior to impingement on the downstream side branch corner, the two interacting shear layers produce a single large-scale source region. Flow separation from the downstream corners of the side branches correlates with the acoustic flux into the main duct and results in negative contribution to the acoustic power budget.

Time-averaged structure of the acoustic source corresponding to the splitter plates of  $c/t = 2.7$  and  $c/t = 5.4$  is exhibited in Fig. 3.24. For the case of a short plate

shown in Fig. 3.24(a), two dominant source-sink regions extend from the leading edges of the side branches up to  $x=15$  mm. Flow separation (without reattachment) occurred in this region of the splitter plate. Additional source-sink pairs formed immediately downstream the splitter plate and attributed to both shear layers that were present in the junction. Prior to impingement onto the downstream side branch corner, all shear layers that were present in the junction interacted to produce a single large-scale source region. This region exhibited a complex structure and lower values of acoustic power compared to the two sources in the vicinity of the plate.

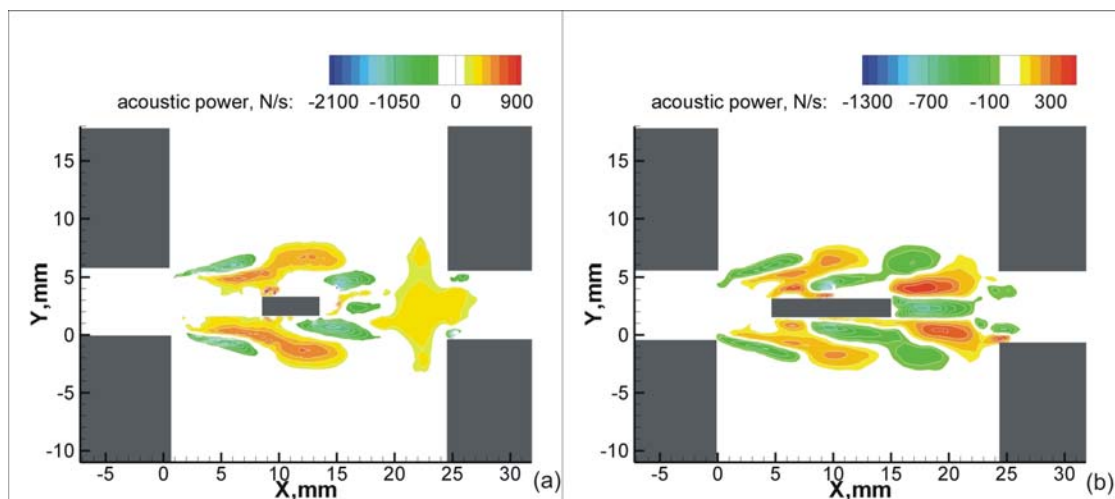


**Fig. 3.24** Patterns of time-averaged distribution of the acoustic source:  $c/t = 2.7$  (a) and  $c/t = 5.4$  (b)

In the case of the long splitter plate shown in Fig. 3.24(b), two discrete source-sink pairs exist in the vicinity of the upstream corner, which is similar to the previous scenario. While the sinks are similar in size and magnitude to those shown in Fig. 3.24(a), the source regions in the case of the long splitter plate ( $c/t = 5.4$ ) were limited in the longitudinal direction and exhibited lower values of generated power. Further downstream, two sink regions were observed in the vicinity of the splitter plate due to formation of the boundary layer. These regions are connected to the sinks produced by upstream shear layers. Downstream of the plate, two source regions with peak

amplitude of 350 N/s were located at  $x=20$  mm. A slender sink region exists between these sources in the wake of the splitter plate.

In summary, with the presence of the long plate ( $c/t=5.4$ ) in the cross-junction the maximum values of acoustic power substantially decreased due to interaction of the acoustic field with the vortices formed at the splitter plate. As a result, reduced amount of acoustic energy is available for assisting in formation of large-scale vortical structures in the side branch shear layers. This phenomenon is utilized in large-scale industrial heat exchangers where perforated screens and splitter plates are used for sound dissipation (Howe, 1986).

### *3.1.3.5 Visco-thermal damping and net acoustic power*

Previously, Dequand (2003) evaluated visco-thermal damping and acoustic source strength associated with a cavity resonator using a vortex model of Nelson et al. (1983). This model assumes that a shear layer is composed of a train of point vortices that are convected across the cavity opening at a constant velocity. The acoustical model employed by Dequand (2003) involved the assumption of plane harmonic wave propagation in the side branches. The present study utilized the theoretical framework outlined by Dequand (2003) and employed a two-dimensional acoustic velocity field, which was calculated numerically as it is described in Section 3.1.1.

The visco-thermal acoustic losses that occur over a period of acoustic oscillation are defined by Dequand (2003):

$$\overline{P_{vth}} = \frac{1}{T} \int_0^T R \overline{|U_{ac}|_s}^2 dt, \quad (3.9)$$

where  $T$  is the acoustic oscillation period,  $R$  is the damping coefficient, and  $\overline{|U_{ac}|}_S$  is the mean magnitude of the acoustic particle velocity in the source region  $S$ . In turn, the damping coefficient is defined as follows Kinsler et al. (2000):

$$R = \frac{\omega_0 M_{ea}}{Q}, \quad (3.10)$$

where  $\omega_0$  is the resonant angular frequency, and  $Q$  is the quality factor of the system, which is defined in Fig. 3.9. The effective acoustical mass  $M_{ea}$  can be determined from the expression of the kinetic energy of the system Dequand (2003):

$$E_k = \frac{1}{2} M_{ea} \overline{|U_{ac}|}_S^2 = \frac{1}{2} \rho_0 \iint_D |U_{ac}|^2 dx dy, \quad (3.11)$$

where  $U_{ac}$  is the acoustic velocity defined by Eqn. (3.3) and  $D$  is the experimental domain that includes the side branches and the main duct.

Under the assumption of thin visco-thermal boundary layers, compared to the side branch cross-section, the  $Q$ -factor of a coaxial side branch resonator is related to the damping coefficient  $\alpha$  Dequand (2003):

$$Q = \frac{\pi}{4\alpha W}. \quad (3.12)$$

Here,  $\alpha$  can be calculated using the following relationship:

$$\alpha = \frac{L_p}{2A} \sqrt{\pi \nu f} \left( 1 + \frac{\gamma - 1}{\sqrt{\text{Pr}}} \right), \quad (3.13)$$

where  $A$  and  $L_p$  are the cross-sectional area and the perimeter of the side branch, respectively, and  $\nu$ ,  $\gamma$ , and  $\text{Pr}$  are the kinematic viscosity, the specific heat ratio, and the Prandtl number, respectively.

The net acoustic power generated during a typical oscillation period can be calculated by integrating the values of the time-averaged acoustic power that are

shown in Figs. 3.23 and 3.24 over the source region. The values of the time-averaged visco-thermal losses and the net acoustic power calculated for the two hydrodynamic oscillation modes ( $(H_1)_L$  and  $(H_2)_L$ ) are summarized in Table 3.3:

	$c/t=2.7$ $(H_2)_L$	$c/t=5.4$ $(H_2)_L$	$c/t=0$ $(H_1)_L$	$c/t=0$ $(H_2)_L$
$\overline{P}_{vth}, W/m$	<b>0.0002</b>	<b><math>6*10^{-5}</math></b>	<b>0.0014</b>	<b><math>4*10^{-5}</math></b>
$\overline{P}_{ac}, W/m$	<b>0.007</b>	<b>0.0012</b>	<b>0.16</b>	<b>0.0013</b>

**Table 3.3** Mean values of net acoustic power and visco-thermal losses

The values of the net acoustic power were positive for all resonant modes, which is consistent with the concept of flow tone generation as well as with the earlier results of Kriesels et al. (1995). Previous studies indicate that the net generated acoustic power is negative in the absence of flow-acoustic resonance (i.e. for the values of flow velocity that do not correspond to dominant pressure peaks shown in Fig. 3.6). The net generated acoustic power was two orders of magnitude higher in the case of the first hydrodynamic oscillation mode ( $(H_1)_L$ ) as compared to the second hydrodynamic mode case ( $(H_2)_L$ ). It is suggested that the reduction in the generated acoustic power levels that was observed at the second hydrodynamic mode was due to the decrease in the amplitude of the transverse shear layer oscillations that is evident in the distributions of vorticity contours. In the case of a short plate ( $c/t=2.7$ ) the net generated acoustic power is still much lower compared to the first hydrodynamic mode without splitter plate, while a substantial increase is observed when compared to the second hydrodynamic mode. This fact is attributed to the dynamics of the shear layers shed from the leading edge of the plate and their subsequent interaction with

the large scale vortices, which result in increased oscillations of the shear layers and corresponding gain added to the acoustic power budget.

In contrast to the findings of Kriesels et al. (1995) the calculated values of the time-averaged visco-thermal damping were very small compared to the net acoustic power for all considered cases. According to Kriesels et al. (1995), at moderate pulsation amplitudes ( $p/\rho_0 c_0 U < 0.2$ , which is the case in the present experiments), acoustic power is approximately balanced by visco-thermal losses. The losses due to radiation of non-resonating harmonics into the main duct become relevant at higher pulsation levels and dominant only when  $p/\rho_0 c_0 U > 0.5$ . Therefore, a comparison provided by Table 3.3 confirms the hypothesis that there is a substantial amount of the radiated acoustic energy in the system.

## 3.2 TURBULENT FLOW OVER THE AIR CLAMP IN PROXIMITY TO A FLEXIBLE AND SOLID WALLS

### 3.2.1 Paper profile

In the absence of the flow, the paper sheet was positioned horizontally at a distance  $H = 6$  mm above the surface of the air clamp (measured upstream of the BFS). The time-averaged paper sheet profile corresponding to  $\Delta p = 25.5$  kPa ( $U_0 = 120$  m/s) and the sheet width of 88.9 mm is shown in Fig. 3.25. Interaction between the air flow and the flexible paper sheet resulted in the paper sheet profile that can be approximated by linear segments with slopes  $\alpha_1 = 1.5^\circ$  ( $-4.5 < x/h < 4.5$ ),  $\alpha_2 = 3.1^\circ$  ( $4.5 < x/h < 22$  mm), and  $\alpha_3 = 2.4^\circ$  ( $22 < x/h < 48$ ). The segments corresponding to  $\alpha_1$  and  $\alpha_2$  are indicated in Fig. 3.25, while the segment corresponding to  $\alpha_3$  was located outside of the FOV1. The resulting geometry of the flow field between the surface of the air clamp and the paper sheet corresponded to a diverging channel configuration.

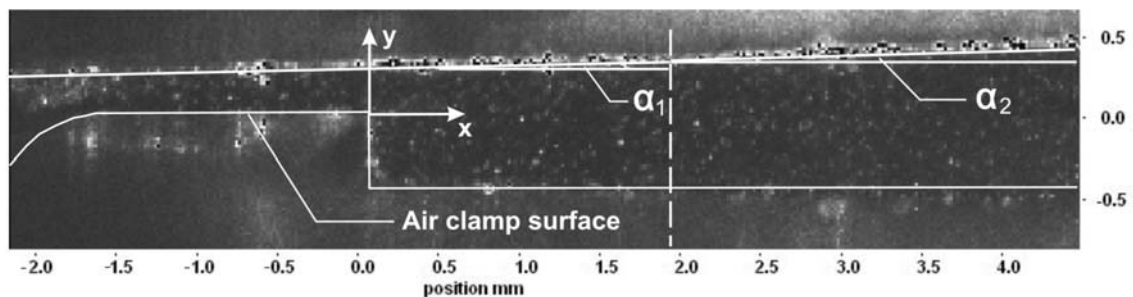


**Fig. 3.25** Time-averaged profile of the paper sheet (FOV1,  $\Delta p = 25.5$  kPa,  $U_0 = 120$  m/s,  $W = 88.9$  mm)

Inclination angles of the paper sheet corresponding to three values of the inflow velocity  $U_0$  are provided in Table 3.4. The inclination angles were measured with an error of less than  $0.2^\circ$ .

	$U_0 = 100$ m/s		$U_0 = 120$ m/s		$U_0 = 150$ m/s	
	$\alpha$	$x/h$	$\alpha$	$x/h$	$\alpha$	$x/h$
$\alpha_1$	0.8°	-4.5 to <b>1</b>	1.5°	-4.5 to <b>4.5</b>	1.9°	-4.5 to <b>6.5</b>
$\alpha_2$	2°	<b>1</b> to 48	3.1°	<b>4.5</b> to <b>22</b>	3.5°	<b>6.5</b> to <b>11</b>
$\alpha_3$	-	-	2.4°	<b>22</b> to 48	2.6°	<b>11</b> to 48
$H_0/h$	0.8		0.6		0.4	
$\overline{X}_r/h$	4.8		5.3		6.2	
$Re_h$	3000		3600		4500	

**Table 3.4** Summary of inclination angles of the paper sheet and shear layer reattachment lengths for case 2.

Table 3.4 also shows the non-dimensional distance of the paper sheet from the surface of the air clamp at  $x = 0$  ( $H_0/h$ ) as well as the non-dimensional reattachment length of the shear layer ( $L/h$ ), which was determined using the quantitative flow patterns described in Section 3.2.2. As the inflow velocity  $U_0$  increased, the paper sheet was pulled closer to the surface of the air clamp, which corresponded to the decrease of the  $H_0/h$  value. The inclination angles  $\alpha_1$  and  $\alpha_2$  increased with the increasing  $U_0$ . The observed increase in the reattachment length  $L/h$  with the increasing angle of the diverging channel configuration is in agreement with earlier investigations of Driver and Seegmiller (1985).

The downstream distance from the BFS location ( $x = 0$ ) to the point where the inclination angle of the paper sheet changes from  $\alpha_1$  to  $\alpha_2$  increases with the increasing inflow velocity. For the case of  $U_0 = 100$  m/s, this point ( $x/h = 1$ ) corresponds to the location of the interface between two counter-rotating flow recirculation cells that exist downstream of the BFS. This flow structure, which is described in detail in Section 3.2.2 (Fig. 3.28), results in periodic upward injection of fluid into the core of the jet. It is suggested that the change in the inclination angle of

the paper sheet is related to the net flux of vertical momentum that exists in the vicinity of  $x/h = 1$ .

For the cases of  $U_0 = 120$  m/s and  $U_0 = 150$  m/s, the location of the change in the inclination angle of the paper sheet from  $\alpha_1$  to  $\alpha_2$  corresponds to the downstream location of the shear layer reattachment to the surface of the air clamp. The local change in the paper profile is attributed to the change in static pressure, which is characteristic to flow reattachment. An additional change in the inclination angle of the paper sheet from  $\alpha_2$  to  $\alpha_3$  was observed for the cases of  $U_0 = 120$  m/s and  $U_0 = 150$  m/s at  $x/h = 22$  and  $x/h = 11$ , respectively. This secondary change in the paper profile is attributed to the flow separation and subsequent reattachment to the inclined paper sheet (not shown herein). It should be noted that reattachment occurs farther downstream for the case of the lower inflow velocity ( $U_0 = 120$  m/s).

Figure 3.26 shows a typical spectrum of the paper sheet vibration in the cross-flow (y-axis) direction. The plot of Fig. 3.26 was obtained by averaging the vibration spectra corresponding to 1000 streamwise locations that were uniformly distributed along the field of view of the camera ( $0 < x/h < 20$ ).

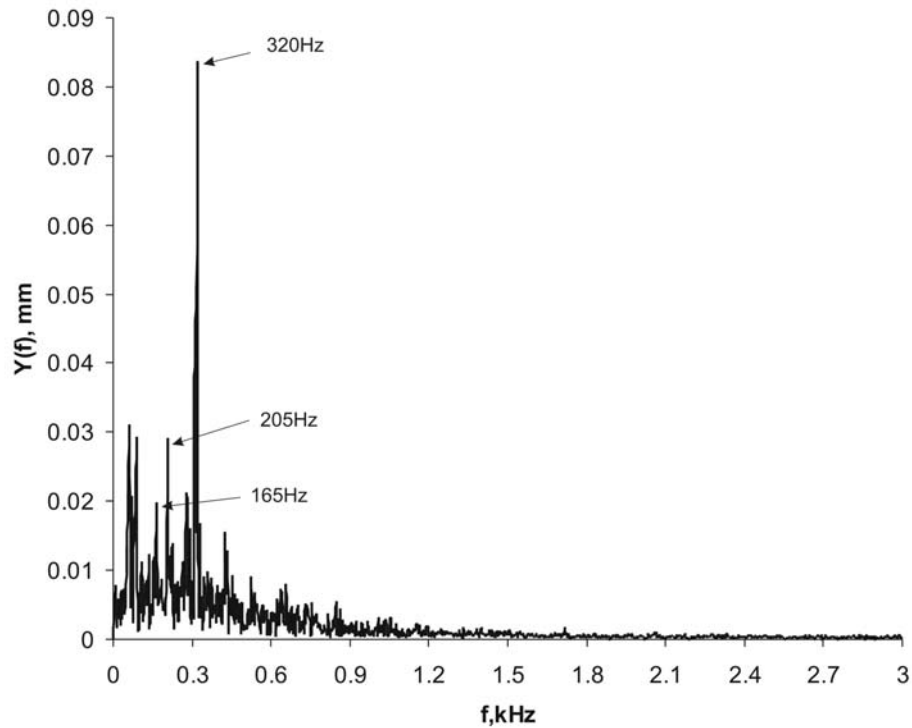


**Fig. 3.26** Spectrum of the paper sheet vibration ( $\Delta p = 25.5$  kPa,  $U_0 = 120$  m/s,  $W = 158.8$  mm)

The spectral peaks that are observed in Fig. 3.26 correspond to the eigenfrequencies (modes) of an oscillating membrane, which can be calculated using the following expression:

$$f_{mn} = \frac{1}{2} \sqrt{\frac{T}{\rho_p} \left[ \left( \frac{m}{L_p} \right)^2 + \left( \frac{n}{W} \right)^2 \right]}, \quad (3.14)$$

where  $T$  is tension,  $\rho_p$  is density of the paper,  $L_p$  and  $W$  are length and width of the paper sheet, and  $m, n = 1, 2, 3, \dots$  are the mode numbers. Theoretical values of the mode frequencies predicted by Eqn. (3.14) are summarized in Table 3.5.

$m/n$	1	2	3	4	5
1	170.4	205.0	252.3	306.6	364.6
2	321.3	340.9	371.3	410.0	455.1
3	476.3	489.7	511.3	540.1	575.07
4	632.4	642.5	659.2	681.8	709.8
5	788.9	797.1	810.6	829.0	852.2

**Table 3.5** Frequencies of the membrane oscillation modes (Hz)

Table 3.5 shows that the predominant spectral peak of Fig. 3.26 corresponds to mode  $f_{21}$ . The oscillation amplitude of the predominant mode  $Y(f_{21}) = 0.085$  mm was two orders of magnitude lower than the maximum time-averaged displacement of the paper sheet from its neutral position (corresponding to the absence of the flow). In the time-averaged sense, the lowest distance between the surface of the air clamp and the paper sheet  $(y_p)_{min} = 0.27$  mm corresponded to the maximum displacement of 5.73 mm and was observed at  $x = -2$  mm.

It should be noted that the simplified model expressed by Eqn. (3.14) is valid under the assumption of the membrane vibrating in vacuum. In the realistic case when the modal wavelength is large compared to the distance between the paper sheet and the rigid surface of the air clamp, the added mass of the fluid can play a significant role. The assumption of the  $f_{21}$  membrane mode is supported by the mode shape information obtained during the high-speed photography of the oscillating paper sheet. The evidence, however, is not conclusive due to the limited field of view of the camera.

The substantial difference in the amplitude of the paper vibrations and the mean displacement of the paper sheet indicates that no significant coupling (resonance) exists between the unsteady flow structures and the oscillating paper

sheet. This observation is also supported by the estimates of the hydrodynamic frequencies of the absolute and convective instabilities of the separated shear layer ( $f_a \approx 3\text{-}7$  kHz,  $f_c \approx 26\text{-}40$  kHz), which are substantially larger (by an order of magnitude) than the measured frequency of paper vibration. These hydrodynamic frequencies, however, were estimated on the basis of the uncoupled shear layer oscillation for the case of classical BFS flows. This fact, in conjunction with the uncertainty in determining the vibration mode of the paper sheet, leads to the conclusion that a certain degree of coupling between the flow oscillations and the paper sheet vibration is possible. Unsteady pressure measurements for the case of a solid upper wall with the shape corresponding to the mean profile of the paper sheet provide improved estimates of the hydrodynamic frequencies associated with the transverse oscillations of the shear layer. Detailed discussion of these hydrodynamic frequencies is presented in Section 3.2.6.2

### **3.2.2 Time-averaged flow patterns**

Patterns of time-averaged velocity (Eqn.2.3), streamlines, and out-of-plane vorticity (Eqn. 2.4) are shown in Fig. 3.27 for the control case corresponding to the absence of the paper sheet (Case 1). Several values of the inflow velocity  $U_0$  were considered in this investigation. The inflow velocity was defined as the maximum streamwise velocity at  $x = 0$  (location of the BFS). The data presented herein corresponds to FOV1, with  $\Delta p = 18.6$  kPa ( $U_0 = 95$  m/s).

The mean reattachment length ( $\overline{X_r}$ ) defines the spatial extent of the recirculation zone that was present downstream of the BFS. The reattachment length is traditionally defined as the streamwise distance between the BFS ( $x = 0$ ) and the

location where the mean shear stress at the wall (the surface of the air clamp) is equal to zero. In the present investigation, the value of  $\overline{X_r}$  was determined from the time-averaged velocity field by calculating the location of the stagnation point on the surface of the air clamp downstream of the BFS. The velocity vector field for FOV1 had a physical resolution of  $29 \times 29 \mu\text{m}^2$ , which corresponded to the uncertainty of  $0.1h$  in the calculated reattachment length.

For the Case 1, shown in Fig. 3.27, the reattachment length  $\overline{X_r}$  was equal to  $2.7 h$ , where  $h$  is the height of the BFS. The relatively small value of  $\overline{X_r}$  was due to the downward deflection of the Coanda jet downstream of the BFS. This phenomenon is related to entrainment of the ambient fluid from the region above the air clamp into the jet, which is evident in the streamline pattern of Fig. 3.27. The fluid entrainment from only one side of the wall-bounded jet resulted in an asymmetric velocity profiles with respect to the core of the jet, which are shown in the top plot of Fig. 3.27. It should be noted that the observed reattachment length is more than two times smaller than that corresponding to the case of the fully-developed channel flow condition at similar Reynolds number (Dandois et al. (2007)).

The pattern of the time-averaged out-of-plane vorticity corresponding to Case 1 is shown in the bottom plot of Fig. 3.27. Regions of the elevated positive and negative values of vorticity correspond to the mixing layers located above and below the core of the Coanda jet. The peak positive value of the vorticity  $\langle \omega_z \rangle = 250,000 \text{ s}^{-1}$  was observed at  $x/h = -2.5$ , while the peak negative value  $\langle \omega_z \rangle = 650,000 \text{ s}^{-1}$  was found downstream of the flow separation point ( $x/h = 0.4$ ).

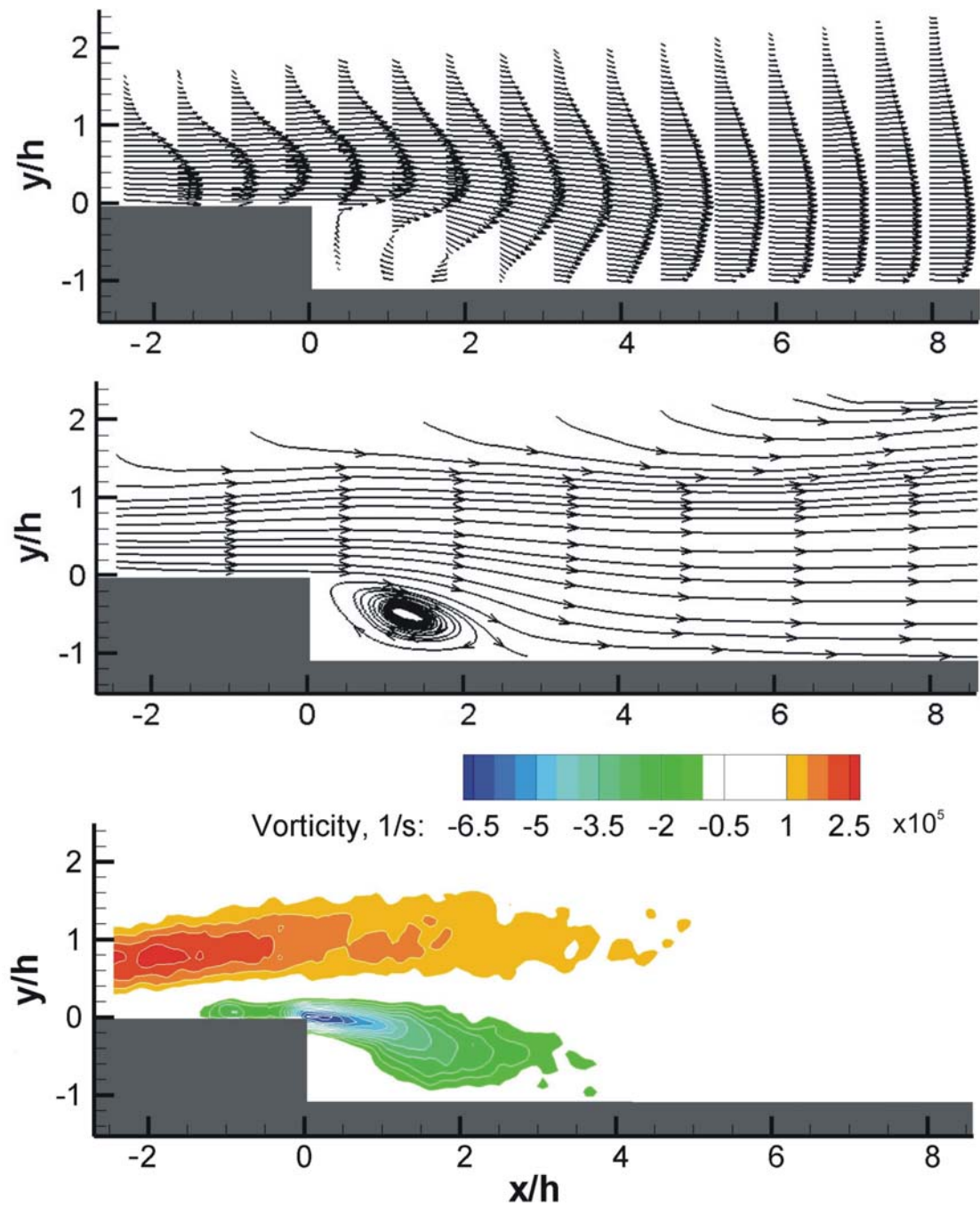


**Fig. 3.27** Time-averaged flow patterns corresponding to FOV1 for Case 1,  $U_0 = 95$  m/s

The presence of the flexible boundary (paper sheet) resulted in substantial changes in flow patterns, as it is shown in Fig. 3.28. The paper sheet is indicated by a bold black line in the plots of Fig. 3.28. The minimum distance between the paper

sheet and the surface of the air clamp was equal to  $(y_p)_{min} = 0.8h$ . The boundary of the flow field corresponded to a diverging channel, which formed between the surface of the air clamp and the paper sheet. The shape of the paper sheet, which formed as a result of the interaction with the unsteady separated flow, is described in detail in Section 3.2.1. Flow patterns of Fig. 3.28 correspond to the inflow velocity  $U_0 = 100$  m/s, and the Reynolds number based on the step height  $Re_h = (U_0h)/\nu = 3000$ , where  $\nu$  is the kinematic viscosity of air.

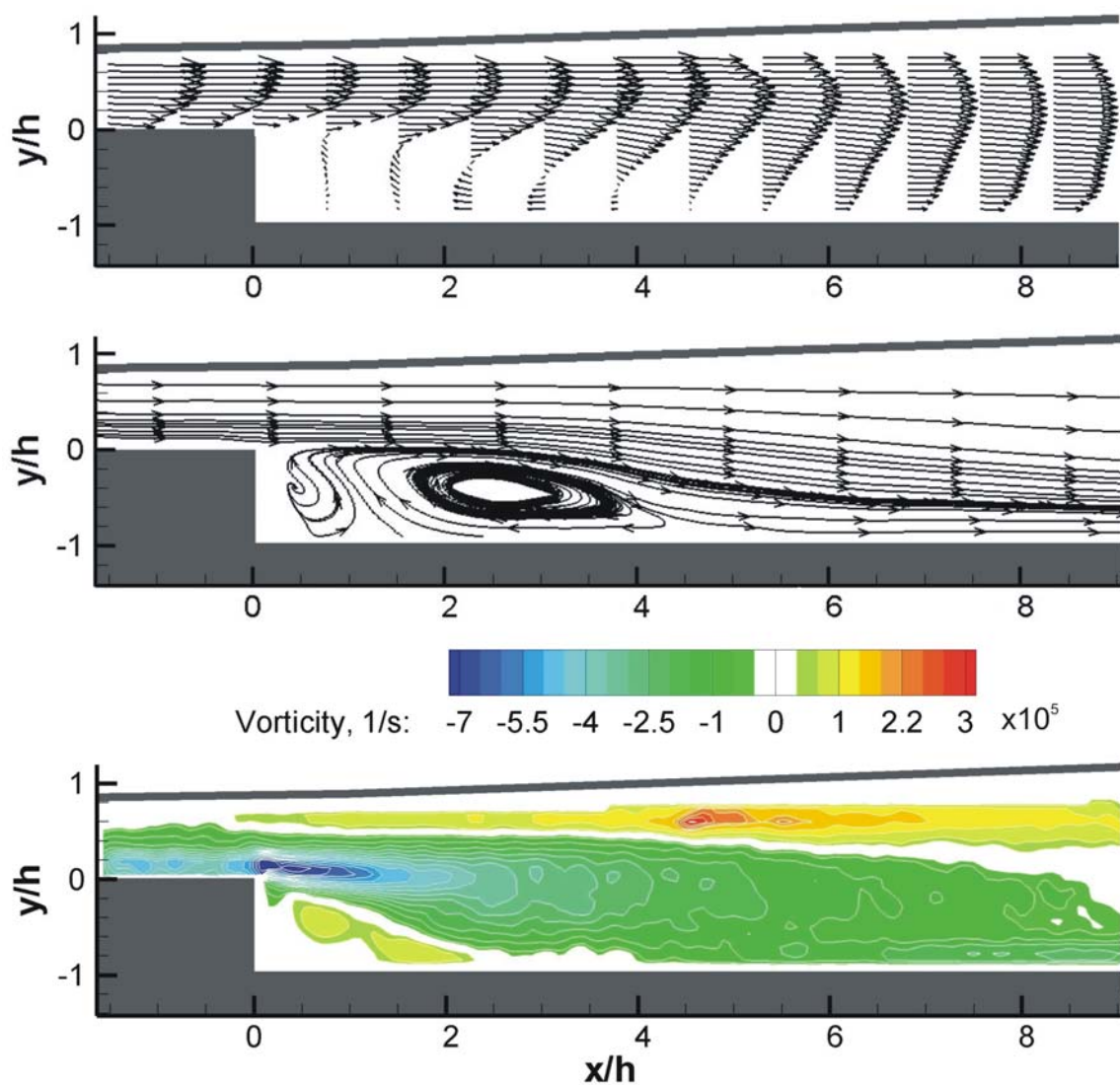


**Fig. 3.28** Time-averaged flow patterns corresponding to FOV1 for Case 2,  $U_0 = 100$  m/s

In Case 2, entrainment of the ambient air into the core of the wall-bounded jet was limited due to the presence of the paper sheet, which resulted in an increased value of the reattachment length  $\overline{X_r} = 4.8h$ . The maximum value of the time-averaged transverse velocity component  $\langle v \rangle = 8$  m/s was attained in the separated shear layer at  $x/h = 4$  and  $y/h = -0.07$ . Downstream of the BFS, the maximum streamwise velocity component rapidly decreased from  $\langle u \rangle = U_0 = 100$  m/s at  $x/h = 0$  to  $\langle u \rangle = 83$  m/s at  $x/h = 4.8$ .

The streamline pattern of Fig. 3.28 shows that the flow recirculation zone in Case 2 contained two counter-rotating cells. The primary cell extended from  $x/h = 1$  to  $x/h = 4.5$  and was characterized by clockwise rotation of the flow. The secondary (counter-clockwise) cell existed in the immediate vicinity of the BFS. The interface between the two recirculation zones is characterized by the net upward motion of the fluid. In this region, periodic injections of the slow-moving fluid into the fast-moving jet results in the onset of the absolute instability of the separated shear layer.

The bottom plot of Fig. 3.28 shows the pattern of the out-of-plane vorticity for Case 2,  $U_0 = 100$  m/s. In addition to the negative vorticity in the separated shear layer, positive vorticity values corresponding to counter-clockwise rotation of the flow were observed in the secondary recirculation zone downstream of the BFS. Moreover, positive vorticity was generated at the surface of the paper sheet downstream of the BFS. The maximum positive value of vorticity  $\langle \omega_z \rangle = 300,000$  s<sup>-1</sup> was attained in the vicinity of the upper boundary of the flow domain (the paper sheet) at  $x/h = 4.8$ , which corresponds to the location of the reattachment of the separated shear layer to the surface of the air clamp. Similarly to Case 1, the maximum negative value of the

time-averaged vorticity  $\langle \omega_z \rangle = 700,000 \text{ s}^{-1}$  was observed in the separated shear layer, immediately downstream of the BFS.

Time-averaged flow patterns for Case 2,  $U_0 = 120 \text{ m/s}$  ( $Re_h = 3600$ ) are shown in Fig 3.29. Due to the higher inflow velocity compared to the case illustrated in Fig. 3.28, the minimum distance between paper sheet and the surface of the air clamp decreased to  $(y_p)_{min} = 0.6h$ .

Flow patterns corresponding to  $U_0 = 120 \text{ m/s}$  (Fig. 3.29) are qualitatively similar to those corresponding to  $U_0 = 100 \text{ m/s}$  (Fig. 3.28). The increase in the inflow velocity resulted in the increased reattachment length  $\overline{X}_r = 5.3h$ . For the case of  $U_0 = 150 \text{ m/s}$  (not shown), the calculated reattachment length was equal to  $\overline{X}_r = 6.2h$ . It should be noted that the increase in the reattachment length was accompanied by the increasing angles of the inclination of the upper wall (paper sheet)  $\alpha_1$  and  $\alpha_2$ , as shown in Table 1. This trend is in agreement with the results corresponding to a rigid diverging channel configuration reported by Driver et al. Driver and Seegmiller (1985). When compared to Case 1 (no upper wall), the values of the reattachment length corresponding to Case 2 better approximate those reported for fully-developed flow over a BFS. Moreover, as it is shown in Section 3.2.5 (Fig. 3.36), velocity profiles in Case 2 are qualitatively similar to those corresponding to fully-developed inflow (Driver and Seegmiller (1985)).

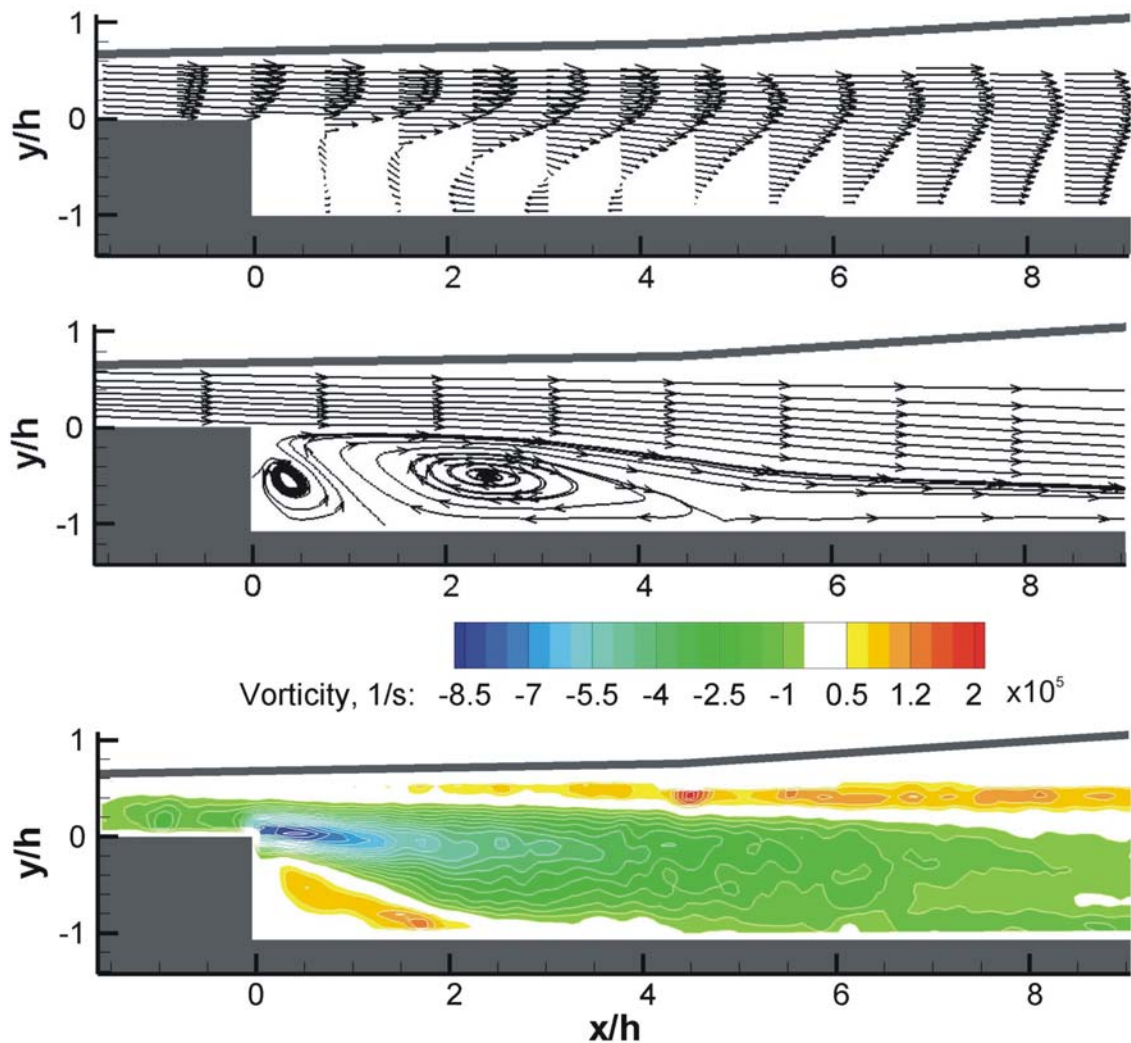


**Fig. 3.29** Time-averaged flow patterns corresponding to FOV1 for Case 2,  $U_0 = 120$  m/s

Fig. 3.30 shows time-averaged flow patterns corresponding to the control configuration involving a solid upper wall (Case 3,  $U_0 = 100$  m/s ). In the absence of the transverse oscillations of the upper wall that are characteristic of Case 2, the confinement effect of the wall on the incoming Coanda jet was more pronounced. In other words, the transverse ( $y$ -direction) flow component and the associated momentum flux are more restricted in the presence of the solid wall, compared to the case of the elastic wall that is free to vibrate. This effect results in the flow conditions at the point of separation ( $x = 0$ ) that better approximate the fully-developed channel

flow, which in turn leads to the increase of the reattachment length ( $\overline{X_r} = 5.6 h$ ). The structure of the flow recirculation region is qualitatively similar to that observed in the configuration involving a flexible upper wall (Case 2).

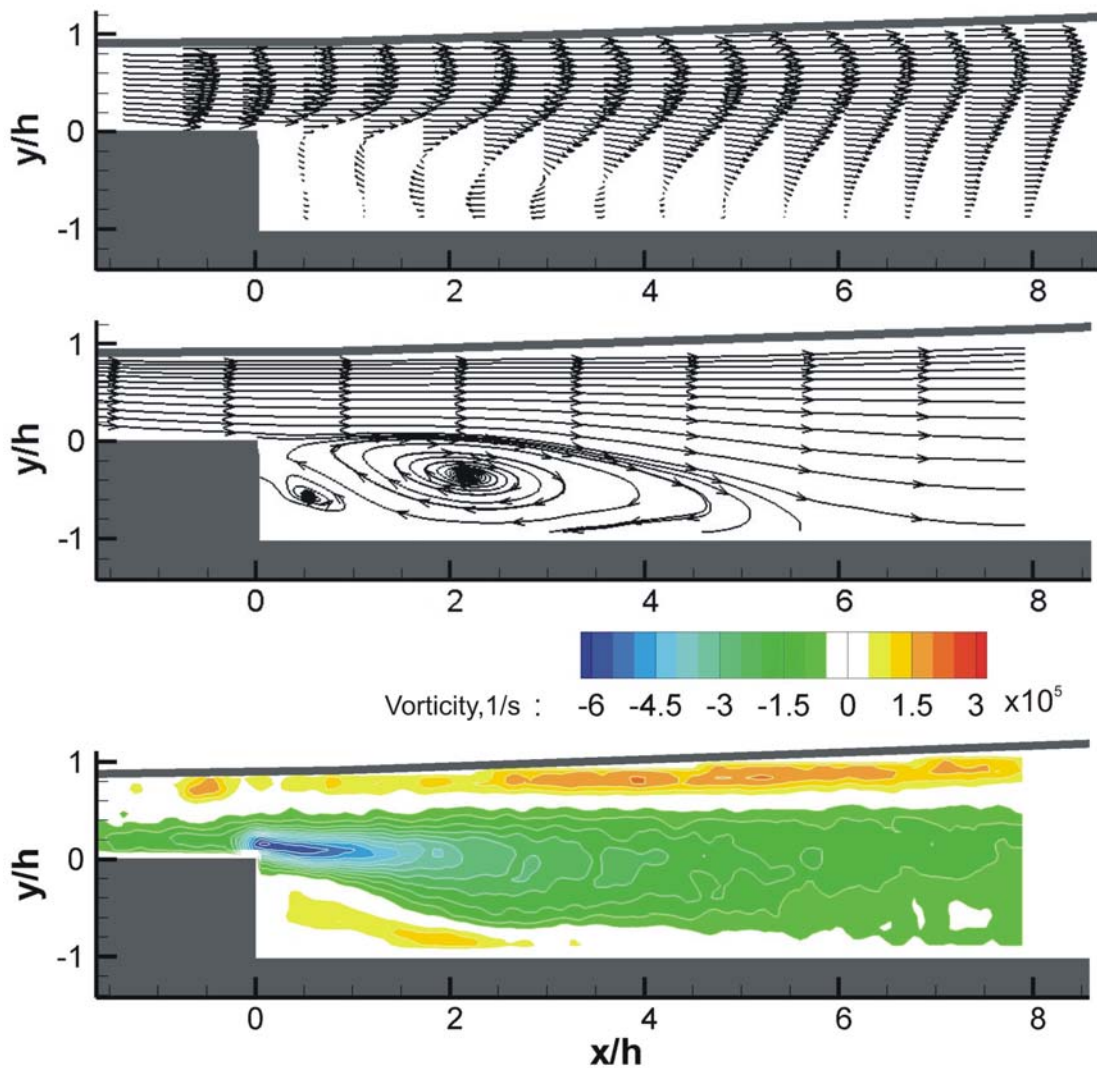


**Fig. 3.30** Time-averaged flow patterns corresponding to FOV1 for Case 3,  $U_0 = 100$  m/s

### 3.2.3 Evolution of vorticity

Development of the separated shear layer, which is related to transformation from the small-scale vortices to large-scale clusters of vorticity, can be quantified in terms of variation of vorticity thickness as a function of the downstream distance.

The distribution of the normalized vorticity thickness across the reattaching shear layer is shown in Fig. 3.31 for all considered cases.

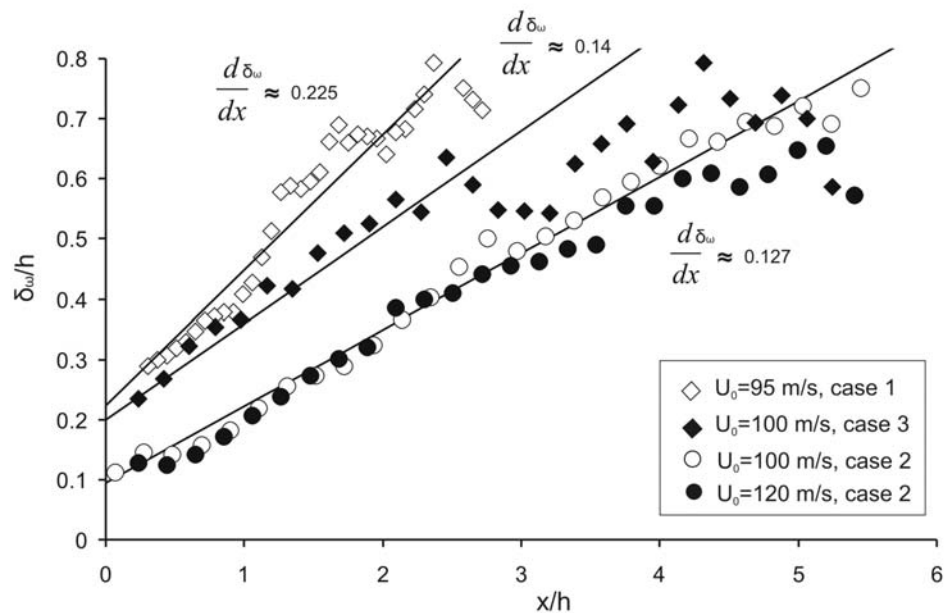


**Fig. 3.31** Distribution of vorticity thickness in the separated shear layer

In the Case 1, which corresponded to the absence of the paper sheet, the vorticity thickness increased with the downstream distance. The growth of the vorticity thickness across the entire FOV1 can be approximated by the relationship  $\delta_{\omega}/h = 0.225x/h + 0.22$ . The wavelength and scale of the vortices in the shear layer are expected to increase as the vorticity thickness increases Monkewitz and Huerre (1982). Therefore, the plot of Fig. 3.31 indicates that small-scale vortices were forming in the vicinity of the BFS, and that they subsequently transformed into large-scale vorticity concentrations at locations well downstream from the flow separation point.

In the Case 2, the presence of the paper sheet inhibited development of the vortical structures in the separated shear layer, which resulted in the lower growth rate

of the vorticity thickness. The vorticity thickness increased with the downstream distance according to the approximate relationship  $\delta_\omega/h = 0.127x/h + 0.95$  for both  $U_0 = 100$  m/s and  $U_0 = 120$  m/s.

In the case of the solid upper wall (Case 3), the trend of the vorticity thickness exhibited a higher overall rate of growth compared to that of Case 2 ( $\delta_\omega/h = 0.14x/h + 0.2$ ). This result is not intuitive, since the incoming Coanda jet flow is more confined by the presence of the solid upper wall. It is suggested that the oscillations of the paper sheet inhibit development of the shear layer instability downstream of the BFS and the associated formation of large-scale vortices. It should also be noted that, as it was described in Section 3.2.1, the dominant frequency of the paper sheet oscillation in Case 2 ( $f = 320$  Hz) is substantially (by an order of magnitude) different from the dominant frequency of the shear oscillation downstream of the BFS ( $f = 6000$  Hz). The difference between the growth rates of the shear layer that was observed between Cases 2 and 3 further supports the assumption of the absence of positive feedback (resonance) between the shear layer oscillations and the vibrations of the paper sheet.

It should be noted that in Case 1, the rate of growth of the vorticity thickness increased at the downstream distance of  $x/h \approx 1$ , which indicates the onset of rapid large-scale vortex formation at that distance. The deviations of the vorticity thickness from the linear trend were less pronounced in Case 2, as the oscillations of the paper sheet interfere with the development of the large-scale vortical structures.

### **3.2.4 Turbulence statistics**

The values of velocity fluctuations and their correlations (Eqns. 2.5-2.7) for the Case 1 are presented in terms of patterns of dimensionless  $\langle u_{\text{rms}} \rangle$ ,  $\langle v_{\text{rms}} \rangle$ , and

$\langle u'v' \rangle$  in Fig. 3.32. Elevated values of  $\langle u_{rms} \rangle / U_0$  were observed downstream of the BFS in the regions corresponding to the upper and the lower shear layers that formed on the periphery of the air jet. The corresponding  $\langle v_{rms} \rangle / U_0$  plot shows the peak value of 0.14 in the vicinity of the reattachment point ( $x/h = 2$ ). The velocity correlation  $\langle u'v' \rangle / (U_0)^2$  that corresponds to the dominant Reynolds shear stress component exhibited high negative values in the separated shear layer. In addition, the elevated positive values were observed in the region corresponding to the upper shear layer, which formed between the fast-moving core of the jet and the quiescent fluid.

Patterns of the time-averaged turbulence statistics corresponding to Case 2 ( $U_0 = 100$  m/s) are shown in Fig. 3.33. In contrast to the Case 1, the elevated values of  $\langle u_{rms} \rangle / U_0$ ,  $\langle v_{rms} \rangle / U_0$ , and  $\langle u'v' \rangle / (U_0)^2$  in Fig. 3.33 extended over a larger region downstream of the BFS. This observation is consistent with the increased interaction between the separated shear layer and the recirculating flow region through periodic injections of the fluid into the core of the jet from the interface region between the two counter-rotating vortices, which were observed in Fig. 3.28.

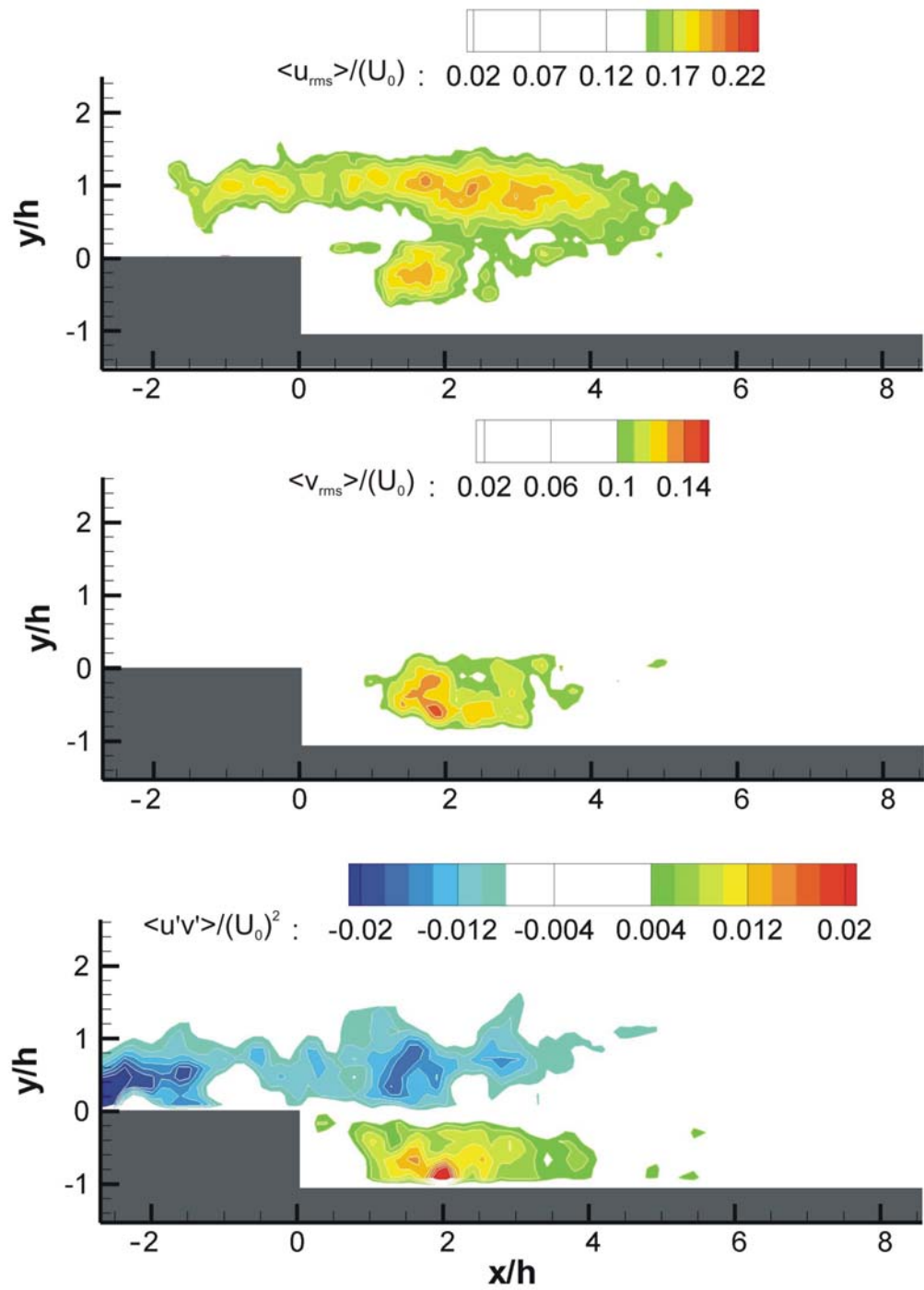
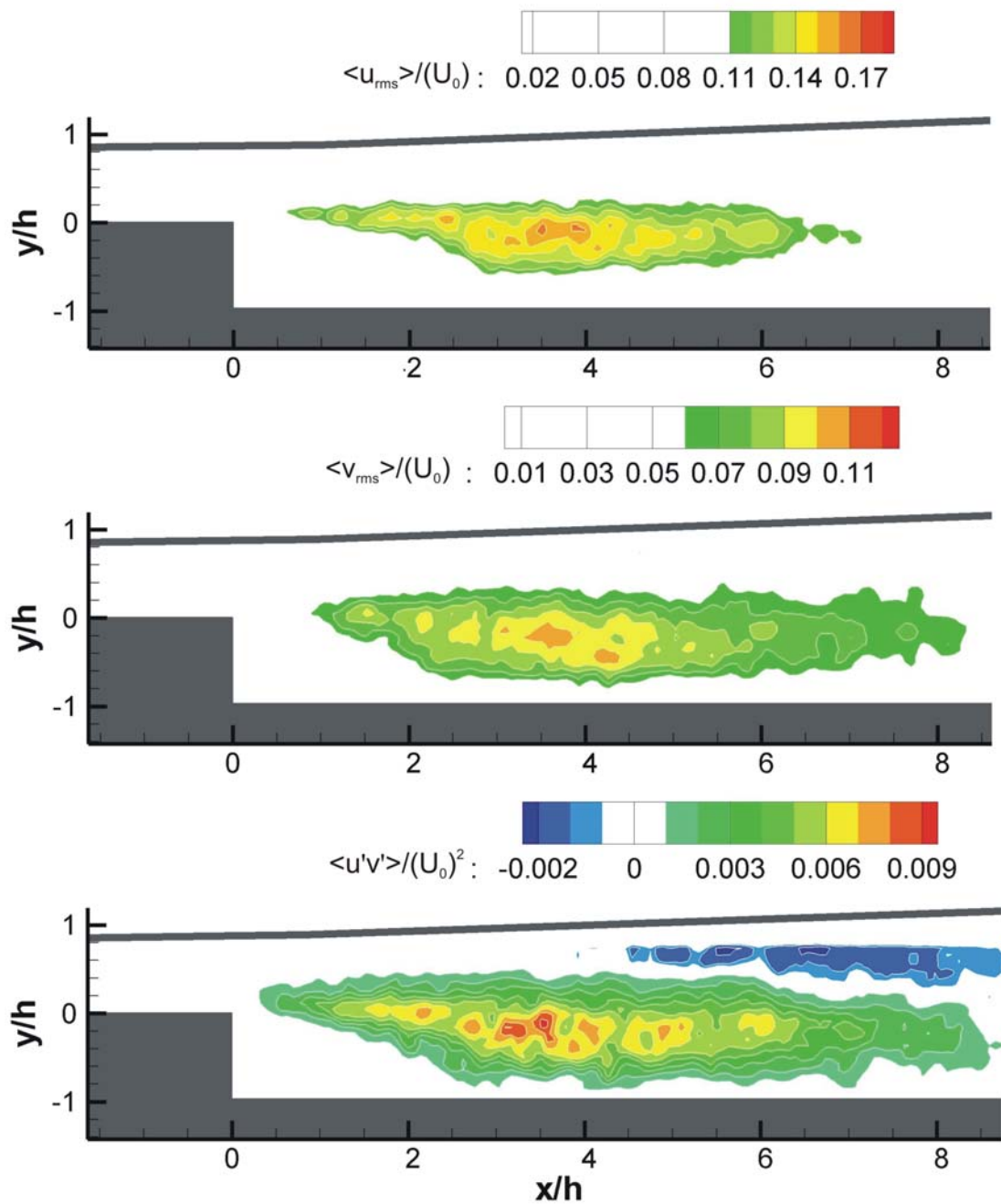


Fig. 3.32 Time-averaged turbulence statistics corresponding to FOV1 for Case 1,  $U_0 = 95$  m/s



**Fig. 3.33** Time-averaged turbulence statistics corresponding to FOVI for Case 2,  $U_0 = 100$  m/s

Patterns of the turbulence statistics for the case of the solid upper wall (Case 3) that are shown in Fig. 3.34 are qualitatively similar to those corresponding to Case 2. The increased confinement of the wall-bounded jet caused the maximum values of  $\langle u_{rms} \rangle / U_0$ ,  $\langle v_{rms} \rangle / U_0$ , and  $\langle u'v' \rangle / (U_0)^2$  to occur farther downstream, at  $x/h = 4.3$ ,  $4.5$ ,

and 4.3, respectively, as compared to  $x/h = 3.5$ , 3.5, and 3.3 for the case shown in Fig. 3.33.

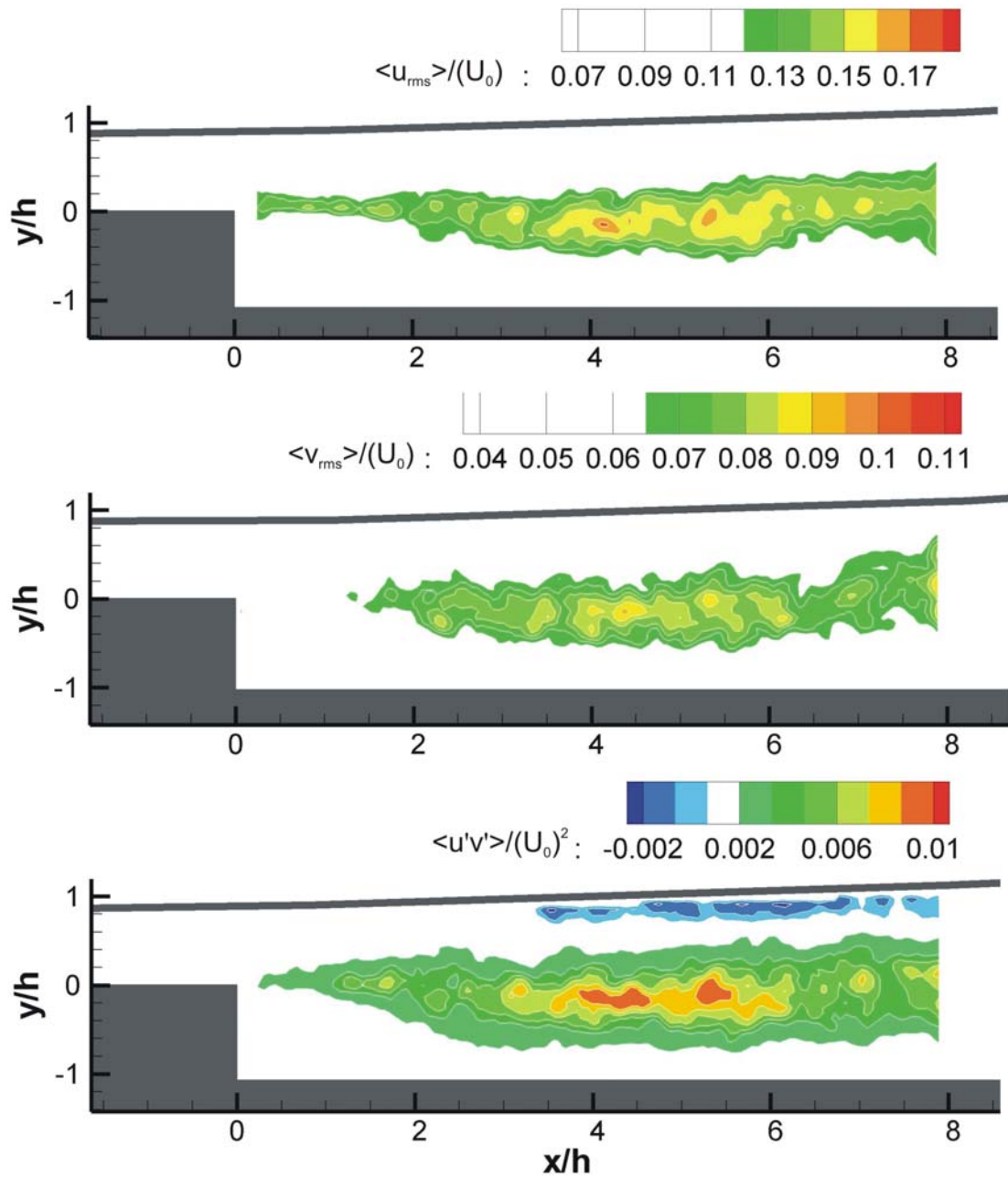


**Fig. 3.34** Time-averaged turbulence statistics corresponding to FOV1 for Case 3,  $U_0 = 100$  m/s

### 3.2.5 Velocity and turbulence profiles

Distributions of the time-averaged streamwise velocity component as functions of the distance from the air clamp surface in the transverse ( $y$ ) direction at several locations downstream of the BFS are shown in Figs. 3.35, 3.36 and 3.37 for Cases 1, 2 and 3 respectively.

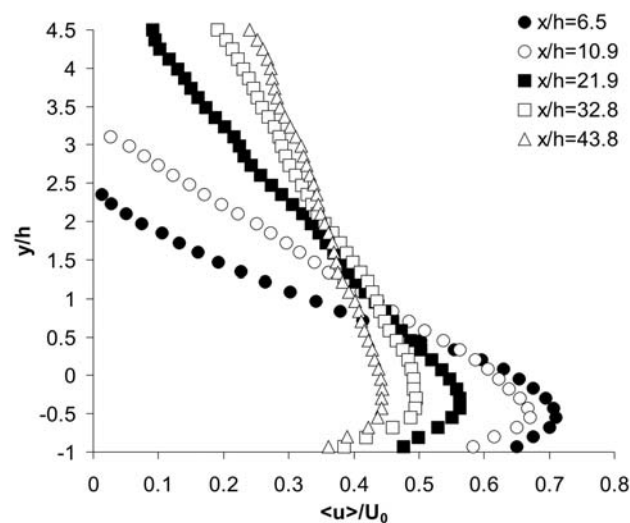


**Fig. 3.35** Distributions of time-averaged horizontal velocity as a function of vertical coordinate corresponding to FOV3 for Case 1,  $U_0 = 95$  m/s

In all cases, the peak velocity decreased with the increasing downstream distance. Moreover, in the Case 1, entrainment at the upper side of the jet resulted in a rapid growth of the width of the jet. In Cases 2 and 3 (Figs. 3.36 and 3.37), the growth of the jet in the cross-flow direction is inhibited by the presence of the upper wall. It should be noted that the velocity profiles of Figs. 3.36 and 3.37 are not symmetric with respect to the core of the jet due to the inherent asymmetry of the boundary of the flow domain and the associated difference in the pressure gradients along the bottom wall (the surface of the air clamp) and upper wall.

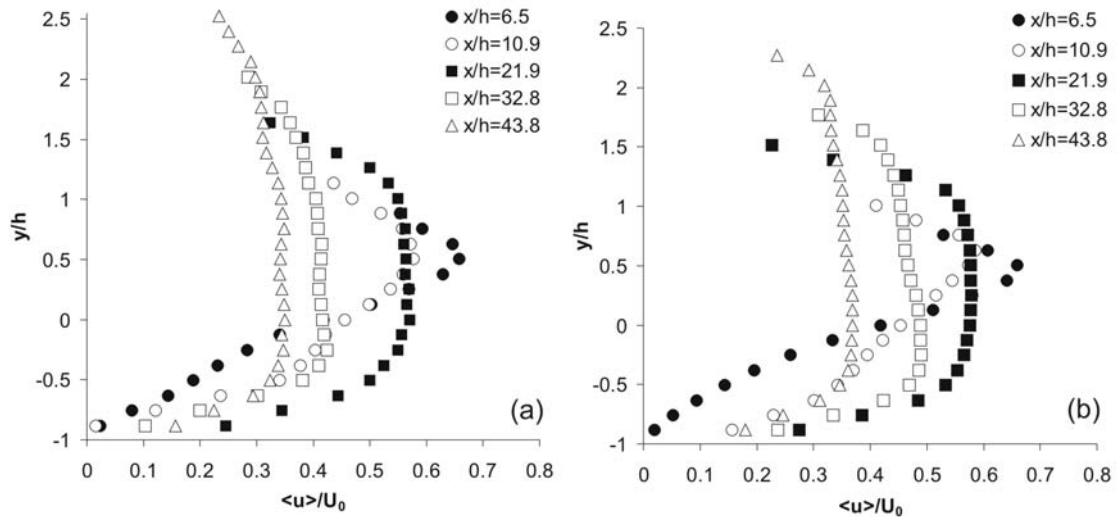


**Fig. 3.36** Distributions of time-averaged horizontal velocity as a function of vertical coordinate corresponding to FOV3 for Case 2, (a):  $U_0 = 100$  m/s, (b):  $U_0 = 120$  m/s

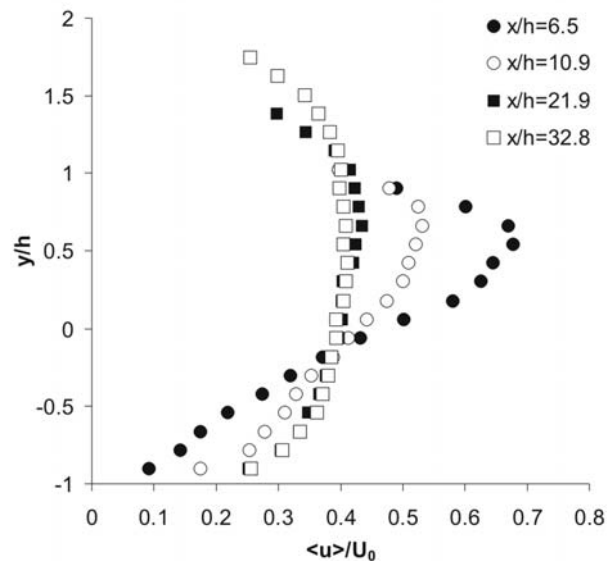


**Fig. 3.37** Distributions of time-averaged horizontal velocity as a function of vertical coordinate corresponding to FOV3 for Case 3,  $U_0 = 100$  m/s

Profiles of the time-averaged turbulence statistics for Case 2 ( $U_0 = 100$  m/s) at several locations downstream of the BFS are shown in Fig. 3.38. The maximum amplitude of the velocity fluctuations decreased with the downstream distance. The high values that were observed in the vicinity of the BFS correspond to the

interactions between the fast-moving fluid in the core of the jet and the counter-rotating flow structures in the recirculation region that are described in Section 3.2.2.

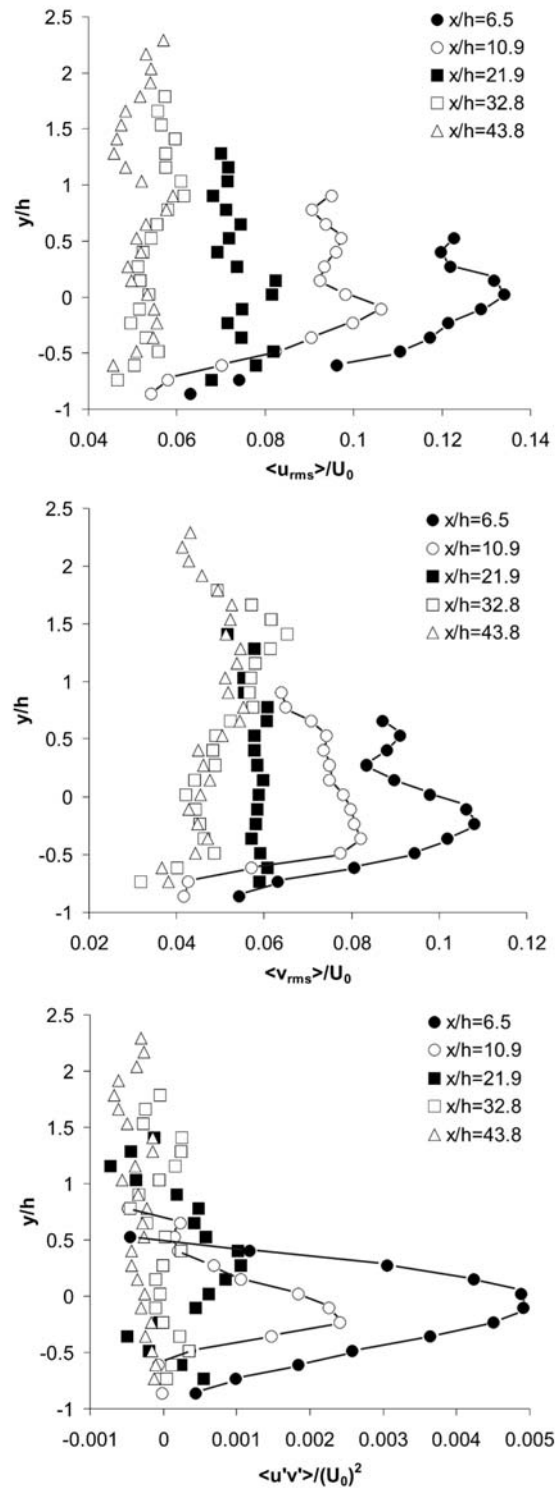


**Fig. 3.38** Time-averaged turbulence statistics corresponding to FOV3 for Case 2,  $U_0 = 100$  m/s

The profiles of  $\langle u_{rms} \rangle / U_0$  and  $\langle v_{rms} \rangle / U_0$  exhibit two local maxima downstream of the BFS. This double-peak structure is qualitatively similar to that observed in the asymmetric diffuser flows Wu et al. (2006). Moreover, the velocity profiles of Fig. 3.36 and the turbulence statistics of Fig. 3.38 share similarity with the corresponding parameters of a classical Couette-Poiseuille flow between a stationary wall and a belt moving in a streamwise direction Nakabayashi et al. (2004).

### 3.2.6 Pressure distribution along the upper wall

#### 3.2.6.1 Distribution of static pressure

Distribution of the static pressure at the solid upper wall (Case 3) was acquired by the array of taps that is indicated in Fig. 2.8. Distribution of the static pressure coefficient as a function of the downstream distance from the BFS is shown in Fig. 3.39.

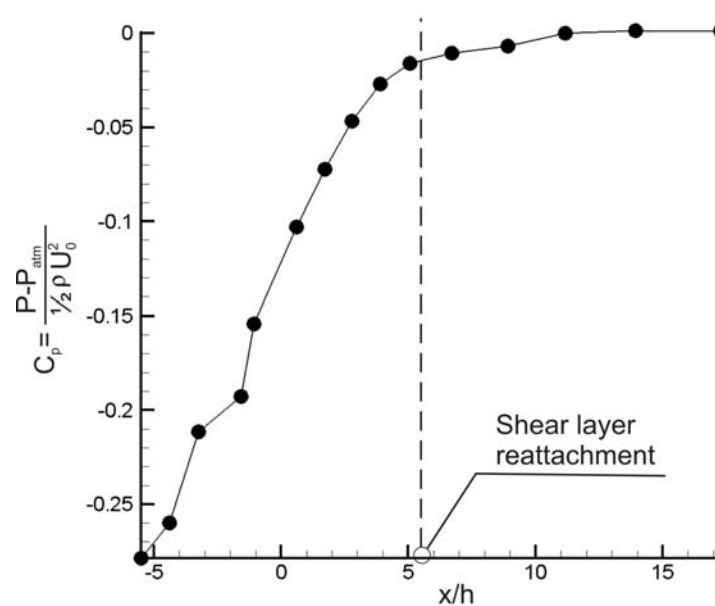
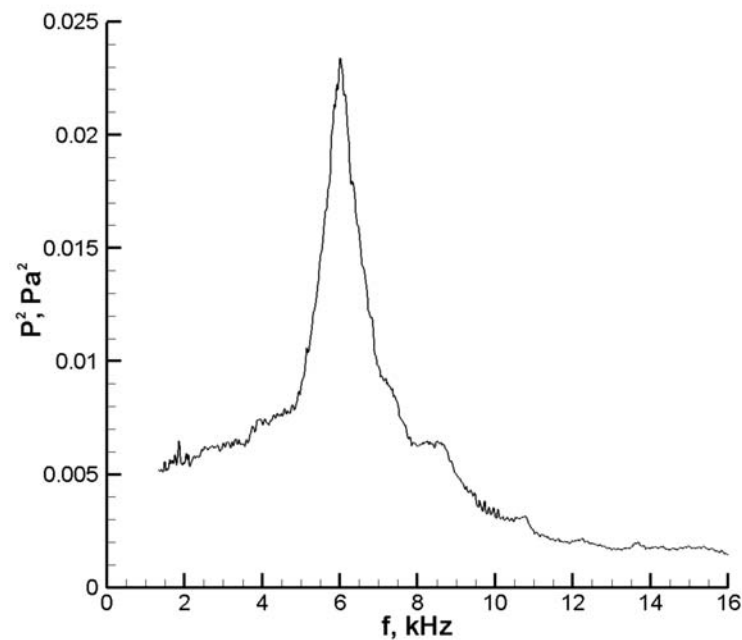


Fig. 3.39 Distribution of static pressure corresponding to FOV3 for Case 3,  $U_0 = 100$  m/s

The region between  $x/h = -3$  and  $x/h = -1.5$ , which exhibits a prominent variation of the slope of the pressure coefficient, corresponds to impingement of the Coanda jet onto the solid upper wall. The location of the reattachment of the separated shear layer to the bottom wall (surface of the air clamp) is indicated by a dashed vertical line. The gradient of the static pressure coefficient upstream of the reattachment was equal to  $h(dC_p/dx) = 0.025$ , which is approximately 40% higher than the value reported by Driver and Seegmiller (1985) for a similar diverging channel configuration with a fully-developed inflow condition. As the local flow velocity decreases, the static pressure coefficient increases with the downstream distance and reaches zero value (corresponding to the atmospheric pressure) at  $x/h = 11.5$ , i.e. approximately six step heights downstream of the shear layer reattachment to the bottom wall.

### *3.2.6.2 Unsteady pressure downstream of the BFS*

The unsteady pressure at the solid upper wall (Case 3) was measured by a pressure transducer shown in Fig. 2.8. The pressure transducer was located in the vicinity of the shear layer reattachment to the bottom wall (surface of the air clamp) at  $x/h = 6$ . The corresponding power spectrum, which is shown in Fig. 3.40 exhibits a dominant peak at  $f = 6000$  Hz.



**Fig. 3.40** Spectrum of the unsteady pressure downstream of the BFS ( $x/h = 6$ ). Case 3,  $U_0 = 100$  m/s

This frequency corresponds to the absolute instability of the oscillating shear layer. The corresponding Strouhal number based on the reattachment length is  $Sr_a = f_a L / U_0 = 0.156$ , which is within the range of Strouhal numbers of classical BFS flows (without Coanda effect) reported in literature ( $0.08 < Sr_a < 0.18$ ) (Dandois et al. (2007)). The difference between the hydrodynamic frequency of the shear layer oscillation and the dominant frequency of the paper sheet vibration ( $f = 320$  Hz), in conjunction with the small amplitude of the paper sheet vibrations, supports the hypothesis of the absence of flow-induced resonance. However, as it was pointed out in Section 3.2.1, the unsteady pressure measurements correspond to uncoupled flow oscillations, as the upper wall in Case 3 was not vibrating.

## CHAPTER 4

### CONCLUSIONS AND RECOMMENDATIONS

#### 4.1. SIDE BRANCH RESONATOR

Acoustic response of a coaxial side branch resonator with fully-turbulent inflow was investigated using a combination of digital particle image velocimetry (DPIV) and the measurements of unsteady acoustic pressure. In the case of the cross-junction without splitter plates, resonant flow tones corresponded to two hydrodynamic modes of shear layer oscillation and were characterized in terms of acoustic pressure amplitude, frequency, and  $Q$ -factor of the dominant pressure peak. Frequencies of the resonant acoustic modes and corresponding mode shapes were also simulated numerically. The calculated frequencies were in good agreement with the measured values, as well as with the frequencies predicted by a theoretical model for long coaxial side branches.

In addition, the effects of the resonator geometry on the associated flow patterns were quantified. Bluff rectangular plates were placed in the vicinity of the side branch openings. This modification had a significant influence on the separated-reattaching shear layers and resulted in the attenuation of the first hydrodynamic oscillation mode, which generally decreases growth rates of the shear layers. Thus, a substantial reduction of the pulsation amplitude and strength of the acoustic source was reported. It should be noted, that in this regard, the long plate ( $c/t = 5.4$ ) has

significantly outperformed the short splitter plate ( $c/t = 2.7$ ). This can be attributed to the difference in separation and reattachment processes due to position of the bluff plates with respect to the upstream corners of the cavity and difference in their lengths, as it was described in detail in Section 3.1.3.3.

Consequently, these studies can lead to the development of various control strategies in application to the side branch resonators. In particular, preliminary experiments involved extension of the length of the splitter plates up to the upstream corners of the cavity ( $c/t = 8.1$ ,  $c/t = 10.8$ ). In this case, separation regions at the leading edge of the plate strongly interacted with main shear layers, suppressing the flow tones and instead leading to the generation of the background noise. It should be noted, however, that position of the splitter plate in the middle of the cross-junction is not acceptable in some applications (e.g. gate valves in the cooling systems for nuclear reactors). Moreover, conventional vortex generators might also be inappropriate, because they extend into the cross-junction region. To overcome these constraints splitter plates can be positioned inside the main duct in the vicinity of the upstream corners of the cavity.

In contrast to the earlier works, the present study represents the first application of the Howe's integral relation in conjunction with global quantitative flow imaging and numerical simulation of the two-dimensional acoustic wave field. This study resulted in the comprehensive semi-empirical approach, which is capable of providing the detailed information regarding the acoustic source structure, even in the presence of complex hydrodynamic interactions between the vortices in the separated shear layers. Moreover, global, quantitative imaging of the acoustically-coupled flow in conjunction with numerically simulated distribution of acoustic

velocity yields estimates of the net generated acoustic power and visco-thermal damping during a typical period of acoustic oscillation.

In addition, the presence of bluff splitter plates in the cross-junction has pronounced effect on the acoustic power source structure due to increased interaction between the unsteady shear layers that form across the side branches and at the leading/trailing corners of plates. In contrast, to the cases of  $c/t = 0$  and  $c/t = 2.7$  the spatial structure of the acoustic power producing region doesn't change from independent sources to a large single source for a long splitter plate ( $c/t = 5.4$ ), leading to the lower values of the net generated power. In addition, strong radiation into main duct was confirmed in the present side branch configuration based on energy balance provided by values of visco-thermal damping and the net generated acoustic power. Acoustic flux into the main duct in conjunction with flow separation at the downstream corners of the side branches results in formation of additional sources of acoustic power.

## **4.2 AIR CLAMP**

Flow-structure interactions aspects of the air clamp device in proximity to a stationary paper sheet were investigated experimentally using a combination of DPIV and high-speed photography. In addition, a control case that involved a rigid wall in place of the paper sheet was studied using a combination of DPIV and pressure measurements. The geometry of the wall corresponded to the time-averaged profile of the paper sheet at the same value of the inflow velocity. The profile of the paper sheet during the operation of the air clamp could be approximated by linear segments,

which, in conjunction with the surface of the air clamp, resulted in a diverging channel configuration.

During the operation of the air clamp, the paper sheet was displaced from its original position due to fast-moving wall-bounded jet flow along the surface of the air clamp. The paper sheet was undergoing transverse oscillations with frequencies corresponding to those of the theoretically-predicted modes of vibration of a rectangular membrane. The amplitude of the oscillation was two orders of magnitude lower than the maximum time-averaged displacement of the paper sheet from its neutral position (corresponding to the absence of the flow). The substantial difference between the amplitude of the paper vibrations and its mean displacement, as well as the large difference between the measured frequencies of paper vibration and estimated hydrodynamic frequencies, indicate that no significant coupling (resonance) existed between the unsteady flow structures and the oscillating paper sheet. This hypothesis is also supported by the unsteady pressure measurements corresponding to the uncoupled shear layer oscillation in proximity to the solid upper wall. However, potential for such coupling exists due to the uncertainty associated with the vibration mode of the paper sheet. Thus, in future work it is recommended to perform correlation analysis between unsteady flow structures and paper sheet vibration via simultaneous measurements of unsteady pressure at the bottom wall of the air clamp and high-speed photography (or vibration measurements) of the paper-sheet.

Global, quantitative flow patterns, which were acquired for a range of inflow velocities, indicate qualitative similarity between the air flow over the surface of the air clamp and that of a two-dimensional backward-facing step (BFS) flow. In contrast to the classical case, which involves fully-developed boundary layer at the point of

flow separation, proximity of the curved nozzle with associated Coanda effect and the adverse pressure gradient imposed by the diverging channel geometry resulted in a substantial decrease of the flow reattachment length. Transverse profiles of the time-averaged flow velocity and turbulence statistics of the flow in the air clamp share qualitative similarity with the corresponding parameters of diverging channel flows as well as classical Couette-Poiseuille flows.

Practical recommendations for industrial application of the air clamp are summarized in Appendix F. These recommendations are generally related to characterization of the flow-induced force acting on the paper sheet and development of methods to control flow separation from the paper-sheet.

## REFERENCES

- Adrian RJ (1991) Particle-Imaging Techniques for Experimental Fluid Mechanics. Annual Review of Fluid Mechanics 23(1): 261-304.
- Adrian RJ, Christensen KT and Liu ZC (2000) Analysis and interpretation of instantaneous turbulent velocity fields. Experiments in Fluids 29(3): 275-290.
- Ahuja KK and Mendoza J (1995). Effects of cavity dimensions, boundary layer and temperature on cavity noise with emphasis on benchmark data to validate computational aeroacoustic codes. Technical Report CR-4653., NASA.
- Allery C, Guerin S, Hamdouni A, et al. (2004) Experimental and numerical POD study of the Coanda effect used to reduce self-sustained tones. Mechanics Research Communications 31: 105-120
- Armaly B, Durst F, Pereira JCF, et al. (1983) Experimental and theoretical investigation of backward-facing step flow. Journal of Fluid Mechanics 127(473).
- Arthurs D, Ziada S and Bravo R (2006). *Flow Induced Acoustic Resonances of an Annular Duct with Co-Axial Side Branches*. ASME Pressure Vessels and Piping Division Vancouver, BC, Canada.
- Azad RS (1996) Turbulent flow in a conical diffuser: A review. Experimental Thermal and Fluid Science 13(4): 318-337.
- Baldwin RM and Simmons HR (1986) Flow-induced vibration in safety relief valves. ASME Journal of Pressure Vessel Technology 108(3): 267-272.
- Blake WK (1986). Mechanics of Flow-Induced Sound and Vibration. New York, Academic Press, INC.
- Bres GA and Colonius T (2007) Direct numerical simulations of three-dimensional cavity flows. AIAA(3405).
- Brown GL and Roshko A (1974) Density Effects and Large Structure in Turbulent Mixing Layers. Journal of Fluid Mechanics 64(JUL24): 775-816.

- Buice CU (1997). Experimental investigation of flow through an asymmetric plane diffuser. Department of Mechanical Engineering, Stanford University, CA, USA. PhD thesis.
- Champagne FH, Pao YH and Wygnanski I (1976) On the two-dimensional mixing region. *Journal of Fluid Mechanics* 74: 209-250.
- Chen YN and Sturchler R (1977). *Flow-induced vibrations and noise in a pipe system with blind branches due to coupling of vortex shedding*. Internoise Zurich.
- Cherry NJ, Hillier R and Latour ME (1983) The unsteady structure of two-dimensional separated and reattaching flow. *Journal of Wind Engineering and Industrial Aerodynamics* 11: 95-105.
- Chun KB and Sung HJ (1996) Control of turbulent separated flow over a backward-facing step by local forcing. *Experiments in Fluids* 21: 417-426.
- Coanda H (1932). Procédé de propulsion dans un fluide. Brevet Invent. Gr. Cl. 2. Republique Francaise. no. 651577.
- Dandois J, Garnier E and Sagaut P (2007) Numerical simulation of active separation control by a synthetic jet. *Journal of Fluid Mechanics* 574: 25-58.
- DeMetz FC and Farabee TM (1977) Laminar and turbulent shear flow induced cavity resonances. AIAA 77(1293).
- Dequand S, Hulshoff, S. J., Hirschberg, A. (2003a) Self-sustained oscillations in a closed side branch system. *Journal of Sound and Vibration* 263: *Journal of Sound and Vibration*.
- Dequand S, Willems JFH, Leroux M, et al. (2003b) Simplified models of flue instruments: Influence of mouth geometry on the sound source. *Journal of Acoustical Society of America* 113: 1724-1735.
- Djilali N and Gartshore IS (1991) Turbulent flow around a bluff rectangular plate. Part 1: Experimental investigation. *Journal of Fluids Engineering* 113: 51-59.
- Driver DM and Seegmiller HL (1985) Features of a Reattaching Turbulent Shear-Layer in Divergent Channel Flow. *Aiaa Journal* 23(2): 163-171.
- Eaton JK and Johnston JP (1980). Turbulent flow reattachment: an experimental study of the flow and structure behind a backward-facing step. Technical Report MD 39, Stanford University. Department of Mechanical Engineering.

- Elder LF, T.M. F and DeMetz FC (1982) Mechanisms of flow-excited cavity tones at low Mach number. *Journal of Acoustical Society of America* 72(2): 532-549.
- Faure TM, Adrianos P, Lusseyran F, et al. (2007) Visualizations of the flow inside an open cavity at medium range Reynolds numbers. *Experiments in Fluids* 42: 169-184.
- Geveci M, Oshkai P, Rockwell D, et al. (2003) Imaging of the self-excited oscillation of flow past a cavity during generation of a flow tone. *Journal of Fluids and Structures* 18: 665-694.
- Gullman-Strand J, Tornblom O, Lindgren B, et al. (2004) Numerical and experimental study of separated flow in a plane asymmetric diffuser. *International Journal of Heat and Fluid Flow* 25(3): 451-460.
- Han G, de Zhou M and Wagnanski I (2006) On streamwise vortices and their role in the development of a curved wall jet. *Physics of Fluids* 18: 95-104.
- Hart DP (2000) PIV error correction. *Experiments in Fluids* 29(1): 13-22.
- Hasan MA (1992) The flow over a backward-facing step under controlled perturbation: laminar separation. *Journal of Fluid Mechanics* 238: 73-96.
- Hillier R and Cherry NJ (1981) The effect of stream turbulence on separation bubbles. *Journal of Wind Engineering and Industrial Aerodynamics* 8: 49-58.
- Hinds WC (1999). Aerosol technology: properties, behavior and measurement of airborne particles. New York, Wiley.
- Howard A (2004). Design of a Flow-Acoustic Experimental Facility. Mech 499, University of Victoria.
- Howe MS (1975) Contributions to Theory of Aerodynamic Sound, with Application to Excess Jet Noise and Theory of Flute. *Journal of Fluid Mechanics* 71(OCT28): 625-673.
- Howe MS (1984) On the Absorption of Sound by Turbulence and Other Hydrodynamic Flows. *Ima Journal of Applied Mathematics* 32(1-3): 187-209.
- Howe MS (1986) Attenuation of sound due to vortex shedding from a splitter plate in a mean flow duct. *Journal of Sound and Vibration* 105(3): 385-396.
- Howe MS (2003) Theory of Vortex Sound. Cambridge University Press
- Huang H, Dabiri D and Gharib M (1997) On error of digital particle image velocimetry. *Measurement Science & Technology* 8: 1427-1440.

- Jungowski WM, Botros KK and Studzinski W (1989) Cylindrical side-branch as tone generator. *Journal of Sound and Vibration* 131: 265-285.
- Karadogan and Rockwell D (1983) Towards attenuation of self-sustained oscillations of a turbulent jet through a cavity. *Journal of Fluids Engineering* 105(3): 335-340.
- Kinsler LE, Frey AR, Coppens AB, et al. (2000) Fundamentals of Acoustics. Forth ed., New York: Jon Wiley & Sons, Inc.
- Kiya M and Sasaki K (1983) Structure of turbulent separation bubble. *Journal of Fluid Mechanics* 137: 83-113.
- Kriesels PC, Peters MCAM, Hirschberg A, et al. (1995) High amplitude vortex-induced pulsations in a gas transport system. *Journal of Sound and Vibration* 184(2): 343-368.
- Lakshmana Rao C, Lakshminarasimhan J, Sethuraman R, et al. (2004). *Engineering Mechanics: Statics and Dynamics*, Prentice-Hall of India.
- Landau LD and Lifshitz EM (1987) Fluid Mechanics. 2nd English ed. Vol. 6., New York: Pergamon Press.
- LaVision (2002). FlowMaster Manual. Gottingen, LaVision.
- Le H, Moin P and Kim J (1997) Direct numerical simulation of turbulent flow over a backward-facing step. *Journal of Fluid Mechanics* 330: 349-374.
- Leontev AI, Shishov EV and Vechkanov SU (1994) The influence of coherent structures on turbulent transfer of heat and momentum in a separated region behind backward-facing step. *Doklady Akademii Nauk* 336(6): 763-765.
- Lin JC and Rockwell D (2001) Organized oscillations of initially turbulent flow past a cavity. *Aiaa Journal* 39(6): 1139-1151.
- Liversey JL, Jackson JD and Southern CJ (1962) The static-hole error problem: an experimental investigation of errors for holes of varying diameter and depth. *Aircraft Engineering* 34:43-47.
- Maul DJ and East LF (1963) Three-dimensional flow in cavities. *Journal of Fluid Mechanics* 16: 620-632.
- Moeller S, Axelrod S and Luis J (2005). Air clamp stabilizer for continuous web materials. United States, Honeywell International, Inc. US 6936137 B2.

- Monkewitz PA and Huerre P (1982) Influence of the Velocity Ratio on the Spatial Instability of Mixing Layers. *Physics of Fluids* 25(7): 1137-1143.
- Nakabayashi K, Kitoh O and Katoh Y (2004) Similarity laws of velocity profiles and turbulence characteristics of Couette-Poiseuille turbulent flows. *Journal of Fluid Mechanics* 507: 43-69.
- Nelson PA, Halliwell NA and Doak PE (1981) Fluid dynamics of a flow excited resonance. Part I: Experiment. *Journal of Sound and Vibration* (78): 15-38.
- Nelson PA, Halliwell NA and Doak PE (1983) Fluid-Dynamics of a Flow Excited Resonance .2. Flow Acoustic Interaction. *Journal of Sound and Vibration* 91(3): 375-402.
- Neuendorf R, Lourenco L and Wygnanski I (2004) On large streamwise structures in a wall jet flowing over a circular cylinder. *Physics of Fluids* 16: 21-58
- Neuendorf R and Wygnanski I (1999) On a turbulent wall jet flowing over a circular cylinder. *Journal of Fluid Mechanics* 381(1).
- Newman BG (1961). The deflexion of plane jets by adjacent boundaries — Coanda effect. Boundary Layer and Flow Control. Lachmann GV. New York, Pergamon Press,; 232-265.
- Okwuobi PAC and Azad RS (1973) Turbulence in a conical diffuser with fully developed flow at entry. *Journal of Fluid Mechanics* 57: 603-622.
- Oshkai P (2002) Flow-acoustic coupling in a cavity-pipeline system. Lehigh University, Bethlehem, PA, USA. PhD thesis.
- Oshkai P and Yan T (2008). *Experimental Investigation of Coaxial Side Branch Resonators*. ASME Pressure Vessels and Piping Division, Vancouver, BC, Canada.
- Oshkai P, Yan T, Velikorodny A, et al. (2008) Acoustic Power Calculation in Deep Cavity Flows. *Journal of Fluids Engineering* 130(051203-1).
- Parker R and Welsh MC (1983) Effects of sound on flow separation from blunt flat plates. *International Journal of Heat and Fluid Flow* 4: 113-127.
- Pope SB (2000). Turbulent flows, Cambridge University Press.
- Powel A (1964) Theory of Vortex Sound. *Acoustic Society of America* 36: 177-195.
- Raffel M, Willert C, Wereley ST, et al. (2007). Particle Image Velocimetry. A practical guide, Springer.

- Rockwell D and Knisely C (1980) Observations of the three-dimensional nature of unstable flow past a cavity. *Phys. Fluids* 23: 425–431.
- Rockwell D, Lin J-C, Oshkai P, et al. (2003) Shallow Cavity Flow Tone Experiments: Onset of Locked-On States. *Journal of Fluids and Structures* 17(3): 381-414.
- Rockwell D and Naudascher E (1979) Self-sustained oscillations of impinging free shear layers. *Annual Reviews of Fluid Mechanics*(11): 67-94.
- Rossiter JE (1964) Wind-Tunnel Experiments on the Flow over Rectangular Cavities at Subsonic and Transonic Speeds. *Aerodyn Res Coun Rep Memo* 3438
- Saathoff PJ and Melbourne WH (1997) Effects of free stream turbulence on surface pressure fluctuations in a separated bubble. *Journal of Fluid Mechanics* 337: 1-24.
- Saric WS (1994) Görtler vortices. *Annual Reviews of Fluid Mechanics* 26: 379-409.
- Sarohia V (1977) Experimental investigations of oscillations in flows over shallow cavities. *AIAA* 15(7): 984-991.
- Scarano F and Poelma C (2009) Three-dimensional vorticity patterns of cylinder wakes. *Experiments in Fluids* 47: 69-83.
- Schlichting H and Gersten K (2000). Boundary Layer Theory, Springer.
- Sigurdson LW (1995) The structure and control of a turbulent reattaching flow. *Journal of Fluid Mechanics* 298: 139–165.
- Stokes AN and Welsh MC (1986) Flow-Resonant Sound Interaction in a Duct Containing a Plate .2. Square Leading-Edge. *Journal of Sound and Vibration* 104(1): 55-73.
- Suksangpanomrung A, Djilali N and Moinat P (2000) Large eddy simulation of separated flows over a bluff plate. *International Journal of Heat and Fluid Flow* 21: 655-663.
- Tafti DK and Vanka SP (1991) A three-dimensional numerical study of flow separation and reattachment. *Physics of Fluids* 3(12): 2887-2909.
- Velikorodny A, Yan T, and Oshkai P, Effect Of Junction Geometry On Acoustic Response Of Side Branch Resonators, 9th International Conference On Flow-Induced Vibrations (FIV 2008), pp. 767- 772, Prague, June 30 - July 3, 2008.
- Velikorodny A, Yan T and Oshkai P (2009a) Quantitative imaging of acoustically-coupled flows. *Experiments in Fluids* doi: 10.1007/s00348-009-0731-5.

- Velikorodny A, Duck G, and Oshkai P (2009b) Experimental Investigation of Flow over a Backward-Facing Step in Proximity to a Flexible Wall. Experiments in Fluids, submitted
- Welsh PD (1967) The Use of Fast Fourier Transform for the Estimation of Power Spectra: A Method Based on Time Averaging Over Short, Modified Periodograms. IEEE Transactions on audio electroacoustics 15: 70-73.
- Westerweel J (1997) Fundamentals of digital particle image velocimetry. Measurement Science & Technology 8(12): 1379-1392.
- Willert C (1996) The fully digital evaluation of photographic PIV recordings. Applied Scientific Research 56(2-3): 79-102.
- Willert CE and Gharib M (1991) Digital Particle Image Velocimetry. Experiments in Fluids 10(4): 181-193.
- Wu X, Schluter J, Moin P, et al. (2006) Computational study on the internal layer in a diffuser. Journal of Fluid Mechanics 550: 391-412.
- Wyganski I and Fiedler H (1970) The two-dimensional mixing region. Journal of Fluid Mechanics 41: 327-361.
- Yan T (2006). Investigation of Acoustically-coupled Shear Layers Using Particle Image Velocimetry. Mechanical Engineering. Victoria, University of Victoria. M.Sc.
- Yang Y, Rockwell D, Cody KLF, et al. (2009) Generation of tones due to flow past a deep cavity: Effect of streamwise length. Journal of Fluids and Structures 25(2): 364-388.
- Ziada S (1994) A Flow Visualization Study of Flow-Acoustic Coupling at the Mouth of a Resonant Side-Branch. Journal of Fluids and Structures 8(4): 391-416.
- Ziada S (2000) Interaction of a jet-slot oscillator with a deep cavity resonator and its control. Journal of Fluids and Structures(15): 831-843.
- Ziada S (2003) Control of Fluid-Structure-Sound Interaction Mechanisms by Means of Synthetic Jets. JSME International Journal 46(3): 873-880.
- Ziada S and Buhlmann ET (1992) Self-Excited Resonances of 2 Side-Branched in Close Proximity. Journal of Fluids and Structures 6(5): 583-601.
- Ziada S and S. Shine (1999) Strouhal numbers of flow-excited acoustic resonance of closed side branches. Journal of Fluids and Structures(13): 127-142.

## APPENDIX A: SOUND

### Extended from Landau and Lifshitz (1987) and Kinsler et al. (2000)

An oscillatory motion with small amplitude in a compressible fluid is called a sound wave. At each point in the fluid, a sound wave causes alternate compression and rarefaction. Since the oscillations are small, the velocity  $v$  is small also, so that the term  $(\bar{v} \cdot \bar{\nabla})\bar{v}$  in Euler's equation may be neglected. For the same reason, the relative changes in the fluid density and pressure are small. We can write the variables  $p$  and  $\rho$  in the form:

$$p = p_0 + p', \rho = \rho_0 + \rho', \quad (\text{A1})$$

where  $\rho_0$  and  $p_0$  are the constant equilibrium density and pressure, and  $\rho'$  and  $p'$  are their variations in the sound wave ( $\rho' \ll \rho_0, p' \ll p_0$ ). The equation of continuity  $\frac{\partial \rho}{\partial t} + \text{div}(\rho v) = 0$ , on substituting in (A1) and neglecting small terms of the second order ( $\rho', p'$  and  $v$  are of the first order), becomes:

$$\frac{\partial \rho'}{\partial t} + \rho_0 \text{div}(v) = 0 \quad (\text{A2})$$

While Euler's equation

$$\frac{\partial v}{\partial t} + (v \cdot \text{grad})v = -\frac{1}{\rho} \text{grad}(p)$$

reduces, in the same approximation, to

$$\frac{\partial v}{\partial t} + \frac{1}{\rho_0} \text{grad}(p') = 0 \quad (\text{A3})$$

The condition that the linearized equations of motion (A2) and (A3) should be applicable to the propagation of sound waves is that the velocity of the fluid particles in the wave should be small compared with the velocity of sound:  $v \ll c$ . This condition can be obtained, for example, from the requirement that  $\rho' \ll \rho_0$  (see A16)

Equations (A2) and (A3) contain unknown functions. To eliminate one of these, we notice that a sound wave in an ideal fluid is, like any other motion in an ideal fluid, adiabatic. Hence the small change  $p'$  in the pressure is related to the small change  $\rho'$  in the density by:

$$p' = \left( \frac{\partial p}{\partial \rho_0} \right)_s \rho' \quad (\text{A4})$$

Substituting for  $\rho'$  according to this equation in (A1.2), we have:

$$\frac{\partial p'}{\partial t} + \rho_0 \left( \frac{\partial p}{\partial \rho_0} \right)_s \text{div}(v) = 0 \quad (\text{A5})$$

The two equations (A3) and (A5), with the unknowns  $v$  and  $p'$ , give a complete description of the sound wave. In order to express all the variables in terms of one of them, it is convenient to introduce the velocity potential by putting  $v = \bar{\nabla}(\varphi)$ . From (A3) we have:

$$p' = -\rho \frac{\partial \varphi}{\partial t}, \quad (\text{A6})$$

which relates  $p'$  and  $\varphi$ . From (1.5) we further obtain:

$$\frac{\partial^2 \varphi}{\partial t^2} - c^2 \Delta \varphi = 0, \quad (\text{A7})$$

which the potential must satisfy; here the notation:  $c = \sqrt{\left(\frac{\partial p}{\partial \rho_0}\right)_s}$  was introduced, and

$\Delta$  is a Laplace operator.

An equation (A7) is called a wave equation. Applying the gradient operator to (A7), it can be found that each of the three components of the velocity satisfies an equation having the same form, and on differentiating (A7) with respect to time we see that the pressure  $p'$  (and therefore  $\rho'$ ) also satisfies the wave equation.

Let's consider equation (A1.7) in 1D case. The flow in this scenario is completely homogeneous in the  $yz$ -plane. Such a wave is called a plane wave. The equation (A7) becomes

$$\frac{1}{c^2} \frac{\partial^2 \varphi}{\partial t^2} - \frac{\partial^2 \varphi}{\partial x^2} = 0 \quad (\text{A8})$$

To solve this equation, we replace  $x$  and  $t$  by new variables  $\zeta = x - ct, \eta = x + ct$ . It

is easy to see that in these variables (A1.8) becomes  $\frac{\partial^2 \varphi}{\partial \eta \partial \zeta} = 0$ . Integrating this

equation with respect to  $\zeta$  we find  $\frac{\partial \varphi}{\partial \eta} = F(\eta)$ , where  $F(\eta)$  is an arbitrary function of

$\eta$ . Integrating again, we obtain  $\varphi = f_1(\zeta) + f_2(\eta)$ , where  $f_1$  and  $f_2$  are arbitrary functions of their arguments. Thus

$$\varphi = f_1(x - ct) + f_2(x + ct) \quad (\text{A9})$$

The distribution of the other quantities ( $p', \rho', v$ ) in a plane wave is given in the same form.

To be consistent, the pressure term should be discussed as well. For example, if  $f_2 = 0$ ,  $\Rightarrow p = f_1(x - ct)$ . The meaning of this solution is as follows: in any plane

$x = \text{const}$  the pressure varies with time, and at any given time it is different for different  $x$ . But it is the same for coordinates  $x$  and times  $t$  such that  $x - ct = \text{const}$ , or  $x = \text{const} + ct$ . The latter means that, if at some instant  $t = 0$  and at some point the fluid pressure has a certain value, then after a time  $t$  the same value of the pressure is found at a distance  $ct$  along x-axis from the original point. The same is true of all the other quantities in the wave. Thus the pattern of motion is propagated through the medium in the x-direction with a velocity  $c$  - speed of sound.

Thus  $f_1(x - ct)$  represents the so called traveling plane wave propagated in the positive direction of the x-axis. It is evident that  $f_2(x + ct)$  gives a wave propagated in the opposite direction. Of the three components of the velocity in a plane wave, only  $v_x = \frac{\partial \varphi}{\partial x}$  is non zero. Thus the fluid velocity in a sound wave is in the direction of propagation. For this reason sound waves in a fluid are said to be longitudinal.

In a traveling plane wave, the velocity is related to the pressure and density in a simple manner. After putting  $\varphi = f(x - ct)$ , we have  $v = \frac{\partial \varphi}{\partial x} = f'(x - ct)$ , also from (A6) one can see that  $p' = -\rho \frac{\partial \varphi}{\partial t} = \rho c f'(x - ct)$ . Comparing the two expressions, we find that:

$$v = \frac{p'}{\rho c} \quad (\text{A10})$$

Upon substitution of (A1.4) into it, we arrive to the relation between velocity and the density variation:

$$v = \frac{c \rho'}{\rho} \quad (\text{A11})$$

## APPENDIX B: VORTEX SOUND THEORY

### From Blake (1986) and Howe (2003)

While relationship between vortices and sound production was understood long ago, a formal theory and the vortex sound equation were established by Powell (1964). He showed that for a low Mach number compact flow in free space Lighthill's sound source can be defined as follows:  $Q_s = \text{div}(f_s) = \text{div}(\rho_0 \bar{\omega} \times \bar{u})$ , where  $\bar{u}$  – fluid with velocity and  $\bar{\omega}$  – vorticity. Powel (1964) considered the generation of fluid disturbances by the motion of an isolated vortex ring. He showed that pressure perturbation is proportional to the change in the rate of vortex stretching by the fluid, confirming the name “vortex sound” to the far-field sound radiation.

$$p(\bar{x}, t) = -\frac{\rho_0}{4\pi c_0} \frac{x_j}{|\bar{x}|^2} \frac{\partial}{\partial t} \iiint_V (\bar{\omega} \times \bar{u}) dV \quad (\text{A12})$$

It should be also noted that the integrand in (A12) is recognized as the forcing term in the Acoustic Power Integral (Appendix C).

Howe (1975) has reformulated Powel's and Lighthill's results to deal with situations where there exists a non-uniform nonisentropic mean flow. He defined source of sound not relative to a uniform fluid, but with respect to a potential flow.

Instead of pressure, the total enthalpy  $\left( B = \int \frac{dp}{\rho} + v^2/2 \right)$  appeared to be a natural variable for this case. If the mean flow is at rest in the far field the acoustic pressure

given by:  $p = -\rho_0 \frac{\partial \varphi}{\partial t}$  (A6), where  $\varphi$  is a scalar potential that defines motion of the irrotational fluid.

The fluid motion satisfies Crocco's form of the momentum equation (Batchelor 1967):

$$\frac{\partial \bar{v}}{\partial t} + \bar{\omega} \times \bar{v} + \nabla B = -\nu \bar{\nabla} \times \omega, \quad (\text{A13})$$

where  $B$  is the total enthalpy and vorticity  $\bar{\omega} = \bar{\nabla} \times v$ , and  $S = \text{const}$  for simplicity.

Multiplying this equation by  $\rho$  and applying the divergence to all terms, Howe (2003) obtained vortex sound equation, where  $\text{div}(\rho \bar{\omega} \times \bar{v})$  is identified as the principal source of sound:

$$\left( \frac{D}{Dt} \left( \frac{1}{c^2} \frac{D}{Dt} \right) - \frac{1}{\rho} \bar{\nabla} \cdot (\rho \bar{\nabla}) \right) B = \frac{1}{\rho} \text{div}(\rho \bar{\omega} \times \bar{v}) \quad (\text{A14})$$

When the characteristic Mach number is small, first  $\rho$  and  $c$  can be approximated with their values in the far field:  $\rho \sim \rho_0 (1 + O(M^2))$ , second the nonlinear effects of propagation and scattering of sound can be neglected. Thus, the modified vortex sound equation is defined by:

$$\left( \frac{1}{c_0^2} \frac{\partial}{\partial t} - \Delta \right) B = \text{div}(\bar{\omega} \times \bar{v}) \quad (\text{A15})$$

## APPENDIX C: DERIVATION OF THE ACOUSTIC POWER INTEGRAL

In an unbounded fluid velocity can be always expressed in terms of scalar and vector potentials (e.g. Batchelor 1967).

$$\bar{v} = \bar{\nabla}\varphi + \bar{\nabla} \times \bar{A}, \quad (\text{A16})$$

where  $\bar{\nabla} \cdot \bar{A} = 0$  – represents solenoidal, rotational part of the velocity, which is induced by vorticity, and  $\bar{\nabla}\varphi$  – irrotational part. If one further assumes the fulfilment of the linear assumption of the conventional wave equation, the acoustical velocity  $u_{ac}$  in the eqn. (A16) framework can be defined as an unsteady irrotational part of the velocity field  $\bar{v}$  (Appendix A).

Thus let's assign:  $\bar{u}_{ac} = \bar{\nabla}\varphi$  and  $\bar{u} = \bar{\nabla} \times \bar{A}$  (note:  $\bar{\nabla} \cdot \bar{u} = 0$ , and  $\varphi$  describes compressibility motions)  $\Rightarrow$

$$\bar{v} = \bar{u} + \bar{u}_{ac} \quad (\text{A17})$$

Crocco's equation (A13) with inviscid flow assumption reads:

$$\frac{\partial \bar{u}}{\partial t} + \bar{\nabla} B + \bar{\nabla} \frac{\partial \varphi}{\partial t} = -\bar{\omega} \times \bar{u} - \bar{\omega} \times \bar{u}_{ac} \quad (\text{A18})$$

Taking scalar product of this equation with  $\bar{u}$ , and integrating over the volume of a large sphere whose radius is allowed to increase without limit we have:

$$\iiint_V \frac{\partial}{\partial t} \left( \frac{1}{2} |\bar{u}|^2 \right) dV + \iiint_V \bar{\nabla} B \cdot \bar{u} dV + \iiint_V \bar{\nabla} \frac{\partial \varphi}{\partial t} \cdot \bar{u} dV = \iiint_V (\bar{\omega} \times \bar{u}) \cdot \bar{u}_{ac} dV \quad (\text{A19})$$

Lets name these integrals by the order of their appearance to get:  $I_1 + I_2 + I_3 = -I_4$ .

Application of partial integration to  $I_2$  results in:

$$I_2 = \iiint_V \bar{\nabla} B \cdot \bar{u} dV = \iiint_{\partial V} B \bar{u} \cdot \bar{n} dS - \iiint_V B \bar{\nabla} \cdot \bar{u} dV \quad (\text{A20})$$

where  $\bar{n}$  is an outward pointing normal of the boundary of the volume  $V$ . It can be noticed that second integral is equal to zero (see definition (A16):  $\bar{\nabla} \cdot \bar{u} = 0$ ). First integral vanishes upon choosing appropriate boundaries of the integration domain, so that  $\bar{u} \cdot \bar{n} = 0$ . Thus,  $I_2 = 0$ .

Partial integration works for  $I_3$  as well, resulting in:

$$I_3 = \iiint_V \bar{\nabla} \frac{\partial \varphi}{\partial t} \cdot \bar{u} dV = \iiint_{\partial V} \frac{\partial \varphi}{\partial t} \bar{u} \cdot \bar{n} dS - \iiint_V \frac{\partial \varphi}{\partial t} \bar{\nabla} \cdot \bar{u} dV \quad (\text{A21})$$

$I_3$  equals zero by the same rules as it was for  $I_2$ . Now, we can sub (A20) and (A21) into (A19) and multiply both sides with  $\rho_0$  to get:

$$\rho_0 \frac{\partial}{\partial t} \iiint_V \left( \frac{1}{2} |\bar{u}|^2 \right) dV = \rho_0 \iiint_V (\bar{\omega} \times \bar{u}) \cdot \bar{u}_{ac} dV \quad (\text{A22})$$

The left hand side of the equation is determined how much kinetic energy is supplied to the field by the vorticity-bearing part of the velocity field. Right hand side represents the rate at which acoustic energy is being absorbed or produced by the vortical field.

In order to conveniently define the direction of the flow of acoustic energy both sides of Eqn. A(22) were multiplied by -1.

Designating  $P_w(t) = -\rho_0 \frac{\partial}{\partial t} \iiint_V \left( \frac{1}{2} |\bar{u}|^2 \right) dV$ , (A22) takes the form of the acoustic power described by equation (1.10) in Section 1.3.4.

**APPENDIX D: AIR CLAMP STAGE AND PAPER SHEET ASSEMBLY**

**DETAIL B  
SCALE 1 : 1**

**NOTES:**  
 1. ASSEMBLY AS SHOWN WITH 6in PAPER STRIP AND 8 TMF TENSIONING WEIGHT.  
 2. TOTAL WEIGHT REQUIRED TO ACHIEVE A 1.12 Nm [100Nm] LINEAL SHEET TENSION LOAD.  
 6in SHEET STRIP - 8 TMF  
 3in PAPER STRIP - 3.28MF  
 REMOVE WEIGHT AS REQUIRED TO ACHIEVE CORRECT LOAD CONDITIONS.  
 3. ASSEMBLY AS SHOWN INCLUDES LASER CALIPER DOME AND AIRCLAMP. TO MOUNT AIRCLAMP ONLY REMOVE ITEMS 6, 10, 12, 13, 28 & 29, AND ADD ITEMS 40, 41, 43 & 44. SEE SHEET 202.

30	1	IN	SCREW 4-40 X 1/2 PAN H/TSS	88888001
40	1	IN	AIR CLAMP SPACER 8x12 3mm	88888020
41	1	IN	SCREW 4-40 X 1/2 PAN H/TSS	88888001
42	2	IN	AIR CLAMP BRACE #	88888020
43	1	IN	SCREW 4-40 X 1/2 PAN H/TSS	88888001
44	1	IN	SCREW 4-40 X 1/2 PAN H/TSS	88888001
45	1	IN	SCREW 4-40 X 1/2 PAN H/TSS	88888001
46	1	IN	SCREW 4-40 X 1/2 PAN H/TSS	88888001
47	1	IN	SCREW 4-40 X 1/2 PAN H/TSS	88888001
48	1	IN	SCREW 4-40 X 1/2 PAN H/TSS	88888001
49	1	IN	SCREW 4-40 X 1/2 PAN H/TSS	88888001
50	1	IN	SCREW 4-40 X 1/2 PAN H/TSS	88888001
51	1	IN	SCREW 4-40 X 1/2 PAN H/TSS	88888001
52	1	IN	SCREW 4-40 X 1/2 PAN H/TSS	88888001
53	1	IN	SCREW 4-40 X 1/2 PAN H/TSS	88888001
54	1	IN	SCREW 4-40 X 1/2 PAN H/TSS	88888001
55	1	IN	SCREW 4-40 X 1/2 PAN H/TSS	88888001
56	1	IN	SCREW 4-40 X 1/2 PAN H/TSS	88888001
57	1	IN	SCREW 4-40 X 1/2 PAN H/TSS	88888001
58	1	IN	SCREW 4-40 X 1/2 PAN H/TSS	88888001
59	1	IN	SCREW 4-40 X 1/2 PAN H/TSS	88888001
60	1	IN	SCREW 4-40 X 1/2 PAN H/TSS	88888001
61	1	IN	SCREW 4-40 X 1/2 PAN H/TSS	88888001
62	1	IN	SCREW 4-40 X 1/2 PAN H/TSS	88888001
63	1	IN	SCREW 4-40 X 1/2 PAN H/TSS	88888001
64	1	IN	SCREW 4-40 X 1/2 PAN H/TSS	88888001
65	1	IN	SCREW 4-40 X 1/2 PAN H/TSS	88888001
66	1	IN	SCREW 4-40 X 1/2 PAN H/TSS	88888001
67	1	IN	SCREW 4-40 X 1/2 PAN H/TSS	88888001
68	1	IN	SCREW 4-40 X 1/2 PAN H/TSS	88888001
69	1	IN	SCREW 4-40 X 1/2 PAN H/TSS	88888001
70	1	IN	SCREW 4-40 X 1/2 PAN H/TSS	88888001
71	1	IN	SCREW 4-40 X 1/2 PAN H/TSS	88888001
72	1	IN	SCREW 4-40 X 1/2 PAN H/TSS	88888001
73	1	IN	SCREW 4-40 X 1/2 PAN H/TSS	88888001
74	1	IN	SCREW 4-40 X 1/2 PAN H/TSS	88888001
75	1	IN	SCREW 4-40 X 1/2 PAN H/TSS	88888001
76	1	IN	SCREW 4-40 X 1/2 PAN H/TSS	88888001
77	1	IN	SCREW 4-40 X 1/2 PAN H/TSS	88888001
78	1	IN	SCREW 4-40 X 1/2 PAN H/TSS	88888001
79	1	IN	SCREW 4-40 X 1/2 PAN H/TSS	88888001
80	1	IN	SCREW 4-40 X 1/2 PAN H/TSS	88888001
81	1	IN	SCREW 4-40 X 1/2 PAN H/TSS	88888001
82	1	IN	SCREW 4-40 X 1/2 PAN H/TSS	88888001
83	1	IN	SCREW 4-40 X 1/2 PAN H/TSS	88888001
84	1	IN	SCREW 4-40 X 1/2 PAN H/TSS	88888001
85	1	IN	SCREW 4-40 X 1/2 PAN H/TSS	88888001
86	1	IN	SCREW 4-40 X 1/2 PAN H/TSS	88888001
87	1	IN	SCREW 4-40 X 1/2 PAN H/TSS	88888001
88	1	IN	SCREW 4-40 X 1/2 PAN H/TSS	88888001
89	1	IN	SCREW 4-40 X 1/2 PAN H/TSS	88888001
90	1	IN	SCREW 4-40 X 1/2 PAN H/TSS	88888001
91	1	IN	SCREW 4-40 X 1/2 PAN H/TSS	88888001
92	1	IN	SCREW 4-40 X 1/2 PAN H/TSS	88888001
93	1	IN	SCREW 4-40 X 1/2 PAN H/TSS	88888001
94	1	IN	SCREW 4-40 X 1/2 PAN H/TSS	88888001
95	1	IN	SCREW 4-40 X 1/2 PAN H/TSS	88888001
96	1	IN	SCREW 4-40 X 1/2 PAN H/TSS	88888001
97	1	IN	SCREW 4-40 X 1/2 PAN H/TSS	88888001
98	1	IN	SCREW 4-40 X 1/2 PAN H/TSS	88888001
99	1	IN	SCREW 4-40 X 1/2 PAN H/TSS	88888001
100	1	IN	SCREW 4-40 X 1/2 PAN H/TSS	88888001

**Honeywell**  
 LASER CALIPER  
 PAPER TENSIONING ASSEMBLY  
 AIR CLAMP PAPER TENSIONING FUTURE  
 V06078 R00004  
 659990100 DD DE 0

**DETAIL E  
SCALE 1 : 1**

**DETAIL D  
SCALE 1 : 1**

**NOTES:**  
 1. ASSEMBLY AS SHOWN INCLUDES LASER CALIPER DOME AND AIRCLAMP. TO MOUNT AIRCLAMP ONLY REMOVE ITEMS 6, 10, 12, 13, 28 & 29, AND ADD ITEMS 40, 41, 43 & 44. SEE SHEET 202.

**Honeywell**  
 LASER CALIPER  
 PAPER TENSIONING ASSEMBLY  
 AIR CLAMP PAPER TENSIONING FUTURE  
 V06078 R00004  
 659990100 DD DE 0

## **APPENDIX E: AIR CLAMP EXPERIMENTAL ISSUES AND CONSTRAINTS**

The ranges of parameters for air clamp experiments specified in Chapter 2 were chosen on the basis of the set of preliminary experiments. The experimental challenges and constraints are summarized and commented below:

### **1. Strong Reflections**

#### **1.1 From the stainless steel surface**

#### **1.2 From the paper**

### **2. Out-of-plane particles in the field of view**

### **3. Oil accumulation at the nozzle**

### **4. Limitations associated with:**

#### **4.1 Spatial resolution**

#### **4.2 Velocities to be measured**

Some of the issues have been successfully resolved, while others constitute inherent limitations of the experimental technique. Being more specific, constraint 1.1 was resolved by introducing fluorescent paint, which is a typically employed to measure a flow field with PIV close to walls. The intensities of the reflections in this scenario are much higher than the particle signal. In order to avoid saturation of the CCD if higher laser powers were used it is recommended to use fluorescent paint. This paint turns some amount of the emitted green light into the red light, which is subsequently blocked by green bandpass filter (a 532 nm wavelength filter with a bandwidth of 10 nm was employed).

Constraint 2 is very much similar to the conventional microPIV, where volume illumination results in high levels of background noise from out-of-focus particles.

Proper f-number of the camera lens has to be implemented for each experiment together with precise focusing. Moreover, large volumes of data have to be averaged, which would, ideally, lead to longer trials of data. In the considered case, however, because oil rapidly accumulates at the nozzle (Constraint 3), forming oil drops in the vicinity of the step, experimental data becomes unreliable.

Constraint 4 represents fundamental limitation of any PIV system. In order to properly compare experimental results with an FSI model, one usually has to resolve rather large field of view to satisfy an outflow condition. In this study the largest FOV was 25 x 18.9 mm. In fact, the choice of the velocity and SR to be measured is a crucial factor when appropriate FOV is identified. First of all, the back pressure that is needed to actually clamp the paper for various  $H$  values has been found. These numbers were later translated to the mean velocities at the edge of the step. Throughout this preliminary experimentation process FOV and interrogation window sizes, as well as  $\Delta t$  (time delay between two laser pulses) values have been adjusted. The procedure has been finally resulted in formulation of the parameters specified in previous sections.

## APPENDIX F: RECOMMEDATIONS FOR AIR CLAMP APPLICATION

It is important to develop passive methods to control gross flow separation from the surface of the paper sheet in order to achieve flatness of the profile.

Figure A.1 compares the time-averaged position of the paper sheet obtained from the present ( $U = 120\text{m/s}$ ) and industrial experiments. The difference in the profiles is due to realistic regime of operation of the air clamp device in the Honeywell experiments, where a width of the paper-sheet is order of magnitude greater than in the present case and it moves with the velocity of up to 28 m/s. Moreover, jet speeds used in Honeywell experiments were up to 1 Mach.

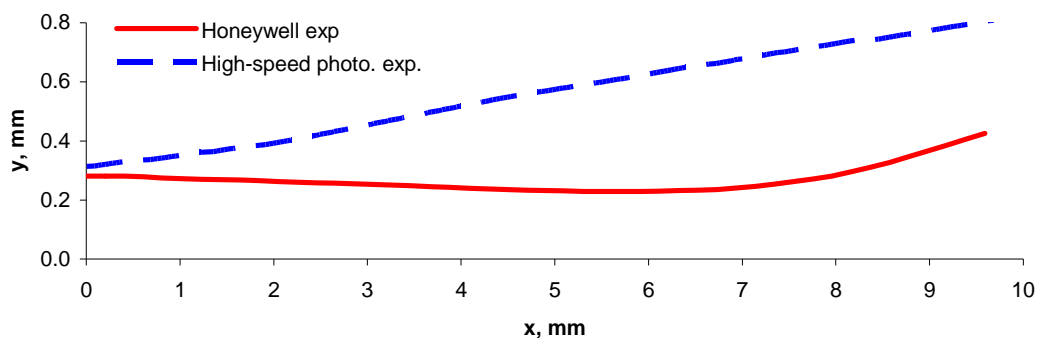


**Fig. A.1** Time-averaged paper sheet profiles from Honeywell and high-speed photography (present) experiments

The Honeywell paper sheet experiences a negative slope up to about 6.5 mm, which is consistent with the location of the reattachment point on the bottom surface of the air clamp. In that region significant pressure increase leads to the consequent gross flow separation from the surface of the paper sheet and a sudden increase in the slope. The following passive control measures can be exploited:

- a) To reduce pressure and increase kinetic energy in the flow, suction can be utilized either from the surface or from the downstream section of

the air clamp. The schematic of Fig. A.2 shows some possible details. The suction ports would be extended in the spanwise direction as well. The spacing between ports as well their dimensions have to be determined experimentally.

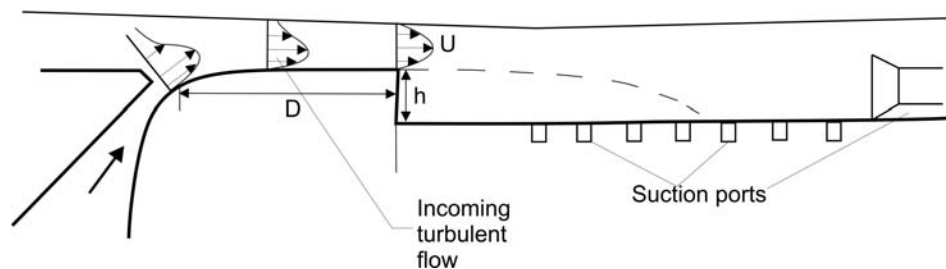


**Fig. A.2** Schematic of the air clamp with suction ports

- b) A more neat set of experiments might be performed by increasing velocity of the paper sheet (or/and decrease jet speed) to be comparable with a speed of the jet in order to mitigate cause of the boundary layer formation.
- c) The previous point can be exploited together with modification of the air clamp geometry corresponding to the absence of the BFS.

In addition, it is recommended to develop a theoretical expression for the flow-induced forcing term that can be subsequently applied for calculation of the shape of the paper sheet subject to an arbitrary set of boundary conditions. The goal of that study is to extend the present experimental results to a realistic regime of operation of the air clamp device.

In particular, the shape of the paper sheet that is subject to arbitrary boundary conditions can be determined from purely geometric arguments if the maximum

displacement of the paper sheet from its initial position (corresponding to the absence of the flow) is known. The known profile of the paper sheet can be subsequently incorporated into a correction factor for measurements of the paper properties in the industrial setting. In other words, it is suggested that the fluid-structure interactions in the air clamp are effectively represented by the maximum paper displacement. This suggestion is based on the assumption (supported by the present results) of a compact forcing region, which is located in the vicinity of the BFS and upstream of the flow separation from the paper sheet.

## APPENDIX G: SOME MATLAB CODES

### SIDE BRANCH RESONATOR PROJECT

#### a) Q-factor

```

% Q_factor calculation for 5mm plate

t = cputime;
q=zeros(33,1);
A=[0.5:0.125:4.5];

u=[3 5.5 8 10.5 13 16 19.25 21.38 23.57 25 25.87 26.9 28 29.93 31.351
32.765 34.178 35.592 37 38.42 39.834 41.248 42.662 44.07...
45.49 46.9 48.31 49.732 51.146 52.56 53.97 55.387 56.8];
ui=[3 4.25 5.5 6.75 8 9.25 10.5 11.75 13 14.5 16 17.625 19.25 20.315
21.38 22.475 23.57 24.285 25 25.435 25.87 26.385 26.9 27.45 28
28.96...
29.93 30.64 31.35 32.05 32.765 33.47 34.17 34.885 35.592 36.29 37
37.71 38.42 39.127 39.83 40.54 41.24 41.95 42.6 43.36 44.07 44.783...
45.49 46.19 46.9 47.61 48.31 49.025 49.73 50.439 51.146 51.853 52.56
53.26 53.97 54.68 55.38 56.09 56.8];

for j=1:33
    k=A(j);
    %clear velspec
        identvelspec=sprintf('Data_%g',k);
        %velspec = sprintf('j:\\Ting\\Labview Data\\FSC velocity
sweep\\%s.txt',identvelspec);
        velspec = sprintf('C:\\Documents and Settings\\asv\\My
Documents\\Matlab\\thesis\\plates\\5mm\\velocity_sweep\\%s.dat',ide
ntvelspec); %determines location to save combined data
        data=textread(velspec, '-1'); %loads the data file under
velocity
        eval(['clear ', identvelspec]);
x = data(:,1);

fs = 8192; %sampling rate that data was taken at.
NFFT = 2^nextpow2(x); % Next power of 2 from length of x

% Take fft, padding with zeros, length(FFTX)==NFFT
FFTX=fft(x,NFFT);
UniquePts = ceil((NFFT+1)/2);

% fft is symmetric, get rid of second half
FFTX=FFTX(1:UniquePts);

Px=abs(FFTX)/length(x); % Magnitude of X and scale.

% Multiply by 2 to take into account the fact that we threw out
second half of FFTX above
Px=Px*2;
Px(1)=0;
f=(0:UniquePts-1)*fs/NFFT;

```

```

%%%%%%%%Q_factor%%%%%%%%%%

%% Initial data
n = length(f);
%f = velspecdata(:,1);
%u(j) = velspecdata(2,2);
p = (Px*6894.75).^2; % For power spectra
m = max(p(100:n))/2;

%% Find max index and f0
for i=100:n
    if p(i)==max(p(100:n))
        fmax=f(i);
        z=i;
        break
    end
end

%% Cut pressure and freq. signals around max
pp=p(z-50:z+50);
ff=f(z-50:z+50);
ff=ff';

%% Interpolate
step=0.05;
l=0.5/step;
fi = (ff(1):step:ff(101))';
pi = interplq(ff,pp,fi);

%% Find frequencies f1 and f2

% First external point
for i=2:100*(l/2)+1
    if pi(i)>m
        f1 = fi(i-1);
        f2 = fi(i);
        break
    end
end
fle=(f1+f2)/2;

%First internal point
for i=100*(l/2)+1:-1:1
    if pi(i)<m
        f1 = fi(i-1);
        f2 = fi(i);
        break
    end
end
fli=(f1+f2)/2;

%Second internal point
for i=100*(l/2)+1:100*l+1
    if pi(i)<m
        f1 = fi(i-1);

```

```

        f2 = fi(i);
        break
    end
end
end
f2i=(f1+f2)/2;

%Second external point
for i=100*l+1:-1:100*(l/2)+1
    if pi(i)>m
        f1 = fi(i-1);
        f2 = fi(i);
        break
    end
end
f2e=(f1+f2)/2;

f1=(f1e+f1i)/2;
f2=(f2i+f2e)/2;

%% Calculate Q-factor
delta(j)=f2-f1;
q(j) = fmax/delta(j);
end

e = cputime-t;
stem(u,q)

```

### ***b) Phase-averaging procedure***

```

% pseudocycle.m
% Finds correspondence between PIV frames (Q-switch) and phases from
the
% reference signal

%% Initialize
A=zeros(10,1800);
x=DATA_1000_5s(24976:end,1);
t=tx(24976:end);
%G=zeros(40200,1);
sp=spline(t,x);
ts=t(1):1/65536:t(end);

x=ppval(sp,ts);
t=ts;

%pint = 1.098632812500000e-04;
%tQ=t(1):1/1000:t(end);
tQ=Q(:,2); % from Q-switch time trace
k=1;

for i=2:1800 % start

%% Find closest point(t0) to tQ within t
    Dif = abs(t-tQ(i));
    M = min(Dif);

```

```

for r=1:length(Dif)
    if Dif(r)==M;
        p=r;
    end
end
t0 = t(p);
%% In the interval [t0-11,t0+11] find max values t1 and t11
int = 70;
if p<int
    int=p-1;
end

M=0;
for r=p-int:p
    if x(r)>M
        M=x(r);
        p1=r;
    end
end
t1=t(p1);

M=0;
for r=p:p+int
    if (r~=p1) && (x(r)>M)
        M=x(r);
        p2=r;
    end
end
t11=t(p2);

% If three values were found take two first
M=0;
if (p1>p) && (p2>p)
    for r=p-int:p+int
        if (r~=p1) && (r~=p2) && (x(r)>M)
            M=x(r);
            p3=r;
        end
    end
    p1=p3;
    t1=t(p3);
end

%% Phase interval = (t11-t1)/11, phases are identified starting from
t1
pint = abs((t11-t1))/11;
if t1>t11
    tt=t11;
else
    tt=t1;
end
for j=1:10
    if ((j-1)*pint+tt<tQ(i)) && (tQ(i)<j*pint+tt)
        A(j,k)=i;
    end
end
k=k+1;

```

```

end % EOF

% Calculates phase-averaged velocity & vorticity plots
% Uses Matrix A from pseudocycle.m

%% Initialize
velocity = zeros(16384,4);
vorticity = zeros(16384,3);
velvort = zeros(16384,6);
z=zeros(10,1); % # of frames to average
A=AA_1800;

%% main
for i=1:10

    for j=1:1800-1
        if A(i,j)~=0
            z(i,1)=z(i,1)+1;
            k=A(i,j);

            % first file
            if k<=9
                ident=sprintf('B0000%g',k);
            elseif k<=99
                ident=sprintf('B000%g',k);
            elseif (k>=100) && (k<=999)
                ident=sprintf('B00%g',k);
            else
                ident=sprintf('B0%g',k);
            end
            svel=sprintf('h:\\splitter
plates\\5mm\\1000Hz_5mode_3s\\exported_new\\velocity\\%s.dat',ident);
%adds the location information to filename
            svor=sprintf('h:\\splitter
plates\\5mm\\1000Hz_5mode_3s\\exported_new\\vorticity\\%s.dat',ident)
; %adds the location information to filename
            velocity1=textread(svel, '',-1,'headerlines',3); %loads the
data file under velocity
            vorticity1=textread(svor, '',-1,'headerlines',3); %loads the
data file under vorticity
            % phase-averaged velocity and vorticity
            velocity(:,3) = velocity(:,3) + velocity1(:,3);
            velocity(:,4) = velocity(:,4) + velocity1(:,4);
            vorticity(:,3) = vorticity(:,3) + vorticity1(:,3);
            end
        end
        velocity(:,1) = velocity1(:,1);
        velocity(:,2) = velocity1(:,2);
        velocity(:,3) = velocity(:,3)/z(i,1);
        velocity(:,4) = velocity(:,4)/z(i,1);
        velocity(:,5) = sqrt(velocity(:,3).^2+velocity(:,4).^2);
        vorticity(:,3) = vorticity(:,3)/z(i,1);
        velvort(:,i)=[velocity vorticity(:,3)]; %combines the vorticity
and velocity data
        %%%
    end
end

```

```

    scom=sprintf('h:\\splitter
plates\\5mm\\1000Hz_5mode_3s\\exported_new\\velvort%s.txt',ident);
%determines location to save combined data
    % Creating the 8 line header that is needed for Tecplot to
read the file
    str1=sprintf('TITLE = "velvort%s"',ident);
    str2='VARIABLES = "x, mm"';
    str3=' "y, mm"';
    str4=' "u, m/s"';
    str5=' "v, m/s"';
    str6=' "abs velocity, m/s"';
    str7=' "vorticity, 1/s"';
    str8='ZONE T="ZONE 001"';
    str9='I=128, J=128, F=POINT';
    str_f=strvcat(str1,str2,str3,str4,str5,str6,str7,str8,str9);
    fid=fopen(scom,'wt');
    for m=1:9
        fprintf(fid,'%s',str_f(m,:));fprintf(fid,'\n');
    end
    sz=size(velvort(:, :, i)); %adding the combined data to the
header
    for m=1:sz(1)
        for n=1:6
            fprintf(fid,'%i\t',velvort(m,n,i));
        end
        fprintf(fid,'\n');
    end
    fclose(fid)

end % EOF

```

## AIR CLAMP PROJECT

### **a) Paper shape from high-speed photography**

```

%% paper time-dependent case

%% read a file
n=200;
A=1:1:n;

for m=1:n % till the EOF
    k=A(m);
    clear paper_shape
    if m<=9
        identpaper=sprintf('B0000g',k);
        paper_shape = sprintf('C:\\Documents and Settings\\asv\\My
Documents\\MATLAB\\air_clamp\\paper
shape\\time_dep\\export\\090508_FOV3\\exp2\\%s.dat', identpaper);
        ps=textread(paper_shape, '', 125000, 'headerlines', 3);
        eval(['clear ', identpaper]);
    end
end

```

```

elseif m<=99
    identpaper=sprintf('B000%g',k);
    paper_shape = sprintf('C:\\Documents and Settings\\asv\\My
Documents\\MATLAB\\air_clamp\\paper
shape\\time_dep\\export\\090508_FOV3\\exp2\\%s.dat',identpaper);
    ps=textread(paper_shape, '',125000,'headerlines',3);
    eval(['clear ', identpaper]);

elseif m<=999
    identpaper=sprintf('B00%g',k);
    paper_shape = sprintf('C:\\Documents and Settings\\asv\\My
Documents\\MATLAB\\air_clamp\\paper
shape\\time_dep\\export\\090508_FOV3\\exp2\\%s.dat',identpaper);
    ps=textread(paper_shape, '',125000,'headerlines',3);
    eval(['clear ', identpaper]);

elseif m<=9999
    identpaper=sprintf('B0%g',k);
    paper_shape = sprintf('C:\\Documents and Settings\\alexey\\My
Documents\\MATLAB\\air_clamp\\paper
shape\\time_dep\\export\\030908\\exp2\\%s.dat',identpaper);
    ps=textread(paper_shape, '',125000,'headerlines',3);
    eval(['clear ', identpaper]);
end

%% extracting paper shape

jcount=1250;
icount=100;
k=1;
dm_max=170;
for j=1:jcount
    dmax=1;
    for i=1:icount
        if ps((i-1)*jcount+j,3)>dmax && j<1000
            dmax=ps((i-1)*jcount+j,3);
            k=i;
        else if ps((i-1)*jcount+j,3)>dmax && ps((i-1)*jcount+j,2)>0.1
            dmax=ps((i-1)*jcount+j,3);
            k=i;
        end
    end
end
if dmax>dm_max
    h(j,1)=ps(j,1);
    h(j,2)=ps((k-1)*jcount+j,2);
else
    h(j,1)=ps(j,1);
    h(j,2)=0;
end
end

k=0;
for i=1:jcount
    if isinf(1/h(i,2))==0
        h1=h(i,1);

```

```

        h2=h(i,2);
        k=k+1;
        h_final(k,1)=h1;
        h_final(k,2)=h2;
    end
end

%% smoothing: Savitsky-Golay filter

hs=sgolayfilt(h_final(:,2),3,133);

%% create TD structure

lh=1000;
ps_TD(1, :, m)=h_final(1:lh,1);
ps_TD(2, :, m)=hs(1:lh);

end

```

### **b) FFT function**

```

function [vFrequency, vAmplitude] = fastfft(vData, SampleRate, Plot)

%FASTFFT Create useful data from an FFT operation.
% Usage: [vFrequency, vAmplitude] = fastfft(vData, SampleRate,
[Plot])
%
% (no plot will be shown if the last input == 0 or is not included)
%
% This function inputs 'vData' as a vector (row or column),
% 'SampleRate' as a number (samples/sec), 'Plot' as anything,
% and does the following:
%
% 1: Removes the DC offset of the data
% 2: Puts the data through a hanning window
% 3: Calculates the Fast Fourier Transform (FFT)
% 4: Calculates the amplitude from the FFT
% 5: Calculates the frequency scale
% 6: Optionally creates a Bode plot

%Make vData a row vector
if size(vData,2)==1
    vData = vData';
end

%Calculate number of data points in data
n = length(vData);

%Remove DC Offset
vData = vData - mean(vData);

%Put data through hanning window using hanning subfunction
vData = hanning(vData);

%Calculate FFT

```

```

vData = fft(vData);

%Calculate amplitude from FFT (multiply by sqrt(8/3) because of
effects of hanning window)
vAmplitude = abs(vData)*sqrt(8/3);

%Calculate frequency scale
vFrequency = linspace(0,n-1,n)*(SampleRate/n);

%Limit both output vectors due to Nyquist criterion
DataLimit = ceil(n/2);
vAmplitude = vAmplitude(1:DataLimit);
vFrequency = vFrequency(1:DataLimit);

if exist('Plot', 'var')==1 & Plot~=0
    plot(vFrequency, vAmplitude);
    title('Bode Plot');
    xlabel('Frequency (Hz)');
    ylabel('Amplitude');
end

%-----
%-----
%Hanning Subfunction
function vOutput = hanning(vInput)
% This function takes a vector input and outputs the same vector,
% multiplied by the hanning window function

%Determine the number of input data points
n = length(vInput);

%Initialize the vector
vHanningFunc = linspace(0,n-1,n);

%Calculate the hanning function
vHanningFunc = .5*(1-cos(2*pi*vHanningFunc/(n-1)));

%Output the result
vOutput = vInput.*vHanningFunc;

```

**PERMISSION LETTERS FOR COPYRIGHTED MATERIAL**

Dear Dr. Velikorodny,

I received your request to use some of my jet slot oscillator images in your thesis.

You are authorized to include in your thesis images and material from:

Ziada (2000) Interaction of a jet-slot oscillator with a deep cavity resonator and its control. *Journal of Fluids and Structures* (15): 831-843

I am aware that you are granting an irrevocable, non-exclusive license allowing the National Library of Canada to reproduce, loan, distribute, or sell copies of this thesis by any means and in any form or format to make it available to interested persons.

Congratulations for defending your thesis!

Samir Ziada

Dear Mr. Velikorodny,

You are authorized to include in your thesis images and material from:

P. Oshkai 2002 "FLOW-ACOUSTIC COUPLING IN A CAVITY-PIPELINE SYSTEM" Lehigh University, Bethlehem, PA, USA.

I am aware that you are granting an irrevocable, non-exclusive license allowing the National Library of Canada to reproduce, loan, distribute, or sell copies of this thesis by any means and in any form or format to make it available to interested persons.

Best regards,

Peter Oshkai.

**SPRINGER LICENSE  
TERMS AND CONDITIONS**

Nov 23, 2009

---



---

This is a License Agreement between Alexey S Velikorodny ("You") and Springer ("Springer") provided by Copyright Clearance Center ("CCC"). The license consists of your order details, the terms and conditions provided by Springer, and the payment terms and conditions.

All payments must be made in full to CCC. For payment instructions, please see information listed at the bottom of this form.

License Number	2314920007811
License date	Nov 23, 2009
Licensed content publisher	Springer
Licensed content publication	Experiments in Fluids
Licensed content title	Digital particle image velocimetry
Licensed content author	C. E. Willert
Licensed content date	Jan 1, 1991
Volume number	10
Issue number	4
Type of Use	Thesis/Dissertation
Portion	Figures
Author of this Springer article	No
Order reference number	
Title of your thesis / dissertation	Flow-induced sound and vibration due to the separated shear layer in backward-facing step and cavity configurations
Expected completion date	Nov 2009
Estimated size(pages)	150
Total	0.00 CAD
Terms and Conditions	

### Introduction

The publisher for this copyrighted material is Springer Science + Business Media. By clicking "accept" in connection with completing this licensing transaction, you agree that the following terms and conditions apply to this transaction (along with the Billing and Payment terms and conditions established by Copyright Clearance Center, Inc. ("CCC"), at the time that you opened your Rightslink account and that are available at any time at

<http://myaccount.copyright.com>).

#### Limited License

With reference to your request to reprint in your thesis material on which Springer Science and Business Media control the copyright, permission is granted, free of charge, for the use indicated in your enquiry. Licenses are for one-time use only with a maximum distribution equal to the number that you identified in the licensing process.

This License includes use in an electronic form, provided it is password protected or on the university's intranet, destined to microfilming by UMI and University repository. For any other electronic use, please contact Springer at ([permissions.dordrecht@springer.com](mailto:permissions.dordrecht@springer.com) or [permissions.heidelberg@springer.com](mailto:permissions.heidelberg@springer.com))

The material can only be used for the purpose of defending your thesis, and with a maximum of 100 extra copies in paper.

Although Springer holds copyright to the material and is entitled to negotiate on rights, this license is only valid, provided permission is also obtained from the (co) author (address is given with the article/chapter) and provided it concerns original material which does not carry references to other sources (if material in question appears with credit to another source, authorization from that source is required as well). Permission free of charge on this occasion does not prejudice any rights we might have to charge for reproduction of our copyrighted material in the future.

#### Altering/Modifying Material: Not Permitted

However figures and illustrations may be altered minimally to serve your work. Any other abbreviations, additions, deletions and/or any other alterations shall be made only with prior written authorization of the author(s) and/or Springer Science + Business Media. (Please contact Springer at [permissions.dordrecht@springer.com](mailto:permissions.dordrecht@springer.com) or [permissions.heidelberg@springer.com](mailto:permissions.heidelberg@springer.com))

#### Reservation of Rights

Springer Science + Business Media reserves all rights not specifically granted in the combination of (i) the license details provided by you and accepted in the course of this licensing transaction, (ii) these terms and conditions and (iii) CCC's Billing and Payment terms and conditions.

#### Copyright Notice:

Please include the following copyright citation referencing the publication in which the material was originally published. Where wording is within brackets, please include verbatim.

"With kind permission from Springer Science+Business Media: <book/journal title, chapter/article title, volume, year of publication, page, name(s) of author(s), figure number(s), and any original (first) copyright notice displayed with material>."

Warranties: Springer Science + Business Media makes no representations or warranties

with respect to the licensed material.

#### Indemnity

You hereby indemnify and agree to hold harmless Springer Science + Business Media and CCC, and their respective officers, directors, employees and agents, from and against any and all claims arising out of your use of the licensed material other than as specifically authorized pursuant to this license.

#### No Transfer of License

This license is personal to you and may not be sublicensed, assigned, or transferred by you to any other person without Springer Science + Business Media's written permission.

#### No Amendment Except in Writing

This license may not be amended except in a writing signed by both parties (or, in the case of Springer Science + Business Media, by CCC on Springer Science + Business Media's behalf).

#### Objection to Contrary Terms

Springer Science + Business Media hereby objects to any terms contained in any purchase order, acknowledgment, check endorsement or other writing prepared by you, which terms are inconsistent with these terms and conditions or CCC's Billing and Payment terms and conditions. These terms and conditions, together with CCC's Billing and Payment terms and conditions (which are incorporated herein), comprise the entire agreement between you and Springer Science + Business Media (and CCC) concerning this licensing transaction. In the event of any conflict between your obligations established by these terms and conditions and those established by CCC's Billing and Payment terms and conditions, these terms and conditions shall control.

#### Jurisdiction

All disputes that may arise in connection with this present License, or the breach thereof, shall be settled exclusively by the country's law in which the work was originally published.

#### v1.2

Gratis licenses (referencing \$0 in the Total field) are free. Please retain this printable license for your reference. No payment is required.

If you would like to pay for this license now, please remit this license along with your payment made payable to "COPYRIGHT CLEARANCE CENTER" otherwise you will be invoiced within 30 days of the license date. Payment should be in the form of a check or money order referencing your account number and this license number 2314920007811.

If you would prefer to pay for this license by credit card, please go to <http://www.copyright.com/creditcard> to download our credit card payment authorization form.

Make Payment To:  
Copyright Clearance Center  
Dept 001  
P.O. Box 843006  
Boston, MA 02284-3006

If you find copyrighted material related to this license will not be used and wish to cancel, please contact us referencing this license number 2314920007811 and noting the reason for cancellation.

Questions? [customercare@copyright.com](mailto:customercare@copyright.com) or +1-877-622-5543 (toll free in the US) or +1-978-646-2777.